JAERI -M
83-058

FIRST WALL EROSION DURING A PLASMA DISRUPTION IN TOKAMAK

March 1983

Hiroo NAKAMURA, Toru HIRAOKA,
A. M. HASSANEIN,* G. L. KULCINSKI**
and W. G. WOLFER**

日本原子力研究所
Japan Atomic Energy Research Institute

JAERI-M レポートは，日本原子力研究所が不定期に公刊している研究報告書です。

入手の問合わせは，日本原子力研究所技術情報部情報資料課（〒319—11 茨城県那珂郡東海村）あて，お申しこしください。なお，このほかに財団法人原子力弘済会資料センター（〒319—11 茨城県那珂郡東海村日本原子力研究所内）で複写による実費頒布をおこなっております。

JAERI-M reports are issued irregularly.

Inquiries about availabiljty of the reports should be addressed to Information Section, Division of Technical Information, Japan Atomic Energy Research Institute, Tokai-mura, Naka-gun, Ibaraki-ken 319 -11, Japan.

編集兼発行　日本原子力研究所

印　　刷　㈱原子力資料サービス

JAERI-M 83-058

First Wall Erosion During a Plasma Disruption in Tokamak

Hiroo NAKAMURA, Toru HIRAOKA, A.M. HASSANEIN*
G.L. KULCINSKI** and W.G. WOLFER**

Division of Large Tokamak Development
Tokai Research Establishment, JAERI

(Received March 7, 1983)

This paper presents results for first wall erosion by evaporation and melting during a plasma disruption. As first wall materials, 316SS, Mo, C, SiC, and TiC are considered. The calculational model includes moving boundaries, non-equilibrium evaporation, vapor shielding, and temperature dependent material properties. The results show that the total erosion thickness depends on melt layer stability and vapor shielding. Calculations were carried out for deposition times equal to 0.1, 0.5 and 1.0 msec for a large tokamak, and equal to 5, 10 and 20 msec for INTOR and for energy densities as large as 1300 J/cm^2. For example, in the severe case of vapor shielding and 200 J/cm^2-0.1 msec disruption, total erosion thicknesses of C, SiC, TiC and Mo are 4, 5, 6, 2 μm for the stable melt layer, and 4, 5, 25, 39 μm for the unstable melt layer. In the future, to evaluate the erosion thickness in more detail, further analyses is required for the vapor shielding model including atomic processes, chemical erosion, and the melt layer stability. Also, a better plasma experiment data base concerning energy density, deposition time, and first wall damage will be required.

Keywords: First Wall Erosion, Plasma Disruption, Evaporation, Melting, Staniless-steel, Molybdenum, Carbon, Titanium Carbide, Silicon Carbide, Vapor-shielding, Non-equilibrium Evaporation, Large Tokamak, INTOR

---

* Argonne National Laboratory, Materials Science and Technology Division.
** University of Wisconsin, Madison

JAERI－M 83－058

トカマク型核融合装置におけるプラズマディスラプションによる第一壁損耗量の評価

日本原子力研究所東海研究所大型トカマク開発部
中村　博雄・平岡　　徹・A. M. HASSANEIN*
G. L. KULCINSKI**・W. G. WOLFER**

（1983年3月7日受理）

本論文は，プラズマディスラプション時の蒸発・溶融による第一壁損耗量の評価について述べた。第一壁材は，316SS，Mo，C，SiCおよびTiCについて検討した。計算モデルは，移動境界条件，非定常蒸発，蒸気シールド効果および温度依存物性値を取扱っている。計算は，大型トカマクに対応して0.1，0.5および1.0m sec，INTORトカマクに対応して5，10および20m secのディスラプション時間について行なわれた。蒸気シールド有り，エネルギー密度200 J/cm²，エネルギー時定数0.1m secのプラズマディスラプションの場合，全損耗量は，C，SiC，TiC，Moに対して，それぞれ4，5，6，2 μm（溶融層が安定な場合）および，4，5，25，39μm（溶融層が不安定な場合）である。これらの損耗量は，第一壁の寿命に影響するため，より詳細な損耗量評価を行うためには，原子分子過程を考慮した蒸気シールドモデル，化学反応による損耗，および溶融層の安定性に関して検討が必要である。又．トカマク装置でのディスラプションプラズマと第一壁の相互作用の実験が，今後重要と考えられる。

＊　アルゴンヌ国立研究所材料科学技術部
＊＊　ウィスコンシン大学（米国マジソン州）

CONTENTS

目　　次

1. Introduction

The existence of plasma disruptions in tokamaks has been known ever since that confinement concept was first introduced by Soviet scientists in 1968. During a plasma disruption, it is expected that extremely high heat loads are deposited on limiters and bring about severe melting and vaporization. These damages have already been observed even in ohmically heated tokamaks such as ST, ORMAK, TFR, and JFT-2. With increasing additional heating power, these problems become one of the important issues which limit the lifetime of a first wall. Therefore, intensive studies on disruption theory and experiments are under way to suppress plasma disruptions[1]. Nevertheless, since present plasma discharges can not be freed of disruptions, we must consider them in the design. For this reason, investigations on first wall erosion under high heat load have been performed. Behrisch 2,3 Behrisch[2,3] has treated slow evaporation with the assumption that energy losses due to melting and evaporation are negligible compared to the disruption heat load. On the other hand, L.L. Loebel, et al.[4] have treated intense evaporation with a model that assumes evaporation only when the surface temperature reaches the boiling point. However, it is difficult to define an ambient vapor pressure and have a boiling point clearly. Recently, Hassanein et al.[5,6] have developed an exact model which takes into account the energy loss of the evaporation and melting process, and the kinetics of non-equilibrium evaporation. Another feature of this model is vapor shielding whereby the vapor layer in front of melted surface decreases the disruption heat load significantly.

This paper describes the results of parametric calculations with Hassanein's model for five candidate materials (SS316, Mo, C, SiC, TiC). Details of the model are described in chapter 3. Calculations have been performed with two sets of parameters relevant for large tokamaks (such as TFTR, JET, JT-60 and T-15) and INTOR. Results are shown in chapter 4. To study the influence of the partial vapor shielding and vapor transport on the erosion thickness, various modifications of the vapor shielding model are described in chapter 5.

2. Plasma disruptions

2.1 Disruption parameters

One of the first problems encountered in this area of research is the lack of well documented experimental data about disruptions. The cause of disruptions and methods to prevent their occurrence are relatively unknown at this time, so it is generally felt throughout the field that we will have to design chamber walls and limiters which can take hundreds to thousands of such disruptions over the lifetime of a device. The major areas of uncertainty in this field are;

1. Time of plasma disruption.
2. Partitioning of plasma and magnetic energy into the first wall.
3. Fraction of the disruption energy which appears as X-rays.
4. Location of the place where the disruptions will hit the wall.
5. Area over which the plasma deposits its energy.

A schematic of the factors that contribute to the plasma energy flux and how that is partitioned to the wall is given in Fig.2-1. In this chapter, the five major areas of uncertainty are discussed.

According to current experimental evidence, typical disruption times for energy loss are listed below.

Device	Energy Loss Time
JFT-2	less than 625 μsec [7]
Alcator	0.1 msec
PLT	0.2 msec
Doublet-III	less than 125 μsec [10]

One way of estimating the disruption time is to assume it scales as $T_e^2 a$ or $T_e^3 a^2$ where T_e is the electron temperature and a is the minor radius of the torus[8]. For example, using values for PLT as a reference, we predict disruption times of 4 ms to 26 ms in INTOR. The IAEA workshop in Vienna assumed 20 ms for a reference value and 5 ms for a alternative one as the disruption time. Also, the range of the disruption time for the large tokamaks is assumed to be 0.1 ~ 1 msec.

The number of disruptions is also subject to a great deal of uncertainty. Currently disruption frequencies of 1 in a 100 are typical.

Presumably, we will do better once the machine is running, and the INTOR workshop assumed a frequency of 5×10^{-3} in stage I and a frequency of 0.001 in Stage II and III. The number of disruptions during each Stage is about 500. Characteristics time scale and frequency are shown in Table 2-1[9].

The total energy content of the plasma is the sum of the thermal energy of the ions and electrons plus the stored magnetic energy. The value of the plasma thermal energy is;

$$\frac{3}{2} \times (\text{average beta}) \times \frac{B^2}{2\mu} \times (\text{plasma volume}) \qquad (2\text{-}1)$$

The stored energy in poloidal magnetic field is obtained from

$$\beta_p = \frac{\int dV \, \frac{3}{2} nKT}{\int dV \, B_p{}^2 / 2\mu_0} \qquad (2\text{-}2)$$

The mechanism by which the magnetic energy is converted to thermal energy is by frictional losses as the flux lines move through the plasma. The amount of stored magnetic energy that appears as heat in the first wall is also unknown. In this study, this value was assumed to be zero.

The plasma energies are estimated to be about 20 MJ for large tokamaks and about 220 MJ for INTOR.

The next step to calculating the first wall energy flux is the determine how much of the plasma energy goes to the wall as X-rays and how much is transported by ions. When the plasma contains a large amount of impurities, essentially all of the plasma energy could be radiated uniformly to the wall as X-ray. If the plasma is relatively "clean", essentially all of the energy will be transferred to the walls in the form of kinetic energy of the plasma particles. During disruptions in present machines, it is commonly observed that the radiation load increases by factor of 5 to 10 over the steady-state values.

In the case of present tokamaks, 50 ~ 70% of the plasma thermal energy goes to the wall during a major disruption[9]. The value of X-rays fraction assumed are 50% for large tokamaks and 30% for the INTOR reference case. Since this energy is uniformly deposited around the chamber, the energy flux is less than a few tens J/cm^2.

Another item for calculating the energy density on the first wall is the area of plasma deposition. Currently, 90% of the disruptions in Alcator A and Alcator C occur on the inboard side. However, the present result of the disruption experiment in D-III[10] shows that the disruption energy is deposited on the outboard side limiter if the plasma contacts the limiter just before the disruption. On the other hand, it is expected that the deposition area is located on the inboard side if the plasma contacts on the inboard side limiter before the disruption. From these results, it is considered that the area of plasma deposition depends on the limiter position and the impurity control methods (material limiter, pumped limiter and divertor). For example, there are toroidal fixed limiters in JT-60, toroidal bumper limiters in TFTR, and poloidal limiters in JET. In recent INTOR design (1982), there is a single-null poloidal divertor as shown in Fig.2-2.

In the large tokamaks, if we assume disruption parameters such that thermal energy to the limiter is 10 MJ, the deposition area is 10 m^2, and peaking factor is 2, the energy density is determined to be about 200 J/cm^2.

In the INTOR deisgn (1982), the energy densities are determined for pumped limiter operation and one divertor. The reference values are 175 J/cm^2 on the first wall and 230 J/cm^2 on the divertor plate for the divertor operation, and 175 J/cm^2 on first wall and 270 J/cm^2 on the limiter for the pumped limiter operation, respectively.

2.2 Description of disruption sequence

The disruption/vaporization process will be broken up into 8 distinct time periods in order to facilitate the examination of disruption models. Once this scenario has been established we will examine (in the next chapter) how previous models have addressed some of these time periods. Before starting, a few terms need to be defined.

t = time from the start of the disruption,

t_m = time required to raise the temperature of the first wall to its melting point,

t_v = time at which significant vaporization begins,

t_{Ed} = time duration of plasma energy loss,

t_{cd} = time duration of current decay, usually $t_{cd} > t_{Ed}$.

Obviously if $t_{Ed} < t_v$, then we only need to worry about the melt layer and no material will be lost from the front surface.

There are three distances that we need to define.

ΔX_m is the thickness of the melt layer on the front surface,

ΔX_v is the thickness of the first wall vaporized,

X_v is the maximum distance that the vaporized atoms have traveled into the plasma chamber.

Finally, there is the energy flux to the first wall surface, F_0. This flux is composed of X-rays, F_x, and the energy flux from the plasma ions, F_i. The value of F_i depends on the interaction of the "incoming" plasma and the "outgoing" vaporized atoms. Fig.2-3 summarizes the disruption/vaporization process considered here.

Step 1

The initial conditions of the problem are that the first wall is completely solid at a temperature T_{ss} (modifications for a liquid first wall can easily be made) and the energy content of the plasma is E megajoules. The temperature of the wall just before the disruption is determined by the steady state surface heat flux, F_{ss}, the neutron heating, and the method of cooling the first wall. For example, these factors cause the first wall of the INTOR reactor to be at 300°C before the disruption.

Step 2

At time $t = 0$, it is assumed that the plasma disruption occurs and the plasma is contacting the first wall. In reality, there will be a short time from the time that the instability starts, X-rays are emitted, and the plasma contacts the wall. However, in this scheme we will assume that this time is short (< 1 microsecond) and that the X-rays and ions strike the first wall with appropriate energy densities (F_x and F_i, respectively) evenly spread over the disruption time, t_{Ed}. The total energy flux is then $F = F_i + F_x$.

Step 3

The continual bombardment of the first wall with the energetic ions and X-rays from the plasma will cause the surface of the first wall to increase in temperature. Some of this energy will be reradiated from the front surface (less than a few percent during the disruption)

and some of this heat will also be conducted into the solid material heating up the first wall over a much larger region than the initial ion or X-ray energy deposition zone. This heating will continue until we reach the next step, i.e. melting at time t_m.

Step 4

As the temperature of the first wall exceeds the melting point, a liquid layer of thickness $\Delta X_m(t)$ will develop. The heat flux to the solid part the first wall (behind the melt region) will include the "loss" of the heat of fusion. The boundary between the melted layer and the solid first wall will move into the solid and we are faced with a so-called "moving boundary" problem. The temperature of the melted layer at the front surface continues to rise as the heat flux, F_0, continues.

Step 5

After part of the first wall has melted, the liquid will be heated until its vapor pressure is sufficient to cause significant vaporization of the first wall. At that point metallic atoms will absorb the heat of vaporization and be released from the melted layer into the plasma chamber. The velocity of these atoms will depend on the vaporization temperature and the angle at which they are emitted into the chamber will be nearby isotropic (2π steradians). At first the metallic atoms will stream into the vacuum with a large mean free path between collisions. Eventually, the density of evaporated atoms will build up to the point that the mean free path between collisions is so short that the velocity distribution becomes fully isotropic. At this point some of the vaporized atoms will be redeposited on the original surface.

The atoms leaving the surface will be moving against the flux of plasma particles from the disruption and will also gain energy by electronic and nuclear collisions. The actual energy flux that reaches the first wall will then be less than F_0 because plasma ion energy which is deposited in the metal vapor. Therefore, the energy flux that actually reaches the front surface of the liquid will be represented as $F_0 - F_d(t)$ where $F_d(t)$ is the average loss of plasma ion energy in the expanding vapor.

Finally, the actual amount of material removed from the melt layer will be the net sum of the evaporation and condensation. We will assume

that the recondensing atoms land on the same area from which they left neglecting large lateral transport in the magnetic field or irregularities in the wall design.

Step 6

At the end of the plasma disruption, that is, when the last plasma ions have hit the first wall, the metallic ions will continue to evaporate until the vapor pressure of the melt layer is less than that in the chamber. When this happens, a maximum amount of first wall will have been evaporated (ΔX_v^{max}), and the final erosion will depend on how much of the evaporated atoms are recondensed on the original surface.

Step 7

The liquid layer now cools off by conducting the deposited heat into the solid or reradiating the energy to surrounding colder surfaces. During this time period the latent heat of fusion is recovered and the melted zone shrinks. Also during this time period, I^2R heating from the decaying current will be encountered, but in the present problem we will assume this to be small and spread out over a much longer time than the plasma disruption, i.e., $t_{cd} \gg t_{Ed}$.

Step 8

Once the melted layer has disappeared, the temperature in the solid first wall will continue to fall as the heat is conducted and radiated away. Eventually the temperature falls to a level determined by the input of decay and I^2R heating, and by heat removed by the coolant.

Table 2-1 Characteristic time scales for disruption [9].

Parameters	Present tokamaks	INTOR
Time scales (ms)		
Thermal (τ_{th})	0.1–1	≈ 20
Voltage spike (τ_V)	0.1–0.3	≈ 20
Current decay (τ_I)	1–20	$\gtrsim 20$
Frequency	$\lesssim 10^{-2}$	5×10^{-3} in Stage I 10^{-3} in Stages II and III

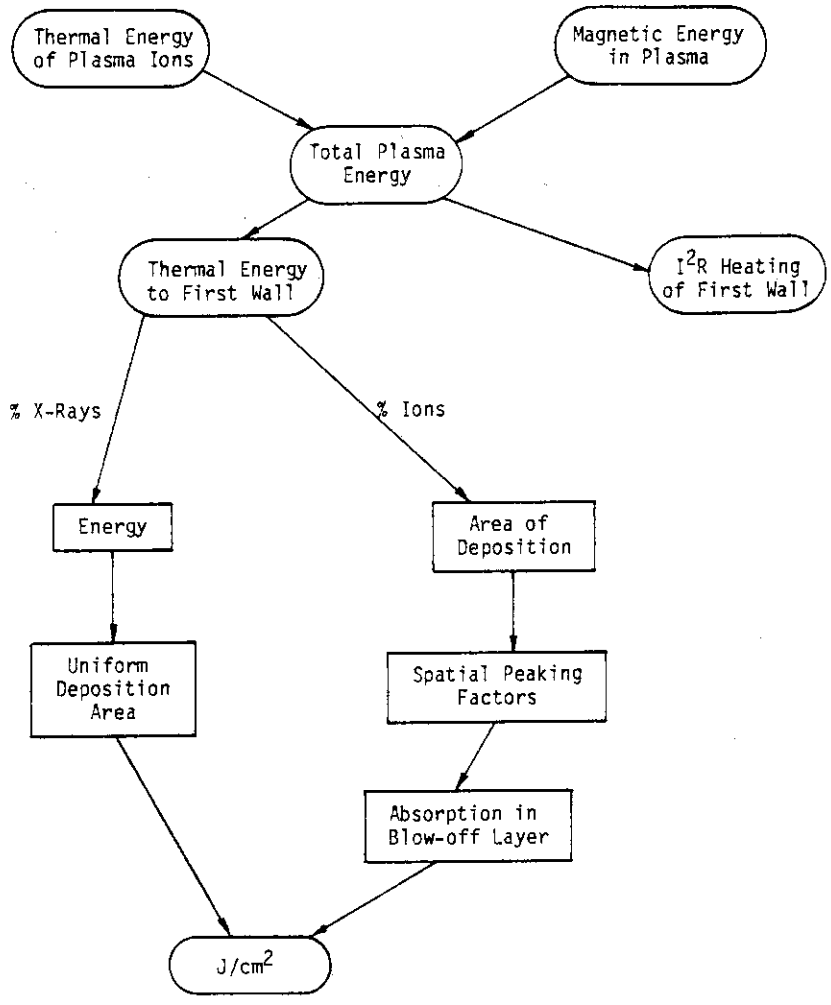

Fig. 2-1 Schematic of factors to be considered for calculating energy deposition densities from plasma disruptions.

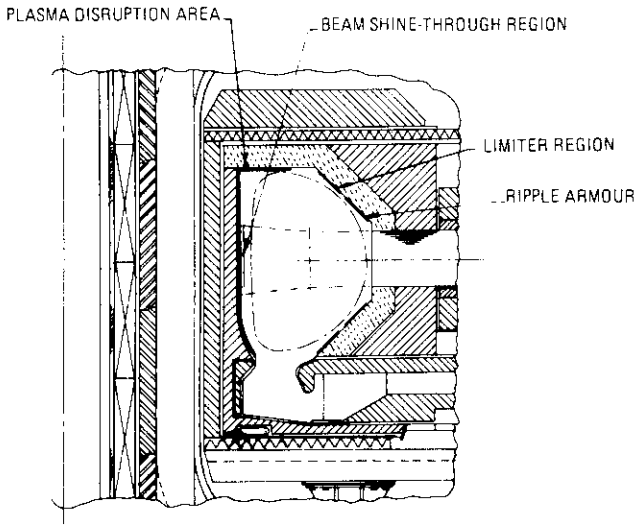

Fig. 2-2 INTOR first wall configuration [9].

SCHEMATIC OF DISRUPTION / VAPORIZATION PROCESS

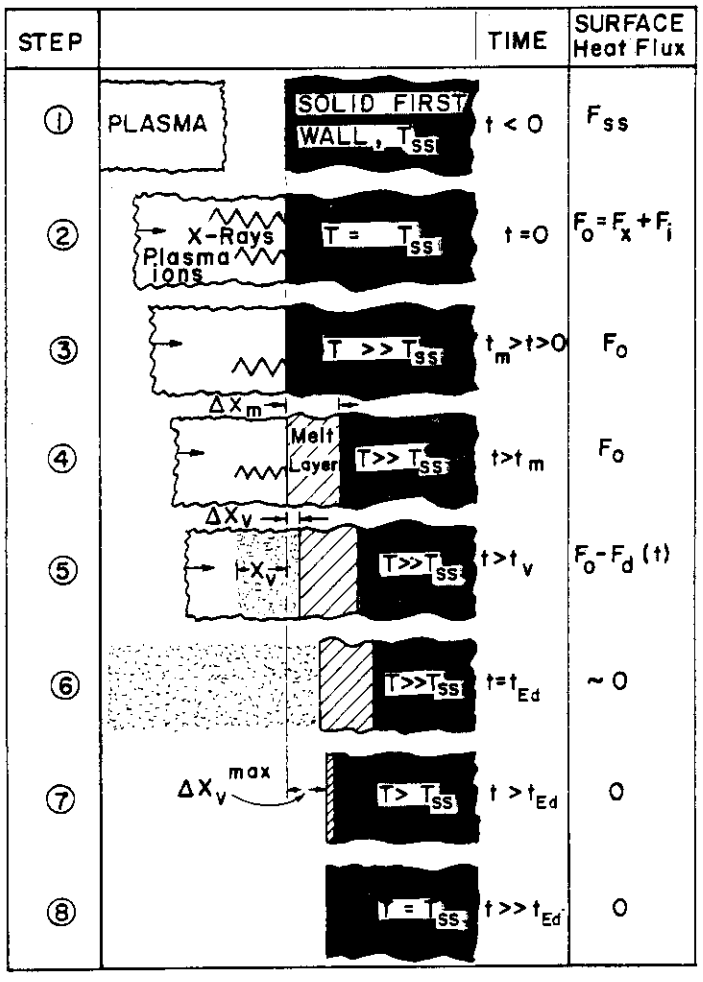

Fig. 2-3 Schematic representation of disruption-vaporization process.

3. Calculational models

The general description of this problem can be conveniently broken up into 4 parts as illustrated in Fig.3-1. A brief discussion of each step is given below.

1) The temporal, volumetric and surface heat flux to the first wall including X-rays and ions must be given. This heat flux should be appropriately corrected for radiation losses from the front surface and loss of energy by the plasma ions in the blow-off vapor from the first wall, although the former is usually negligible for steel.
2) The temperature distribution that exists in the solid and liquid layer (should any develop) must be calculated. This calculation should include the thermal variation of materials properties and the heat of fusion and vaporization. The temperature profile should be appropriately adjusted for two moving boundaries; that between the vapor and the metal layer as well as that between the melt layer and the solid.
3) The rate at which metallic first wall atoms leave the surface of the melt zone and stream into the vacuum chamber must be determined. This requires a knowledge of the vapor pressure as a function of temperature and the results of such a calculation will reveal the spatial distribution of the evaporated atoms in the chamber.
4) The rate at which metallic atoms are redeposited on the original surface needs to be determined. This is a very difficult calculation because it requires a knowledge of the mean free path for collisions between the evaporated atoms, and any transport processes going on while the atoms is in the chamber.

Once all four steps have been integrated together we can get an accurate picture of the net erosion produced by the intense heat pulse. We have already discussed the first step in Chapter 2 so in this chapter will examine steps 2, 3, and 4.

3.1 Temperature calculation with moving phase boundaries

The rapid heating of the first wall during a plasma disruption may lead to melting and to subsequent evaporation of the first wall material. Assuming that the melt layer is not removed, the temperature distribution

through the first wall must be computed according to the following steps.

For time periods less than t_m, the time to reach the melting point on the surface, the heat conduction equation

$$\rho_s C_s \frac{\partial T_s}{\partial t} - \nabla \cdot K_s \nabla T_s = \dot{q}(x,t) \qquad (3\text{-}1)$$

must be solved subject to the boundary conditions that, $T = T_0 = \text{constant}$, on the coolant side and,

$$F(t) = - K_s \frac{\partial T_s}{\partial x} + \rho_s(T_v)\, L_v v(t) + \sigma(T_v^4 - T_0^4) \qquad (3\text{-}2)$$

on the surface facing the plasma. Here $F(t)$ is the heat flux, $\dot{q}(x,t)$ is the volumetric energy deposition rate, $\rho_s(T)$ is the density, $C_s(T)$ the specific heat, and $K_s(T)$ the thermal conductivity of the solid material. The heat of vaporization is L_v, T_s is the temperature in the solid, T_v the surface temperature, and $v(T_v(t))$ is the velocity of the receding surface. Furthermore, the radiative heat transfer term contains the Stefan-Boltzmann constant σ and the surface temperature T_0 of the cold portion of the first wall. The velocity v is a function of the instantaneous surface temperature and other materials parameters. The second term in equation (3-2), which will be discussed shortly in connection with the evaporation energy loss rate, is negligible for temperatures below the melting point.

Once melting occurs, the condensed phase consists of two regions:

a) $s(t) \leqslant x \leqslant m(t)$ for the melt layer

b) $m(t) \leqslant x$ for the solid phase.

where: $s(t)$ is the distance of the melted surface from the original solid surface;

$m(t)$ is the distance of the melted layer from the original surface.

Equation (3-1) applies again to the solid phase, but the boundary conditions are now that at $x = m(t)$

$$T_s(m(t),t) = T_\ell(m(t),t) = T_m \qquad (3\text{-}3a)$$

and

$$- K_\ell \left.\frac{\partial T_\ell}{\partial x}\right|_{m(t)} = - K_s \left.\frac{\partial T_s}{\partial x}\right|_{m(t)} + \rho_s L_f w(t) \qquad (3\text{-}3b)$$

where T_m is the melting temperature, T_ℓ is the temperature in the melt layer, L_f the latent heat of fusion, and

$$w(t) = \frac{dm}{dt} \qquad (3\text{-}4)$$

is the velocity of the melt-solid interface. In the melt layer, the heat conduction equation is

$$\rho_\ell C_\ell \frac{\partial T_\ell}{\partial t} - \nabla \cdot K_\ell \nabla T_\ell = \dot{q}(x,t) \quad . \qquad (3\text{-}5)$$

The solution in the melt layer must satisfy the boundary conditions (3-3) and (3-4) on $x = m(t)$ and the condition

$$F(t) = - K_\ell \left.\frac{\partial T_\ell}{\partial x}\right|_{s(t)} + \rho_\ell(T_v)\, L_v\, v(t) + \sigma(T_v^4 - T_0^4) \qquad (3\text{-}6)$$

on the surface $x = s(t)$.

Finally, we can introduce a moving coordinate system

$$z(t) = x - s(t) \qquad (3\text{-}7)$$

for which the surface remains always at $z = 0$. However, the heat conduction equations (3-1) and (3-5) are now changed to

$$\rho C \frac{\partial T}{\partial t} - \rho C\, v(t) \frac{\partial T}{\partial z} - K \frac{\partial^2 T}{\partial z^2} = \dot{q}(z,t) \quad . \qquad (3\text{-}8)$$

The main difference in this equation is that it includes the convective term $v(\partial T/\partial z)$.

The most general approach to solve the equations (3-1) through (3-7), without any restrictions, is by the finite difference method. A computer program based on this method has been developed using the Crank-Nicholson implicit method for solving the time-dependent heat conduction equation in the moving frame defined by equation (3-7). All thermal materials properties for both the solid and liquid phase may be polynomial functions of the temperature.

Melting, evaporation, as well as radiative heat transfer are

included in the computation, and the energy deposition may be an arbitrary function of time or other time-dependent variables. Furthermore, the energy deposition can be partitioned into surface a heat flux and a volumetric heat production rate. The latter may be a function of depth. The results of the present calculations were, however, obtained by assuming that the entire energy deposition can be adequately modeled as a surface heat flux.

In order to achieve high accuracy for the surface temperature and for the advance of the melt-solid interface, variable thickness zones are used. The spacing of the grid points is chosen to be small near the surface, and increases with increasing depth into the material.

A input manual of the computer program based on the finite difference method is given in Appendix A.

3.2 Evaporation models

According to the Hertz-Knudsen-Langmuir theory of evaporation and condensation, the net flux of atoms leaving the surface of the condensed phase is given by

$$J = (2\pi mkT)^{-1/2} (\sigma_e P_s - \sigma_c P_c) \tag{3-9}$$

Here, m is the mass per atom, k the Boltzmann constant, σ_e and σ_c are coefficients, P_c is the ambient partial pressure in the chamber, and

$$P_s = P_0 \exp(-\Delta H/RT) \tag{3-10}$$

is the saturation vapor pressure. Equation (3-9) consist of two opposite fluxes, $J = J_e - J_c$, an evaporation and a condensation flux.

Although Eq.(3-9) is valid only for thermal equilibrium, it can be modified for non-equilibrium evaporation or condensation. If the surface temperature T_v of the condensed phase is different from the temperature T_c of the ambient vapor, the evaporation and condensation flux may be written as

$$J_e^{eq} = (2\pi mkT_v)^{-1/2} \sigma_e P_s(T_v) \tag{3-11}$$

and

$$J_c = (2\pi mkT_c)^{-1/2} \sigma_c P_c \tag{3-12}$$

The evaporation flux J_e^{eq} represents a maximum for evaporation into a vacuum provided the vapor expands at a sufficient rate so the vapor density in front of the surface always remains low.

The net evaporation flux may be computed according to

$$J = J_e^{eq}(T_v) - J_c(T_c) \tag{3-13}$$

if the two fluxes do not interact. This will only be the case for slow evaporation, i.e., when both J_e^{eq} and J_c are small or when they are almost of equal magnitude.

Unfortunately, for conditions encountered in a plasma disruption, Eq.(3-13) cannot be considered valid. Since the evaporation flux is expected to be high, the vapor density in front of the surface is finite even if the vapor gas expands into a vacuum. As a result, J_v^{eq} is not the maximum evaporation flux into a vacuum for intense evaporation.

One may be tempted to assume that the maximum evaporation flux is determined by the velocity of an adiabatically expanding gas. Therefore, we consider for the moment a gas of initial density n and initial temperature T_v. It expands into one direction with a maximum velocity of[11]

$$U_{max} = 4\ c_o$$

where

$$c_o = \sqrt{\gamma k T_v / m}$$

is the speed of sound in a gas of temperature T_v and density n, and γ is the ratio of the specific heats for constant pressure and constant volume. For a monoatomic gas, $\gamma = 5/3$.

The maximum flux of evaporation according to this model would be given by

$$J_e^{max} = 4\ c_o n_s = 4\ \left(\frac{3kT_v}{2m}\right)^{1/2} \frac{p_s}{kT_v}$$

$$= 4\sqrt{3\pi}\ J_e^{eq} \tag{3-14}$$

Since this is larger than J_e^{eq}, we conclude that hydrodynamic

considerations alone cannot be invoked to limit the rate for intense evaporation below the maximum equilibrium rate.

It is therefore necessary to derive the rate of recondensation of the expanding vapor from gas-kinetic considerations. In an early analysis by Schrage[12], the vapor is treated as a gas with a Maxwellian velocity distribution superimposed on an average velocity $\bar{u}$. This average velocity must be equal to the average forward velocity of a stationary Maxwellian gas. Hence

$$\bar{u} = (kT_v/2\pi m)^{1/2} \quad . \tag{3-15}$$

The fraction of recondensing atoms is now given by

$$\Gamma = \exp(-a^2) - a\sqrt{\pi}\ \mathrm{erfc}(a) \tag{3-16}$$

where

$$a = \bar{u}/v_0$$

and

$$v_0 = \sqrt{2kT_v/m}$$

is the most probably velocity of the Maxwellian gas.

The net evaporation flux is then equal to

$$J = J_e^{eq}\left(1 - \frac{\sigma_c}{\sigma_e}\Gamma\right) \quad . \tag{3-17}$$

Assuming that $\sigma_c = \sigma_e = 1$, one obtains for $a = 0.282$ a maximum net evaporation flux of

$$J = 0.422\ J_e^{eq} \quad . \tag{3-18}$$

More accurate transport calculations for intense evaporation have been performed more recently by Anisimov and Rakhmatulina[13]. In their work the following problem was considered: The surface of a material which occupies the half-space is suddenly raised and held at a constant surface temperature T_v for times $t \geq 0$. The material begins to vaporize and the vapor expands freely into the vacuum. Initially, the evaporation flux leaving the surface is equal to J_e^{eq}, but it decreases thereafter due to recondensation. This process of recondensation arises from two facts. First, the density of vapor expanding into a vacuum

retains a finite value for $t > 0$ in front of the surface. Second, atoms evaporated subsequently from the surface may collide with the already present vapor phase and be backscattered towards the surface where they may be reabsorped. The fraction of recondensing atoms will increase as the vapor density and the spatial extension of the vapor phase increases with time. However, an asymptotic value of 0.2 is reached for this fraction after about 20 collision times. The collision time τ_c for the vapor atoms is given by

$$\frac{1}{\tau_c} = 16\sqrt{\pi}\, na^2\, (kT_v/m)^{1/2} . \tag{3-19}$$

where πa^2 is the elastic scattering cross section for the vapor atoms and n the vapor density in front of the surface. The latter can be related to the maximum vacuum evaporation rate according to

$$J_e^{eq} = \frac{1}{4}\,\bar{v}n = n(kT_v/2\pi m)^{1/2} \tag{3-20}$$

where we used the relation

$$\bar{v} = (8kT_v/\pi m)^{1/2}$$

for the average velocity of the vapor atoms.

For the elastic scattering cross-section we may use the approximation that

$$\frac{4\pi}{3}\, a^3 = \Omega$$

where Ω is the atomic volume. Then, the collision time τ_c is given by

$$\frac{1}{\tau_c} = 16\sqrt{2}\, \pi^{1/3}\, (\frac{3}{4}\,\Omega)^{2/3}\, J_e^{eq} \quad . \tag{3-21}$$

The numerical results of Anisimov and Rakhmatulina for the time-dependent net evaporation rate may be approximated by

$$J(t) = J_e^{eq}\, [0.8 + 0.2\, \exp(-t/\tau_R)] \quad . \tag{3-22}$$

The relaxation time τ_R to reach, say 98% of the full amount of recondensation after 20 collision times τ_c, is then given by

$$\tau_R = 20\tau_c \,/\, \ell n 10 \cong 10\tau_c$$

or

$$\frac{1}{\tau_R} = 1.6\sqrt{2}\ \pi^{1/3}\ (\frac{3}{4}\ \Omega)^{2/3}\ J_e^{eq} \quad . \tag{3-23}$$

In the above equations, $J_e^{eq}(T_v)$ is a constant for $t \geqslant 0$, since it was assumed that T_v remains constant.

For our present application, however, the surface temperature $T_v(t)$ varies with time. Nevertheless, as the numerical results in the following section show, the surface temperature rapidly approaches a saturation value once intense evaporation begins. Accordingly, the time variable in equation (3-22) should be replaced by $(t-t_v)$ where the preheat time t_v may be estimated as follows.

In order for recondensation to become significant, the thickness of the vapor zone in front of the surface should be of the order of the mean free collision path

$$\ell = [\sqrt{2}\ n\pi a^2]^{-1} \quad .$$

The thickness Δx of material evaporated to produce a vapor zone of thickness ℓ is then

$$\Delta x(t_v)/\Omega = n\ell$$

or

$$\Delta x(t_v) = \frac{1}{\sqrt{2}\pi}\ (\frac{4}{3})^{2/3}\ (\frac{\Omega}{\pi})^{1/3} = 0.585\ \Omega^{1/3} \quad . \tag{3-24}$$

This corresponds roughly to half of a monolayer of atoms evaporated from the surface. The relationship (3-24) determines the preheat time t_v.

The evaporation flux of atoms is then equal to J_e^{eq}, for $t \leqslant t_v$ and

$$J(t) = J_e^{eq}(T_v(t))[0.8 + 0.2\ \exp(-(t-t_v)/10\tau_c)] \tag{3-25}$$

for $t \geqslant t_v$. It should be noted, that the collision time τ_c is a very strong function of the surface temperature through its dependence on J_e^{eq}. Therefore, if we consider τ_c as a function of time, it will be a very large number before intense evaporation commences, i.e., for $t < t_v$. As a result, the second term in equation (3-22) will then be equal to 0.2, so that automatically $J(t) \cong J_e^{eq}$, for $t < t_v$. Therefore, by

considering the collision time τ_c as a continuous function the changing surface temperature $T_v(t)$, the equations (3-22) and (3-25) are practically identical. In other words, it is not necessary to compute the preheat time t_v in order to obtain the time-dependent evaporation flux J(t) correctly according to equation (3-22).

Finally, we note that the velocity of the receding surface is given by

$$v(t) = \Omega J(t) \quad . \tag{3-26}$$

3.3 Vapor shielding

The heat flux F(t) on the first wall during a disruption consists to a large part of the plasma ions. It is generally believed that a sheath potential of the order of 10 kV exists at the onset of the plasma disruption. The plasma ions will therefore strike the first wall with a kinetic energy of about 10 keV. The average range of the plasma ions in a stainless steel wall is about 7.5×10^{-8} m. Because of this short range, it is indeed appropriate to treat the energy deposition as a surface heat flux rather than a volumetric heat deposition.

On the other hand, if a vapor layer of sufficient thickness has been produced, the plasma ions will be stopped in this vapor layer rather than in the condensed material of the first wall. The vapor layer, in the process of stopping the plasma ions, will be partially ionized, excited, and heated. Subsequently, the energy stored in this vapor layer will be emitted in the form of X-rays, optical radiation, and thermal diffusion of the hot vapor atoms. As a result, the energy flux of the plasma particles is converted from a unidirectional one into a more isotropic one. If we assume in fact that the converted energy flux has become isotropic, only one half of the original, unidirectional energy flux will now strike the part of the first wall exposed to the plasma disruption.

Accordingly, we have modeled the efffct of vapor shielding in the following manner. If F_0 is the magnitude of the initial energy flux, and R the range of plasma ions in the condensed phase of the first wall, a vapor layer produced by the evaporation of a thickness $\Delta x(t) \leqslant R$ will reduce the surface heat flux to the first wall to the value of

$$F(t) = F_0[1 - \Delta x(t)/R] + \frac{1}{2} F_0 \Delta x(t)/R$$
$$= F_0[1 - \Delta x(t)/2R] \quad . \tag{3-27}$$

When the evaporation thickness $\Delta x(t) \geqslant R$, then

$$F(t) = \frac{1}{2} F_0 \quad . \tag{3-28}$$

Fig.3-2 shows schematically the effect of vapor shielding on the surface heat flux according to the present model and for a constant plasma particle flux during the disruption time.

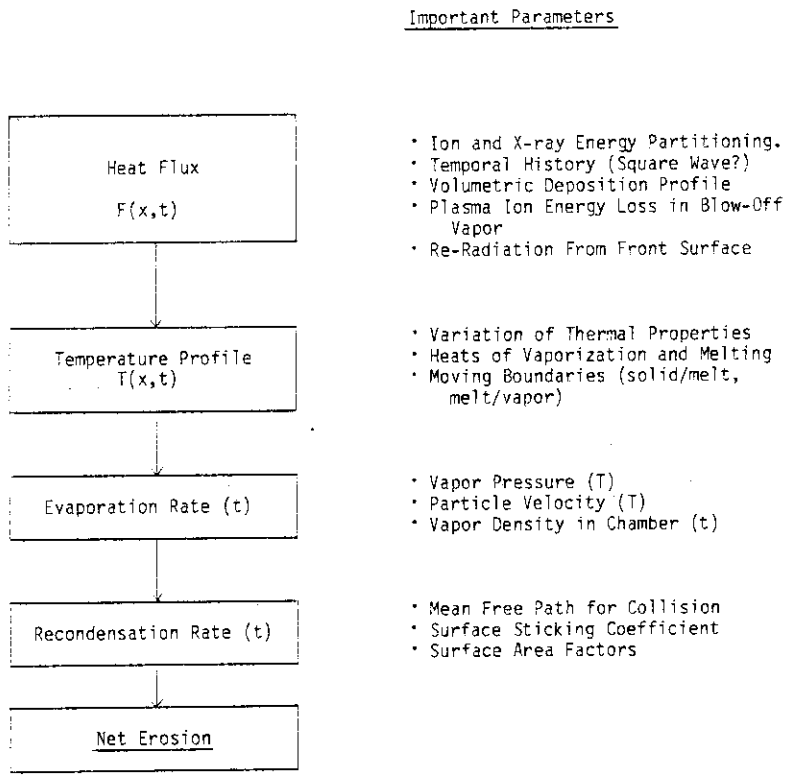

Fig. 3-1 Procedure for calculating the erosion resulting from a plasma disruption.

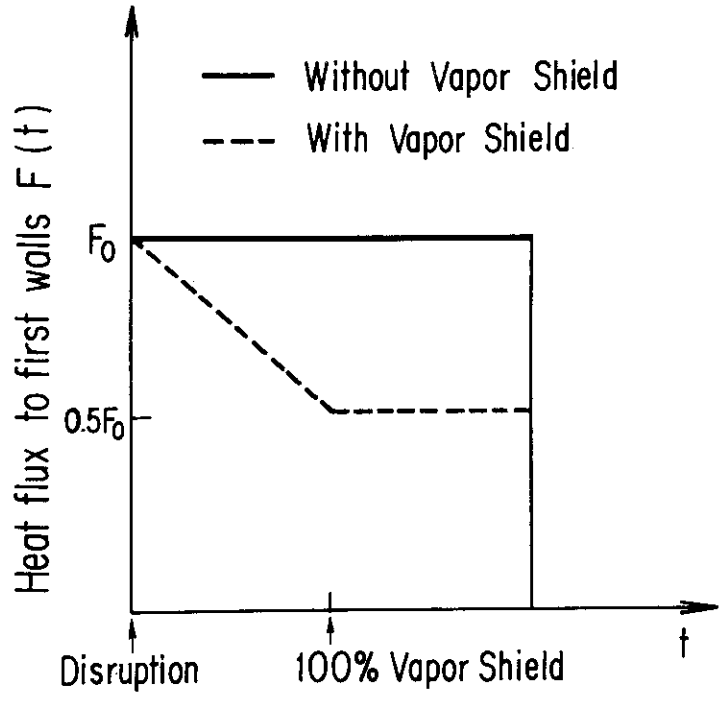

Fig. 3-2 Schematic of heat fluxes to first walls during plasma disruptions.

4. Results of parametric analysis

Present calculations were carried out for deposition times equal to 0.1, 0.5 and 1.0 msec for a large tokamak, and equal to 5, 10, and 20 msec for INTOR and for energy densities as large as 1300 J/cm^2. Furthermore, it was assumed that the energy deposition was constant during a disruption.

Materials considered in this calculation are stainless steel, molybdenum, carbon, silicon carbide, and titanium carbide. Stainless steel is the main candidate material for structural component in fusion reactors. Molybdenum and carbon are the substrate materials in large tokamaks. Titanium carbide is the main candidate material for surface coating in large tokamaks.

Moreover, molybdenum, carbon, silicon carbide are the candidate materials for surface protection in fusion reactors. In this study, calculations were carried out for deposition times appropriate for large tokamaks and for titanium carbide, whereas INTOR parameters were used in the case of stainless steel. Both parameters ranges were investigated for molybdenum, graphite, and silicon carbide. Because, the calculations for large tokamak parameters are urgently needed in a first wall design, calculations in the case of molybdenum, graphite and titanium carbide were carried out in great detail.

4.1 Stainless steel

The thermal properties for 316 stainless steel are as follows:

Heat capacity

$$C_s = 0.1097 + 3.174 \times 10^{-5}\ T \quad (cal/g/K)$$

$$C_\ell = 0.1840 \quad (cal/g/K)$$

Density

$$\rho_s = 8.0842 - 4.2086 \times 10^{-4}\ T - 3.8942 \times 10^{-8}\ T^2 \quad (g/cm^3)$$

$$\rho_\ell = 7.4327 + 2.9338 \times 10^{-5}\ T - 1.8007 \times 10^{-7}\ T^2 \quad (g/cm^3)$$

Thermal conductivity

$$K_s = 9.248 \times 10^{-2} + 1.571 \times 10^{-4}\ T \quad (w/cm/K)$$

$$K_\ell = 1.241 \times 10^{-1} + 3.279 \times 10^{-5}\ T \quad (w/cm/K)$$

Thermal diffusivity

$$\alpha_s = 2.578 \times 10^{-2} + 3.265 \times 10^{-5}\ T - 3.138 \times 10^{-9}\ T^2\ (cm^2/sec)$$

$$\alpha_\ell = 2.686 \times 10^{-3} - 4.812 \times 10^{-7}\ T + 2.58 \times 10^{-9}\ T^2\ (cm^2/sec)$$

Heat of fusion

$$L_f = 64.46\ (cal/gm)$$

Heat of vaporization

$$L_v = 1780.7\ (cal/gm)$$

Vapor pressure

$$\log P_s(atm) = 6.1127 - 18868 / T$$

Figures 4-1 and 4-2 show, using the Pessimistic-Maximum Evaporation Model (no vapor shield), the cumulative amount of material evaporated as a function of time for a 20 ms disruption and energy fluxes from 289 J/cm^2 to 500 J/cm^2. The same information for 800 and 1300 J/cm^2 is given in Fig.4-3. In all the cases, there is an incubation period required to heat up the solid, melt it, and heat the melt layer to a point where significant evaporation can occur. This evaporation threshold varies as follows:

Energy Flux	Incubation time, ms
289	15
350	11
500	6
800	3
1300	2

The cumulative amount of material evaporated is given in Fig.4-4 for 5, 10, and 20 msec disruptions times. As would be expected, the total amount evaporated increases as the disruption time gets shorter.

It is worth noting that for base case INTOR conditions (20 msec - 289 J/cm^2) relatively little erosion is obtained; only if the disruption times are 5 or 10 msec will there be a problem. However, since these parameters are closed to the threshold for evaporation, a reduction of the energy flux to 200 J/cm^2 will avoid any problem even for short disruption times.

Also shown in Fig.4-4 are the results when reradiation, vapor shielding and variable evaporation models are included. The dramatic reduction in erosion is due to the reduction in the heat flux after an amount of steel equivalent to the range of the plasma ions is removed. Since this is only 0.075 micron, the heat flux is quickly dropped to 1/2 of its initial value which greatly reduces the material evaporated at initial heat fluxes of 300 - 500 J/cm^2.

The effect of including reradiation in the net heat flux to the front surface was investigated. It was found, as previously indicated, that it is negligible compared to other effects for steel.
Identical vapor shielded calculations were performed with and without thermal radiation included. The difference is only a few percent, and it is clear that such an effect could be neglected for steel and other low melting point materials. However, because the radiation loss goes as T^4, this effect could be important for refractory metals and for graphite.

Melting zone thickness for different disruption times (5, 20 msec) is shown in Fig.4-5. The threshold energy density and maximum melting zone thickness are 70 J/cm^2 and 120 μm for 5 msec deposition, and 160 J/cm^2 and 260 μm for 20 msec deposition, respectively. With vapor shielding, the energy density at maximum melting increase by 300 J/cm^2 for both depositions. But, the maximum melting zone thicknesses are the same as in the case no vapor shielding.

4.2 Molybdenum

The specific thermal and physical properties of Mo were taken as follows.

Heat capacity

$$C_{ps} = 0.0991 - 4 \times 10^{-5}\ T + 1.77 \times 10^{-8}\ T^2\ \frac{cal}{gm°K}$$

$$C_{p\ell} = 0.101\ \frac{cal}{gm°K}$$

Density

$$\rho_{s,\ell} = 10.32 - 2.412 \times 10^{-4}\ T \quad gm/cm^3$$

Thermal diffusivity

$$\alpha_s = 0.5 - 1.1 \times 10^{-4}\ T \qquad cm^2/s$$

$$\alpha_\ell = 0.175 - 3 \times 10^{-6}\ T \qquad cm^2/s$$

Heat of fusion

6.65 kcal/gm-mole

Heat of vaporization

141.6 kcal/gm-mole

Vapor pressure

$$\log P = a + \frac{b}{T} \quad atm$$

$a = 7.2 \quad b = -33700 \quad 0 < T \leqslant 300°K$

$a = 6.34 \quad b = -31210 \quad 300°K < T$

A summary of the amount of material vaporized and the maximum thickness of the melted layer is given in Tables 4-1 and 4-2, respectively. Instead of addressing the details in the tables directly, we will begin by considering the effect of energy flux (J/cm^2) and disruption time on the Mo surface temperature for two starting temperatures (573°K and 873°K), and with or without the benefits of vapor shielding.

The first three Figs.4-6, 7, 8 reveal the calculated temperature increase in a Mo surface which is initially at 573°K. The vapor shielding effect has been neglected and the heat pulse time is 0.1, 0.5, and 1 msec. It is observed from these figures that the maximum surface temperature is reached in a very short time (~0.001 to 0.02 seconds) for the 0.1 msec pulse. The surface temperature reaches ~6400°K for the 200 J/cm^2 pulse, ~7000°K for 400 J/cm^2, ~7500°K for 500 J/cm^2, and ~7900°K for 1200 J/cm^2 (Fig.4-6). When the disruption is finished, the temperature drops very rapidly to the melting point while the melted layer solidifies. The length of time that the surface remains at the melting point ranges from 0.01 to 0.1 msec with the longest time associated with the lowest heat flux. This can be explained by the fact that most of the energy in the high energy flux case (e.g., 1200 J/cm^2) is expended in vaporization with little melting, while the opposite is true in the low heat flux cases. Finally, it takes an

additional millisecond or so for the surface to cool down to the original surface temperature.

The same general behavior is observed in the longer pulse loading cases (Figs.4-7, 8) with two exceptions. First, the maximum temperature is lower (e.g., ~6300°K for a 1 msec pulse vs. 7900°K for a 0.1 msec pulse, both at 1200 J/cm^2). Second, the surface temperature corresponding to the lowest energy flux studied (200 J/cm^2) never did reach the equilibrium value in the 0.5 and 1 msec pulses.

It can be seen from Figs.4-9, 10, and 11 that raising the operating temperature of the Mo from 573°K to 873°K had little effect on the maximum temperature achieved. On the other hand, the time required to freeze the melted layer is longer in the 873°K case because more material is melted when the starting temperature is higher.

The effect of the disruption time at constant energy flux on the surface temperature increase is shown in Figs.4-12 and 4-13 for $T_0 = 573$°K, and Figs.4-14 and 4-15 for $T_0 = 873$°K. For example, we see in Fig.4-12 that at 400 J/cm^2, the maximum temperature reached in a 0.1 msec pulse is ~7000°K versus only ~5500°K after a 1 msec pulse. The time spent at the melting point after the energy pulse is longer for the longer pulse because more energy goes into melting than into vaporization. The same general behavior is true for 800 J/cm^2 (Figure 4-13) and $T_0 = 873$°K (Figs.4-14, 4-15), and only the values are slightly changed.

The total time that the front surface stays molten is listed in Table 4-13 for a selected set of parameters.

It is important to note from Table 4-3 that these values (0.2 to 2.4 msec) represent the maximum time the front surface stays in the molten state. At distances which are farther back into the component, the time the Mo is molten is less than these numbers.

The effect of the blow-off vapor layer on the surface temperature increase is illustrated in Figs.4-16 through 4-21. For example, in Fig.4-16, we can see that the vapor shielding drops the maximum temperature from ~5500°K to ~4700°K during a 1 msec, 400 J/cm^2 pulse. The effect of vapor shielding on the 200 J/cm^2 pulse is less pronounced but the maximum surface temperature achieved is still reduced.
It should also be noted that for those two energy fluxes, the time the surface remains molten is shortened by vapor shielding.

There is a rather interesting "bump" in the surface temperature curves for the high heat flux cases when vapor shielding is included. This occurs because the increasing vapor layer thickness absorbs more of the incoming particles, thus lowering the transmitted heat flux to the front surface. Eventually, all of the particle energy is absorbed in the vapor layer and reradiated isotropically to the chamber walls. The lower heat flux causes the temperature to rise at a reduced rate, and the transition to the different slope results in the peculiarly shaped curve.

The time that the surface is molten is actually increased by vapor shielding for the very high heat fluxes because less energy is used for vaporization and more is used in melting the Mo. The total time the surface remains in the molten state for the 800 and 1200 J/cm^2 pulses is ~2 msec (Fig.4-17).

As the disruption time is shortened, the effect of vapor shielding becomes more pronounced (e.g., compare Figs.4-16 vs. 4-18 vs. 4-20 or 4-17 vs. 4-19 vs. 4-21). The vapor shielding actually increases the time in the molten state (i.e., thickness of melted layer) at 400 J/cm^2. When we consider the 0.1 msec disruption time, the duration of time in the molten state is lengthened for all the energy fluxes (Figs.4-20, 21).

When the base temperature is raised from 573°K to 873°K, the main effect is to slightly increase the maximum surface temperatures obtained while slightly extending the time in the molten state and hence the thickness of the molten layer (Figs.4-22 through 4-27).

The general effects of energy density, disruption time, and the effects of vapor shielding on the total amount of Mo vaporized are summarized in Fig.4-28. Some important observations from this figure are listed below.

- The threshold energy densities for significant evaporation (> 1 micron per pulse) are as follows:

No Vapor Shielding	With Vapor Shielding
270 J/cm^2 for 1 msec,	400 J/cm^2 for 1 msec,
190 J/cm^2 for 0.5 msec,	300 J/cm^2 for 0.5 msec,
150 J/cm^2 for 0.1 msec.	150 J/cm^2 for 0.1 msec.

- A thickness of the vaporized region of 30 microns per pulse is obtained for energy deposition of

No Vapor Shielding	With Vapor Shielding
550 J/cm and 1 msec,	1050 J/cm and 1 msec,
425 J/cm and 0.5 msec,	900 J/cm and 0.5 msec,
350 J/cm and 0.1 msec.	700 J/cm and 0.1 msec.

Finally, the effects of disruption time and energy on the maximum zone thickness is plotted in Fig.2-29. While the results displayed here are only for the case of an initial temperature of $T_0 = 573°K$, Table 4-2 shows that raising the starting temperature to 873°K has only a small effect on the melted zone thickness.

Important points from Figs.4-29 are listed below.

- The approximate threshold for a 1 micron melted zone thickness is

  120 J/cm^2 for 1 msec,
  100 J/cm^2 for 0.5 msec,
  75 J/cm^2 for 0.1 msec.

- The maximum thickness of the melted layer is obtained for energy deposition of

  400 J/cm^2 for 1 msec (100 microns),
  300 J/cm^2 for 0.5 msec (72 microns),
  150 J/cm^2 for 0.1 msec (35 microns).

- Vapor shielding does not effect the absolute magnitude of the maximum melt layer thickness, but it requires more energy to obtain it. For example,

  ~100 microns for 700 J/cm^2 of 1 msec,
  ~ 76 microns for 500 J/cm^2 at 0.5 msec.

- The vapor shielded cases show that increased melting will occur at higher energy fluxes. This is because the transmitted energy flux is less and more of this energy is used for melting than for vaporization as compared to the the unshielded case.

For INTOR parameters, the general effects of energy density, disruption time, and the effects of vapor shielding on the total amount of Mo vaporized and melting zone thickness are summarized in Figs.4-30 and 4-31.

Some important observations are listed below.

- The threshold for significant evaporation (> 1 micron per pulse) is approximately as follows:

No Vapor Shielding	With Vapor Shielding
860 J/cm^2 for 20 msec,	>1200 J/cm^2 for 20 msec,
630 J/cm^2 for 10 msec,	1050 J/cm^2 for 10 msec,
480 J/cm^2 for 5 msec.	800 J/cm^2 for 5 msec.

- The approximate threshold for a 1 micron melted zone thickness is

  550 J/cm^2 for 20 msec,
  390 J/cm^2 for 10 msec,
  280 J/cm^2 for 5 msec.

- Except for a 5 msec disruption without vapor shield, the melting zone thickness increases with energy density. Melting zone thickness for 5 msec (no vapor shield) reaches to saturation value of 210 microns at 680 J/cm^2.

- Vapor shielding effectively reduces the melting zone thickness for the energy ranges employed in this calculation.

4.3 Carbon

The thermophysical properties used for carbon are listed below.

Density

$$\rho = 1.8 \text{ gm/cm}^3$$

Specific heat

$$C_p = 0.093 + 4.8 \times 10^{-4}\ T - 1.33 \times 10^{-7}\ T^2 \quad \text{cal/gm°K}$$

$$500°K \leqslant T \leqslant 2000°K$$

$$C_p = 0.52 + 4.7 \times 10^{16}\ \frac{\exp[-8.9 \times 10^4/T]}{T^2} \quad \text{cal/gm°K}$$

$$T > 2000°K$$

Thermal conductivity

$$K = \frac{1.0}{2.4 + 3.46 \times 10^{-3}\ T + 8.5 \times 10^{11}\ \exp \frac{[-8.9 \times 10^4]}{T}} \quad \frac{cal}{cm \cdot S \cdot °K}$$

Enthalpy

$$H_v = 169.422 \ \frac{kcal}{g \cdot mole}$$

Vapor pressure

$$\log P = 9.73 - \frac{39924}{T} \ atm \qquad T \leqslant 1933°K$$

$$\log P = 8.975 - \frac{38463}{T} \ atm \qquad T > 1933°K$$

A summary of the amount of material vaporized is given in Table 4-4. It is instructive to examine the thermal behaviour of the graphite in a graphical manner before we address the full consequences of the proposed disruptions.

The first three Figs.4-32, 33, 34 show the increase of the surface temperature for 0.1, 0.5, and 1.0 msec disruption times, respectively. The general trends are the same regardless of the energy flux; the surface temperature rises to 4700 - 5000°K for 0.1 msec disruption, 4400 - 4700°K for 0.5 msec disruption, and 4200 to 4600°K for 1 msec disruption.

Figs.4-35 and 36 show how the surface temperature varies with disruption time for 400 and 800 J/cm^2 heat fluxes. As expected, the time above a given temperature (e.g., 1500°K) increases dramatically with the disruption time.

The effect of vapor shielding at 200 and 400 J/cm^2 is given in Figs.4-37, 38 and 39 for 0.1 msec, 0.5 msec, and 1.0 msec disruption times, respectively. Figs.4-40, 41, and 42 give the same data for 800 and 1200 J/cm^2. The general effect for vapor shielding is to slightly reduce the maximum surface temperature by 100 to 200°C. The vapor shielding also tends to keep the temperature of the front surface after the disruption above the value when no vapor shielding is considered.

Finally, Fig.4-43 compares the amount of carbon vaporized per shot with and without vapor shielding. As discussed previously, vapor shielding generally tends to reduce the evaporation. However, carbon is unique in that above a relatively low heat flux (200 to 600 J/cm^2)

the longer disruption times cause more carbon to evaporate than shorter times. This can be explained by the fact that the vapor produced by the shorter pulses is hotter because the lower conductivity of carbon allows less material to be heated. During the longer pulses, a larger volume of carbon is heated above the vaporization temperature, but the vaporized material is "cooler".

Next, Fig.4-44 compares the amount of carbon vaporized per shot for INTOR parameters. In this case, more material is vaporized for shorter disruption times, and vapor shielding effectively decreases the maximum evaporation thickness.

4.4 Titanium carbide

The thermophysical properties used for TiC are listed below.

Density

$$\rho_{s,\ell} = 4.6 \text{ g/cm}^3$$

Melting temperature

$$T_m = 3340°K$$

Heat of fusion

$$H_f = 5.55 \text{ kcal/g•mole}$$

Heat of vaporization

$$H_v = 113.2 \text{ kcal/g•mole}$$

Specific heat

$$C_{p,s} = 0.1915 + 1.48 \times 10^{-5} \, T \quad \text{cal/g°K}$$

$$C_{p,\ell} = 0.268 \quad \text{cal/g°K}$$

Thermal diffusivity

$$\alpha_s = 0.08179 + 6.83 \times 10^{-6} \, T \quad \text{cm}^2/\text{s}$$

$$\alpha_\ell = 0.1046 \quad \text{cm}^2/\text{s}$$

Vapor pressure

$$\log P = a + \frac{b}{T} \qquad a = 7.652, \quad b = -33600, \quad P \text{ in atm.}$$

The amount of TiC evaporated from the front surface and the maximum thickness of the melted layer are given in Table 4-5. Before we address the specific results of these calculations, it is instructional to examine the temperature response of the first surface.

Fig.4-45, 46, and 47 show how the surface temperature of the TiC depends on energy flux and disruption time if $T_0 = 573°K$ and if there is no vapor shielding.

The general features of the curves are the same as those previously calculated for 316 SS and Mo. Only a few general points are worth repeating at this time.

- The equilibrium temperatures are all reached before the end of the pulse, except for the 200 J/cm^2 - 1 msec case. In general, the equilibrium temperatures are reached in ~10% of the pulse duration.
- The magnitude of the temperature increase is proportional to the energy flux and inversely proportional to the pulse length. For example, the maximum surface temperatures reached for 0.1, 0.5 and 1 msec pulses are 6200°K, 5500°K, and 5200°K, respectively.
- Once the disruption is completed the temperature drops very rapidly to the melting temperature (within less than a microsecond). The length of time at the melting point depends on how much material is melted, but the longest time in the molten state after the energy pulse ceases is ~0.2 msec.
- The temperature returns to the initial value in roughly 0.1 - 4 msec.

The effect of increasing the initial temperature from 573 to 873°K is shown in Figs.4-48, 49, and 50. There appears to be very little effect, and the general features of the curves are the same at both starting temperatures.

The effect of disruption time is illustrated in Figs.4-51 and 4-52 for $T_0 = 573°K$ and in Figs.4-53 and 4-54 for $T_0 = 873°K$. It can be seen that for a given energy flux (400 or 800 J/cm^2) the maximum temperature is obtained with the shortest pulse. On the other hand, the time spent at the melting point after the disruption is longer for the longer pulses, indicating that more material is in the molten state.

Inclusion of the vapor shielding effect is depicted in Figs.4-55 to 4-60 for $T_0 = 573°K$. The effect of the vapor shielding is to reduce the maximum temperature attained but also to extend the time at the melting point. This behavior is indicative of a reduction in the

amount of material evaporated, and at the same time, of an increase in the thickness of the melted layer.

Figs.4-61 to 4-66 display the corresponding results for $T_0 = 873°K$. There is no major difference in the response of the TiC for the different starting temperatures.

A summary of the material evaporated as a function of energy density and disruption time is given in Fig.4-67. This figure, which shows the same general trends as the 316 SS and Mo, yields the following observations for the case of no vapor shielding.

- The threshold for significant vaporization of TiC is between 100 and 200 J/cm^2 for t = 0.1 to 1 msec.
- The amount of material evaporated is significantly higher (factors of 2 or more) compared to the case when the surface is shielded by the blow-off vapor.
- The effect of disruption time is reduced as the energy flux increases.

For the vapor shielded case:

- The threshold for vaporization is between 200 - 300 J/cm^2.
- The shorter the pulse duration, the more material is evaporated.

Finally, the effect of energy flux and disruption time on the maximum thickness of the melted layer is shown in Fig.4-68 with no vapor shielding and $T_0 = 573°K$. Observations from this figure are:

- A threshold for melting exists between 50 and 100 J/cm^2.
- A maximum in the melted layer thickness occurs at ~100 J/cm^2 for 0.1 msec, ~200 J/cm^2 for 0.5 msec, and around 300 J/cm^2 for 1 msec.
- The maximum thickness of the melted zone is ~20 microns per pulse at 0.1 msec, ~38 microns per pulse for 0.5 msec, and ~50 microns per pulse at 1 msec.
- The melted layer thickness is reduced as the energy flux increases because more energy is expended in vaporization.

The effect of including the vapor shielding is also shown in Fig.4-68. As in the previous cases, the vapor shielding;

- increases the threshold for melting;
- decreases the melting where the energy flux is below a characteristic value corresponding to the maximum value of the melt layer thickness.

- increases the melting at higher fluxes.

The increase at higher temperatures is obviously due to the increased amount of vaporization which reduces the energy available for melting. It is interesting to note that the maximum in the melt zone thickness is not altered by the inclusion of the vapor shielding, it is only displaced to higher energy fluxes.

It was discovered, after the present calculations were performed, that the values used for the heat of vaporization and melting might be too low. Information from Vier[14,15] suggests that the heat of fusion should be 16.9 kcal/mole, and the heat of vaporization should be 187 kcal/mole. Such changes in the thermal properties would be expected to reduce the magnitude of the melting and evaporation.

To test the sensitivity of the results to the heats of fusion and vaporization proposed by Vier, we reran the 400 and 800 J/cm^2 cases at 1 msec and $T_0 = 573°K$. The results are quoted below.

		Input from Section II		Vier Values of H_f, H_v	
		(w/o V.S.)	(with V.S.)	(w/o V.S.)	(with V.S.)
Evaporation	400 J/cm^2	33	7	22	4
	800 J/cm^2	91	35	67	24
Melting	400 J/cm^2	48	52	45	44
	800 J/cm^2	33	46	33	45

It is seen that the evaporation is the most sensitive property, resulting in a 30 - 40% reduction with the "new" values. However, the effect on the melting is minor, on the order of 10% or less. The net effect would be to bring the results for TiC closer to those for Mo with respect to evaporation, and to render TiC much better from the standpoint of total effected thickness. It is recommended that future work should try to establish a more reliable (or accepted) value for the heat of vaporization.

4.5 Silicon carbide

The thermophysical properties used for SiC are listed below.

Density

$\rho = 3.2$ g/cm^3

Melting point

SiC decomposes at 2700°C

Heat of vaporization

H_v = 125 kcal/g•mole

Specific heat

$$C_p = 13.25 - \frac{2035}{T} + \frac{288 \times 10^5}{T^2} \exp(-\frac{5600}{T})$$

$$\cong 13.25 - \frac{2035}{T} \qquad (cal/mole \cdot °K)$$

Thermal conductivity

k = 0.074 cal/gm•s•°C

Vapor pressure

$$\log P_{si}(torr) = -\frac{2.703 \times 10^4}{T} + 7.89298$$

A summary of the amount of material vaporized is given in Table 4-6 and plotted in Figs.4-69 and 4-70. There are several interesting observations to be made about the current results.

1. At 200 J/cm^2, significant evaporation only occurs for impulse times of 0.5 msec or shorter when vapor shielding is effective.
2. At 400 J/cm^2, the impulse time must be 1 msec or less to get significant evaporation.
3. At 800 J/cm^2, there was no evaporation during a 20 msec, vapor shielded pulse, but there was evaporation if no vapor shielding was considered.
4. The evaporation during a 1200 J/cm^2 pulse is significant for all pulse times studied, but the effect of vapor shielding is especially dramatic during the long heat pulse times.
5. If the heat flux is 20 ms long, and vapor shielded, then significant evaporation only occurs at very high energy fluxes (1200 J/cm).
6. At the high energy fluxes we find again that the amount of material evaporated goes through a maximum at about 0.5 to 1 msec pulse lengths.

4.6 Discussions

Typical results for the evaporation, melting, and total thicknesses are summarized in Table 4-7 for 0.1 ~ 1 msec - 200 J/cm^2, Table 4-8 for 5 ~ 20 msec - 200 J/cm^2, and Table 4-9 for 5 ~ 20 msec - 400 J/cm^2. In these tables, the total thickness is defined as the sum of the evaporation and melting thicknesses. We assume that a permissible erosion thickness is 10 μm per disruption, equivalent to 1 cm per 1000 disruptions.

In the case of 0.1 ~ 1 msec - 200 J/cm^2, C and SiC perform the best, except for SiC under the condition of 0.1 msec disruption time and no vapor shield. In this exceptional case, the erosion thickness exceed the permissible value. On the other hand, the erosion thickness of TiC and Mo depend on whether the melt layer is removed by various forces or not, that is, whether the melt layer is stable. If it is TiC and Mo perform favorably except for the condition of 0.1 msec disruption and no vapor shielding. In this exceptional case, the erosion thicknesses are at most 20 μm. If the melt layer is unstable, the erosion thickness of TiC and Mo are 22 ~ 67 μm, where the major part is the melting thickness. In the case of 5 ~ 20 msec - 200 J/cm^2, only 316 SS shows a high melting thickness of 45 ~ 100 μm because of its low melting point and a low evaporation thickness of 4 μm. On the other hand, total erosion thicknesses of C, SiC and Mo are less than 1 μm. A similar trend is shown in Table 4-9 for 5 ~ 20 μm - 400 J/cm^2. In this case, C and SiC are most favorable and, 316 SS and Mo are not. Maximum erosion thicknesses of 316 SS and Mo depend on the melt layer stability.

This stability has been investi ated by Wolfer and Hassanein by considering a Rayleigh-Taylor instability as the mechanism of the melt layer removal[16]. The results show that the stability strongly depends on the magnitude of the electromagnetic force. In the case of 316 SS and Mo under 5 msec disruption and 400 ~ 1200 J/cm^2, it can be concluded that the melt layer remains stable for the lower value of the electromagnetic force of 1 MN/m^3. Marginal stability or approaching instability is obtained for medium values of the force around 10 MN/m^3, whereas melt removal is certainly indicated for the highest value of the force around 100 MN/m^3. Since the electromagnetic force vary approximately as the inverse of the resistivity, the melt layer of

316SS is more stable than Mo. For an exact assessment, the calculation should be performed using detailed machine parameters.

Results from the calculations with the different initial temperatures for Mo and TiC show that there are no large difference between the erosion thicknesses at the initial temperatures of 573°K and 873°K. However, if first wall, limiter and divertor plate are cooled by only thermal radiation, an increase of the erosion thickness is expected when the initial temperature reaches around 2000°K.

Whereas the mechanisms of the erosion considered in this model are thermal vaporization and melting, it is expected that in the actual environment the chemical reaction with energetic hydrogen increase the erosion thickness for carbon and carbides. The chemical sputtering of C[17,18,19], SiC[20,21,22] and TiC[23] at temperatures of between 300 and 1200°K have been studied previously. The results show that the chemical sputtering of carbon has the maximum value of 7×10^{-2} atoms/ion around 800 ~ 900°K. The sputtering yields of carbides are about one order of magnitude less than that of carbon, and have small temperature dependencies. The maximum values are 6×10^{-3} atoms/ion[22] and 1×10^{-2} atoms/ion[21] for SiC, and 3×10^{-3} atoms/ion for TiC. Rough estimates show that the erosion yield due to the chemical sputtering at 300 ~ 1200°K is less than 1 μm, but it depends on the particle flux during a disruption. However, since the surface temperature during a disruption easily reaches to 3000 ~ 6000°K, the chemical reaction at these high temperature range should be considered in future model developments.

Above 1200°K, little data is available for the chemical reaction rates. Recently, the erosion of carbon due to bombardment with energetic ions has been measured at temperatures up to 2000 ~ 2200°K by Roth et al.[24] and Philipps et al.[25]. These results show that at these temperature the erosion yields are a factor 20 ~ 40 higher than the values at room temperature. Such a high erosion yield is considered to be due to an enhanced evaporation activated by the ion bombardment. Using these value, it is expected that the erosion of carbon increase significantly over that of thermal evaporation. On the other hand, chemical sputtering process is compound materials such as B_4C, SiC and TiC is more complicated. Recent result of heat treatment experiment up to 1000°C under ultra-high vacuum show that TiC was the most stable under heat loads, and a stoichiometric composition was maintained up to 1000°C, whereas a large segregation of carbon was observed in B_4C

and SiC[26]. In the case of compound materials, an enhanced evaporation similar to carbon is also expected. In the future, models which include the above effects are needed.

Finally, we remark on the vapor shielding model. In this study, we assume that the incoming plasma ions are stopped in the condensed material if the evaporated thickness is greater than the range of plasma ions. The range was calculated under the assumption that the stopping powers for liquid and gas are the same as the one for the solid. However, the actual phenomena are more complex than in model with the above assumptions. In addition to the vapor shield, vapor transport should also be considered. Vapor transport implies that some of the vaporized materials is ionized and swept away by the toroidal magnetic field. Although in the future, a more refined model is required a sensitivity analysis involving the effectiveness of the vapor shield and the vapor transport has been carried out, and it will be disucssed in the following chapter 5.

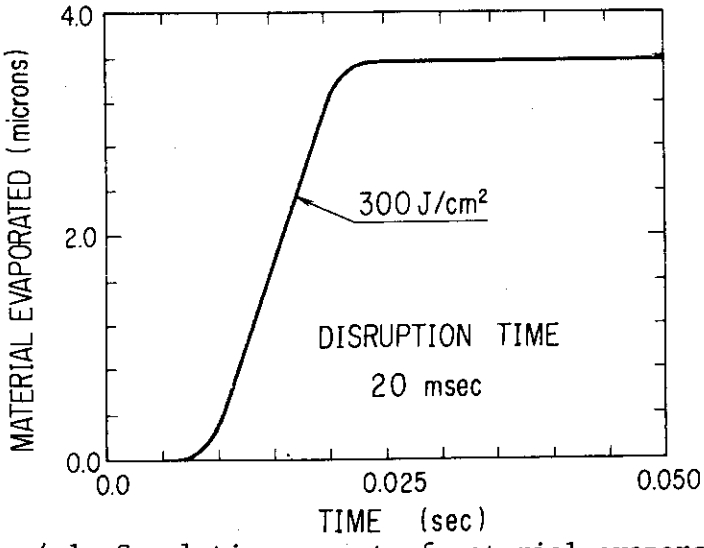

Fig. 4-1 Cumulative amount of material evaporated. (300 J/cm^2, 20 ms disruption)

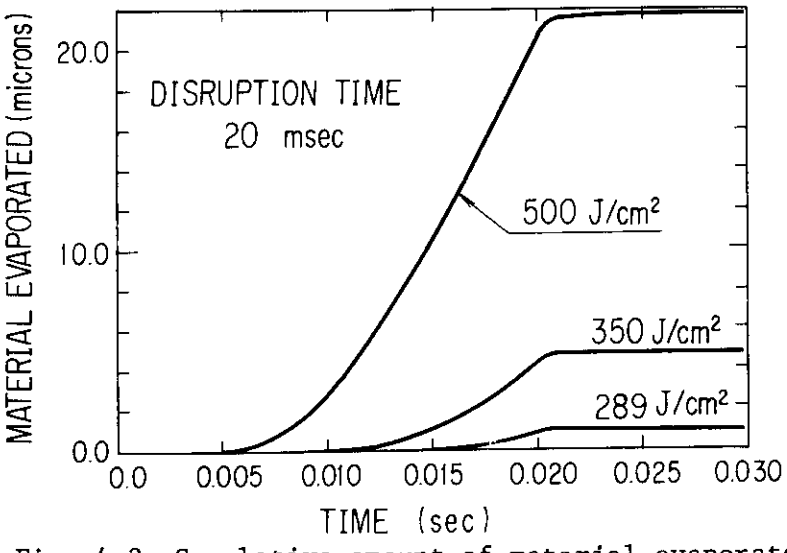

Fig. 4-2 Cumulative amount of material evaporated. (289, 350, 500 J/cm^2, 20 ms disruption)

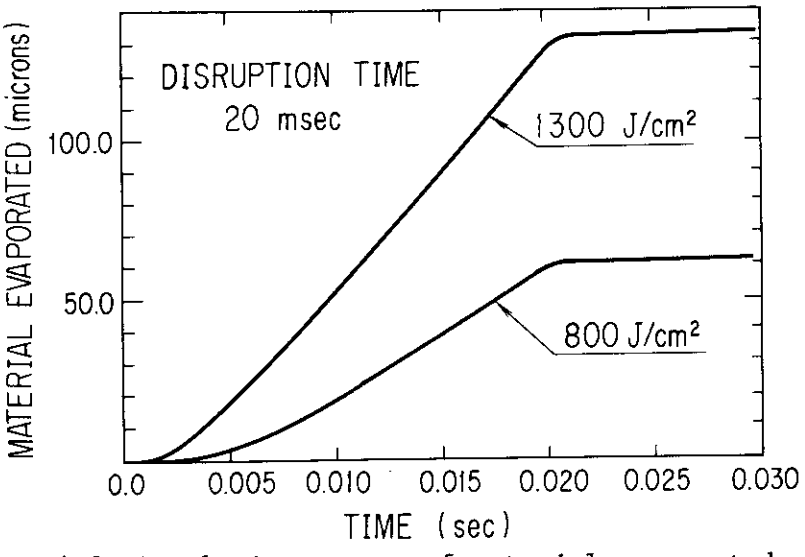

Fig. 4-3 Aumulative amount of material evaporated. (800, 1300 J/cm^2)

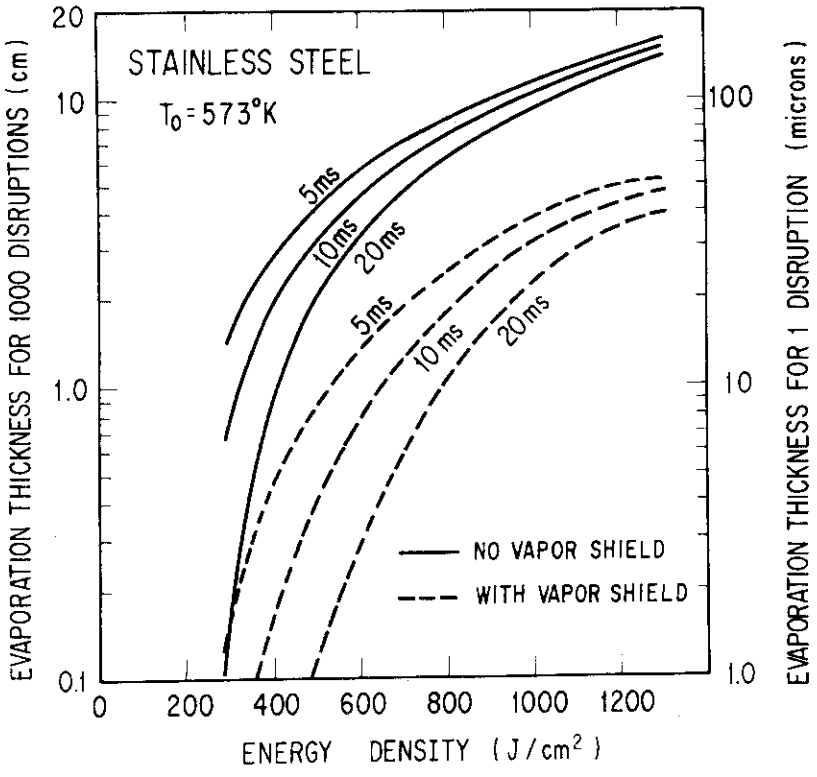

Fig. 4-4 Evaporation thickness of stainless steel for different energy deposited and disruption time (5, 10 and 20 msec).

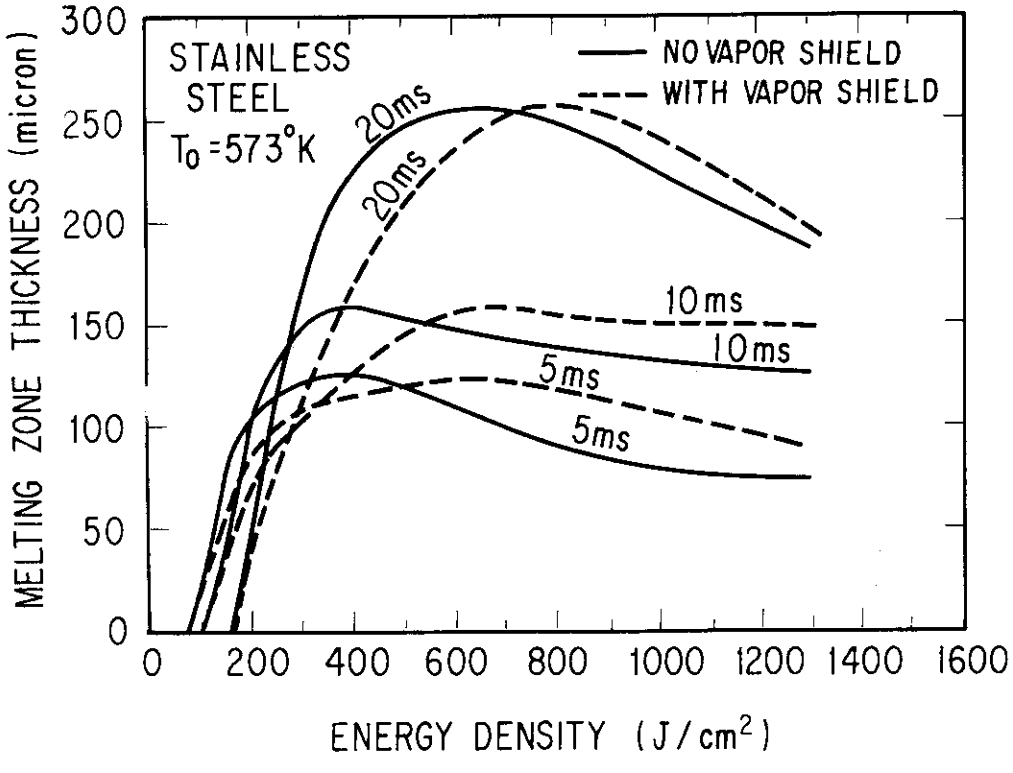

Fig. 4-5 Melt layer thickness of stainless steel for different energy deposited and disruption time (5, 10 and 20 msec).

Table 4-1 Effect of heat flux on the vaporization thickness.

Molybdenum Evap. Thickness (μm)		0.1 msec		0.5 msec		1.0 msec	
Energy Flux (J/cm^2)	Initial Temp.(°K)	Vapor Shield w/o	with	Vapor Shield w/o	with	Vapor Shield w/o	with
200	573	11.8	2.4	2.2	0.1	0.1	0.3
	873	12.6	2.8	3.1	0.0	0.3	0.4
400	573	34.0	12.7	22.8	4.0	14.7	0.9
	873	35.1	13.4	24.6	4.9	16.7	1.4
800	573	75.4	34.6	68.0	24.5	60.1	17.3
	873	77.4	35.6	70.4	26.1	63.0	19.1
1200	573	116	55.7	112	47.0	105	39.4
	873	118	57.0	115	48.9	109	41.7

Table 4-2 Effect of heat flux on the maximum melt layer thickness.

Molybdenum Melt. Thickness (μm)		0.1 msec		0.5 msec		1.0 msec	
Energy Flux (J/cm^2)	Initial Temp.(°K)	Vapor Shield w/o	with	Vapor Shield w/o	with	Vapor Shield w/o	with
200	573	34	37	65	44	57	49
	873	36	39	74	54	70	57
400	573	24	34	69	72	99	84
	873	27	35	72	79	106	95
800	573	15	24	54	69	85	99
	873	16	27	57	72	89	109
1200	573	10	19	39	59	69	90
	873	11	22	42	64	74	106

Table 4-3 Time front molybdenum surface stays molton.

Energy Flux (J/cm^2)	Disruption Time (msec)	Time front M_o surface stays molten.(msec) $T_0 = 573$ °K	$T_0 = 873$ °K
400	0.1	0.2	0.2
	0.5	1.0	0.8
	1.0	2.0	1.9
800	0.1	0.2	0.2
	0.5	1.3	0.9
	1.0	2.4	2.1

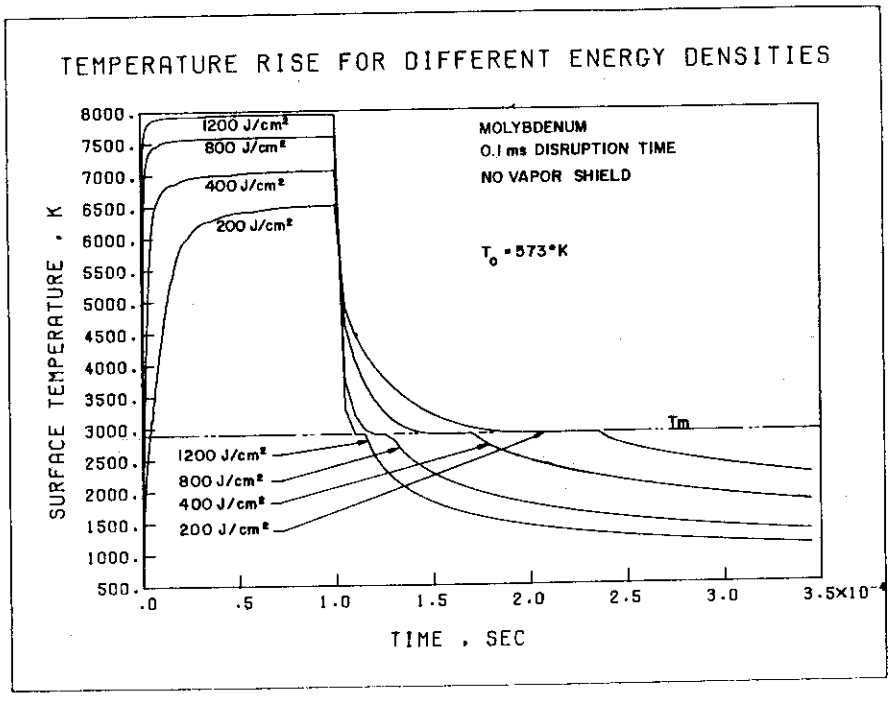
TEMPERATURE RISE FOR DIFFERENT ENERGY DENSITIES
MOLYBDENUM
0.1 ms DISRUPTION TIME
NO VAPOR SHIELD
T_0 = 573°K
1200 J/cm²
800 J/cm²
400 J/cm²
200 J/cm²
Tm
SURFACE TEMPERATURE , K
TIME , SEC

Fig. 4-6

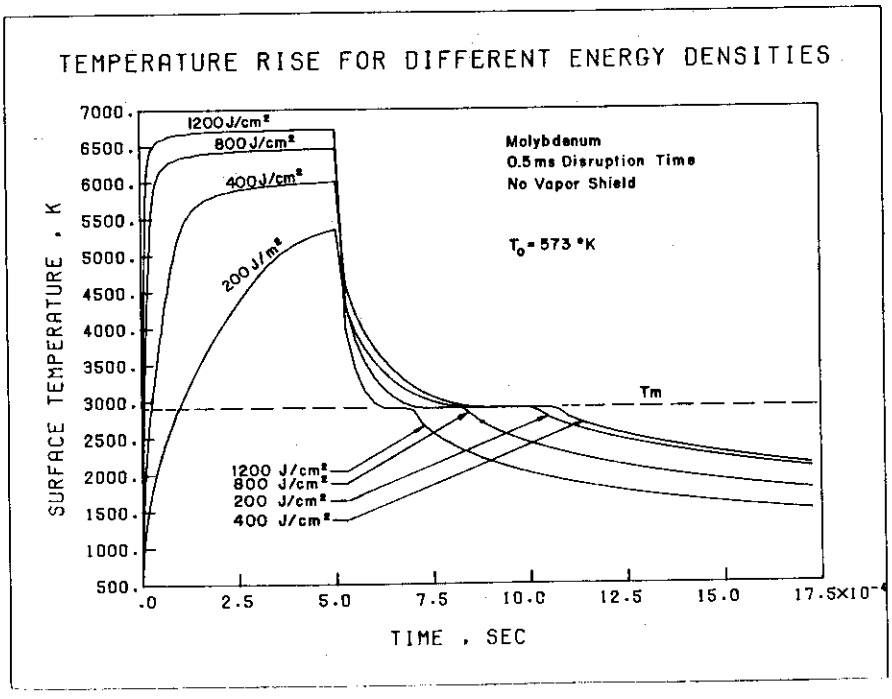
TEMPERATURE RISE FOR DIFFERENT ENERGY DENSITIES
Molybdenum
0.5 ms Disruption Time
No Vapor Shield
T_0 = 573 °K
1200 J/cm²
800 J/cm²
400 J/cm²
200 J/cm²
Tm
SURFACE TEMPERATURE , K
TIME , SEC

Fig. 4-7

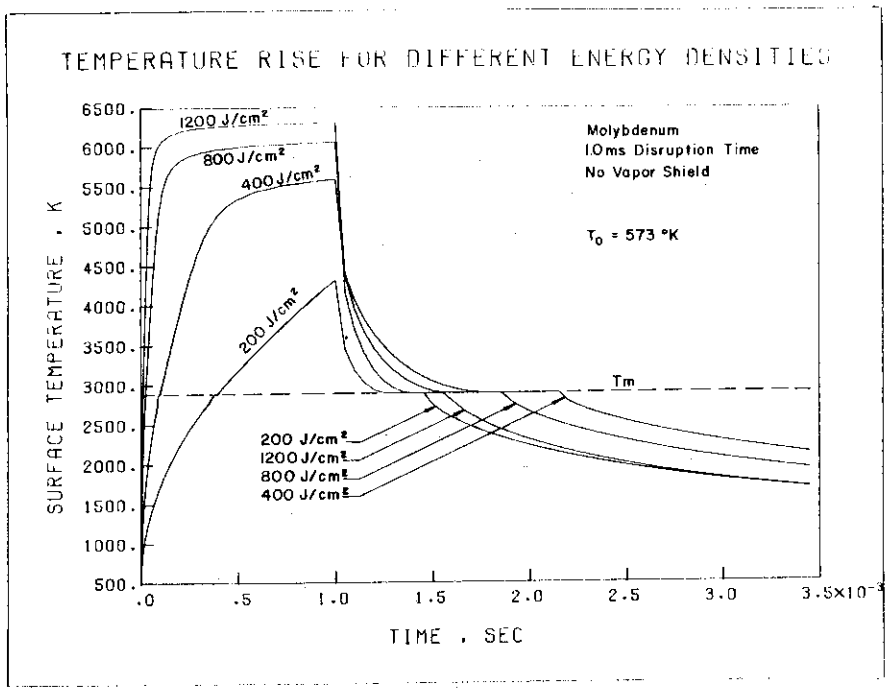
TEMPERATURE RISE FOR DIFFERENT ENERGY DENSITIES
SURFACE TEMPERATURE , K
TIME , SEC
1200 J/cm²
800 J/cm²
400 J/cm²
200 J/cm²
Molybdenum
1.0ms Disruption Time
No Vapor Shield
T₀ = 573 °K
Tm
200 J/cm²
1200 J/cm²
800 J/cm²
400 J/cm²
6500.
6000.
5500.
5000.
4500.
4000.
3500.
3000.
2500.
2000.
1500.
1000.
500.
.0
.5
1.0
1.5
2.0
2.5
3.0
3.5x10⁻³

Fig. 4-8

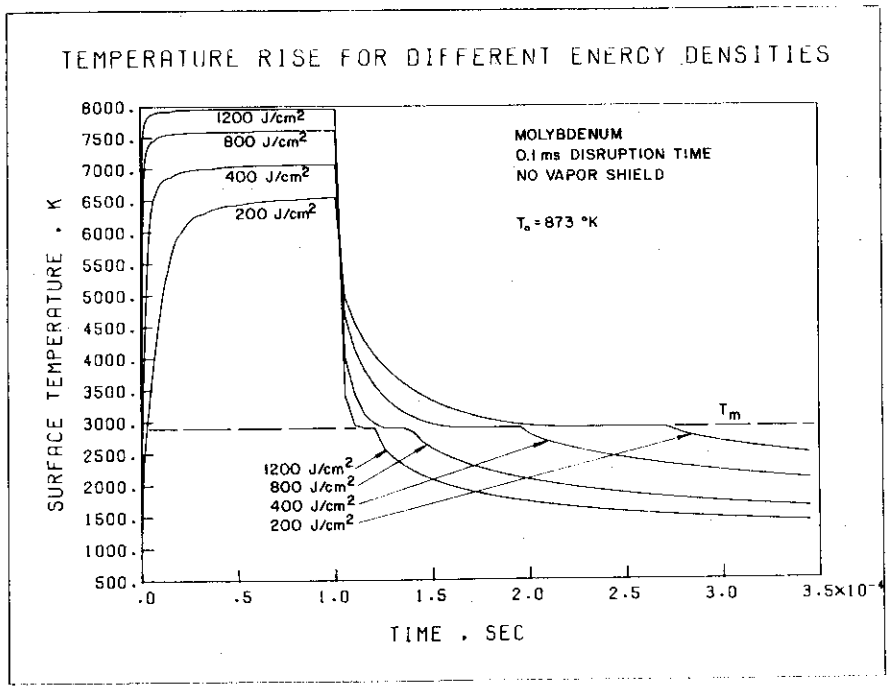
TEMPERATURE RISE FOR DIFFERENT ENERGY DENSITIES
SURFACE TEMPERATURE , K
TIME , SEC
1200 J/cm²
800 J/cm²
400 J/cm²
200 J/cm²
MOLYBDENUM
0.1 ms DISRUPTION TIME
NO VAPOR SHIELD
T₀ = 873 °K
Tm
1200 J/cm²
800 J/cm²
400 J/cm²
200 J/cm²
8000.
7500.
7000.
6500.
6000.
5500.
5000.
4500.
4000.
3500.
3000.
2500.
2000.
1500.
1000.
500.
.0
.5
1.0
1.5
2.0
2.5
3.0
3.5x10⁻⁴

Fig. 4-9

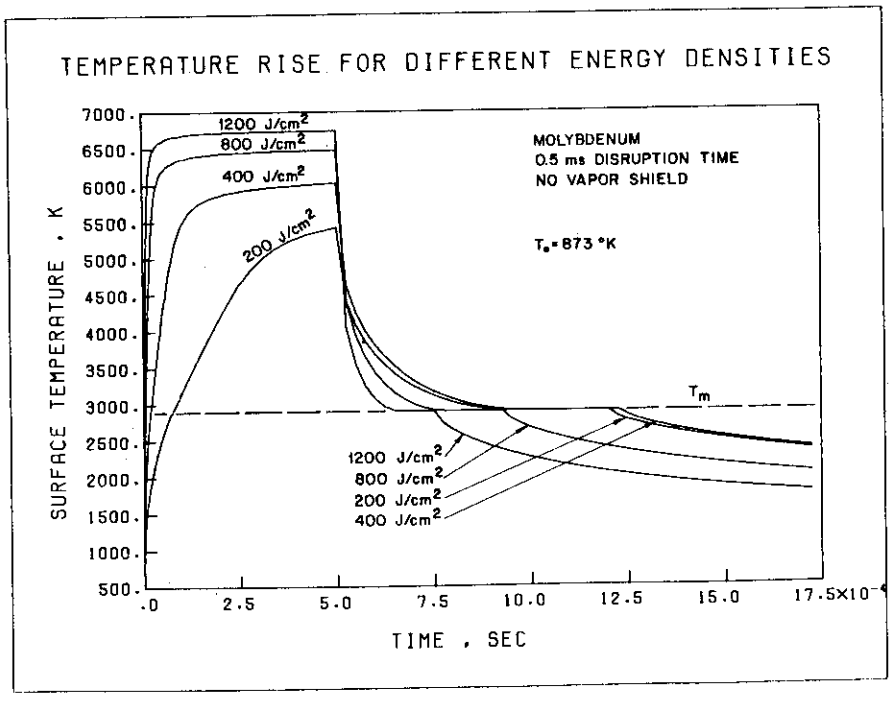

Fig. 4-10

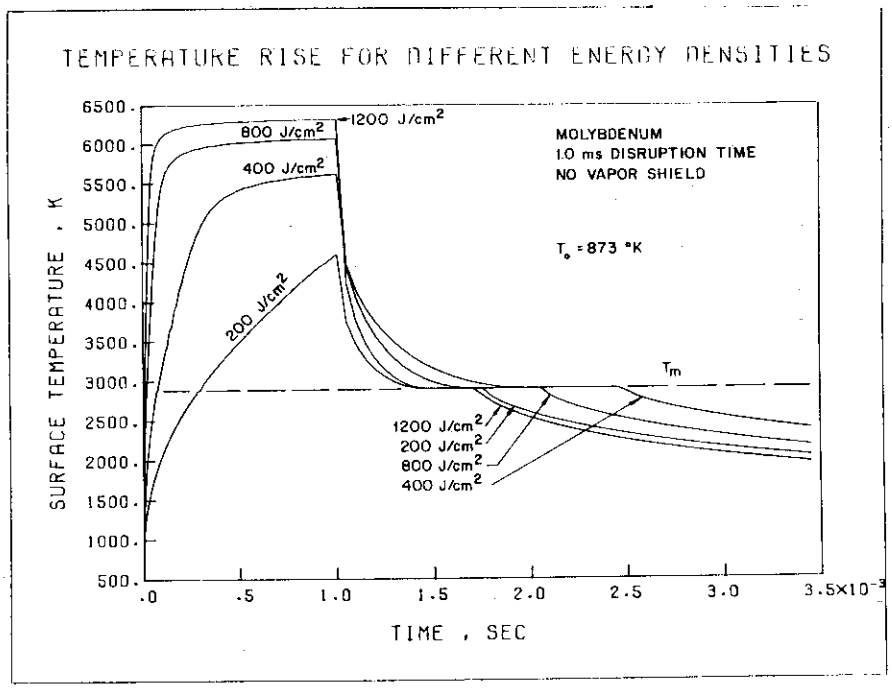

Fig. 4-11

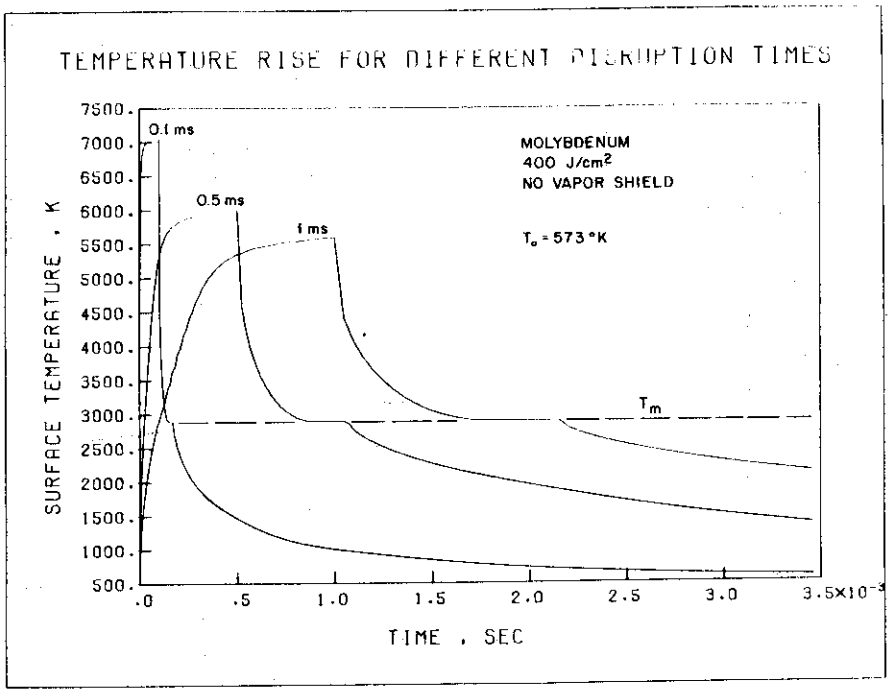

Fig. 4-12

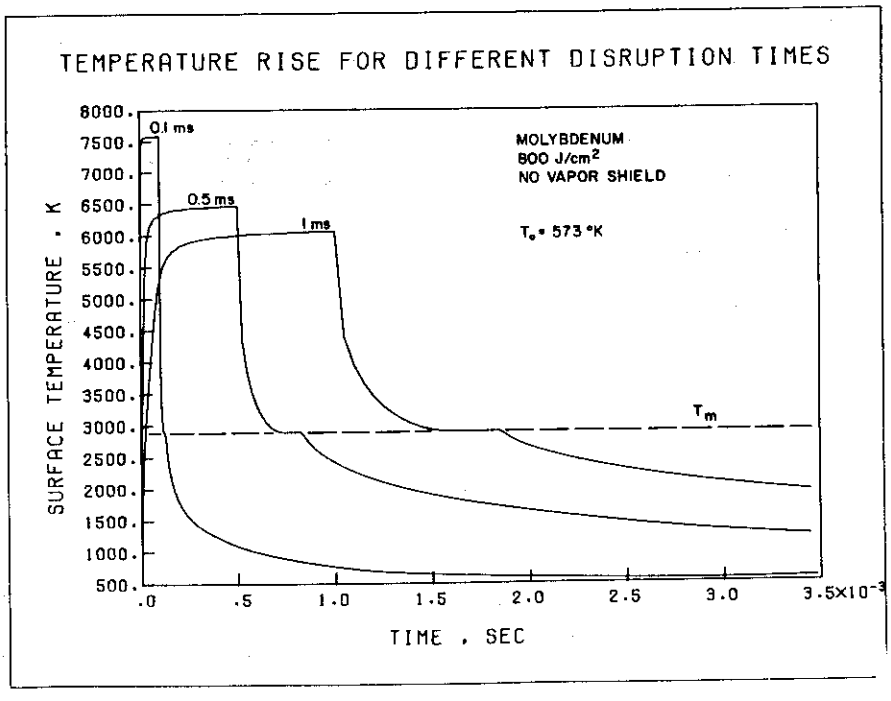

Fig. 4-13

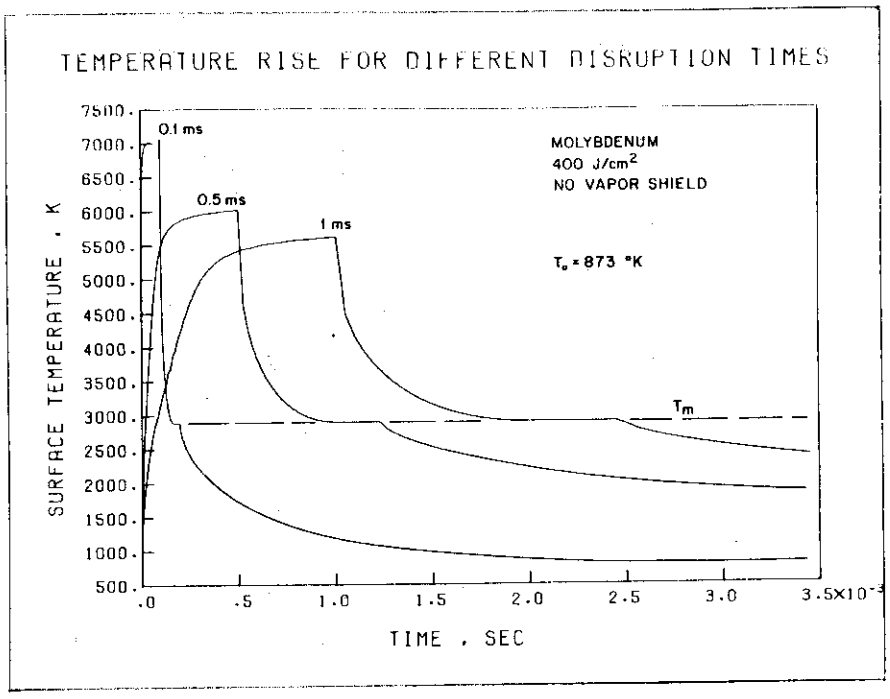

Fig. 4-14

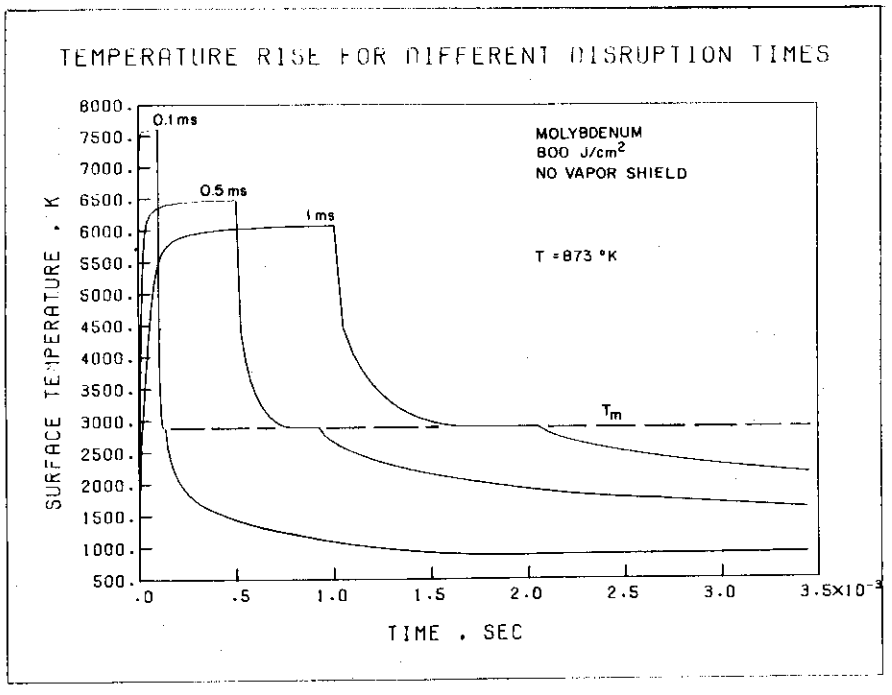

Fig. 4-15

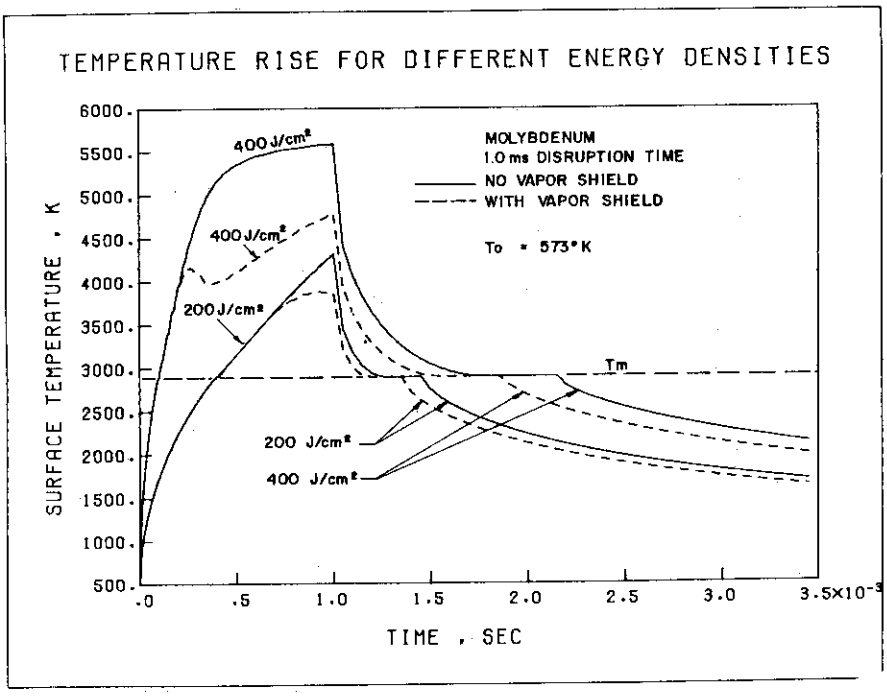

Fig. 4-16

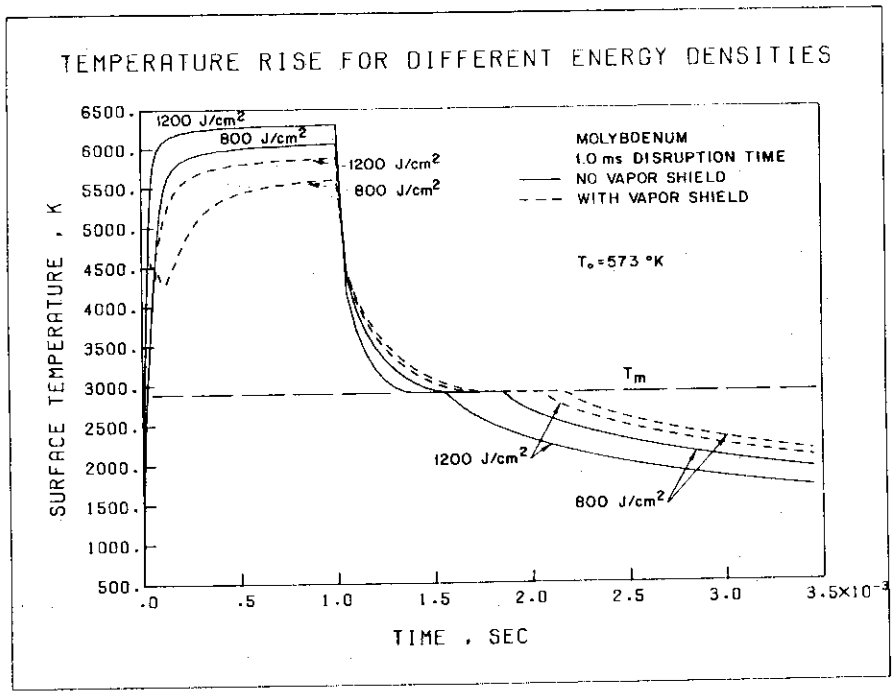

Fig. 4-17

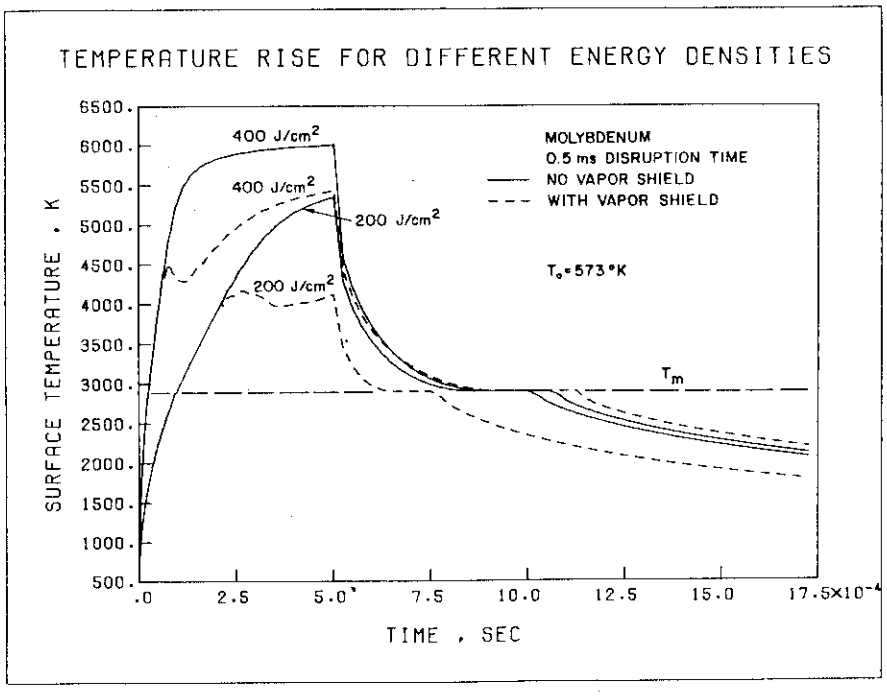

Fig. 4-18

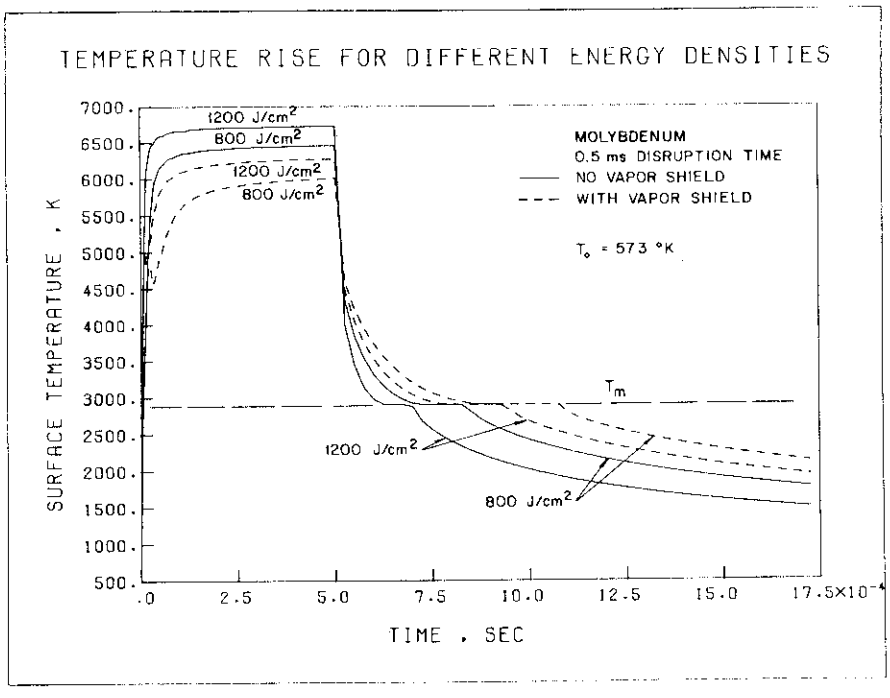

Fig. 4-19

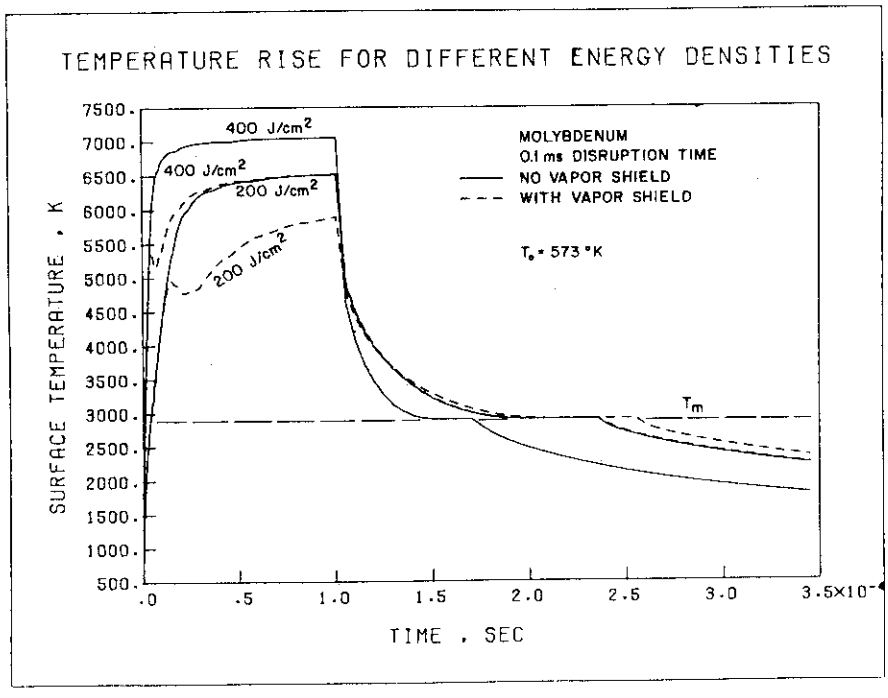

Fig. 4-20

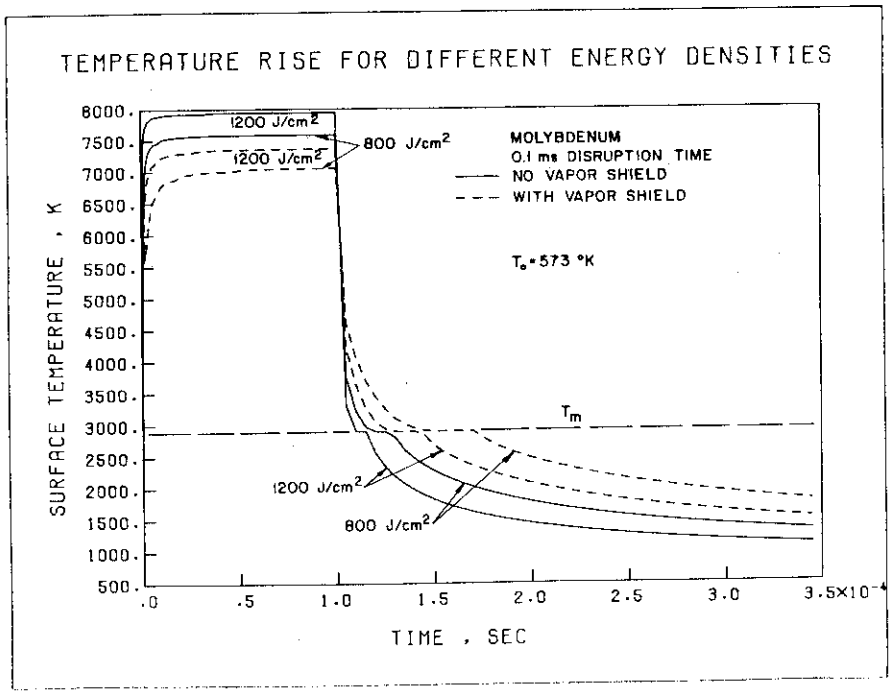

Fig. 4-21

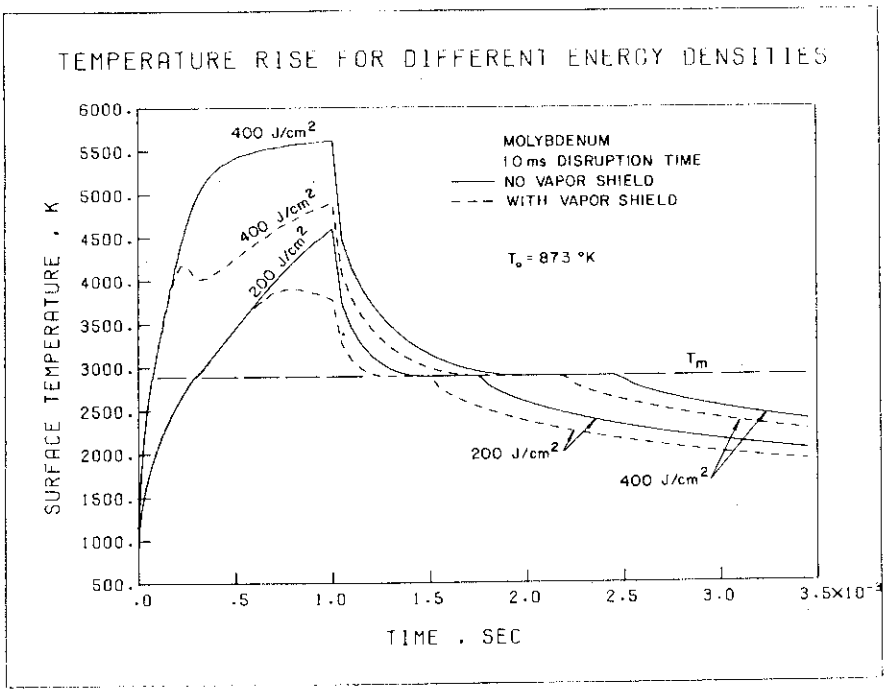

Fig. 4-22

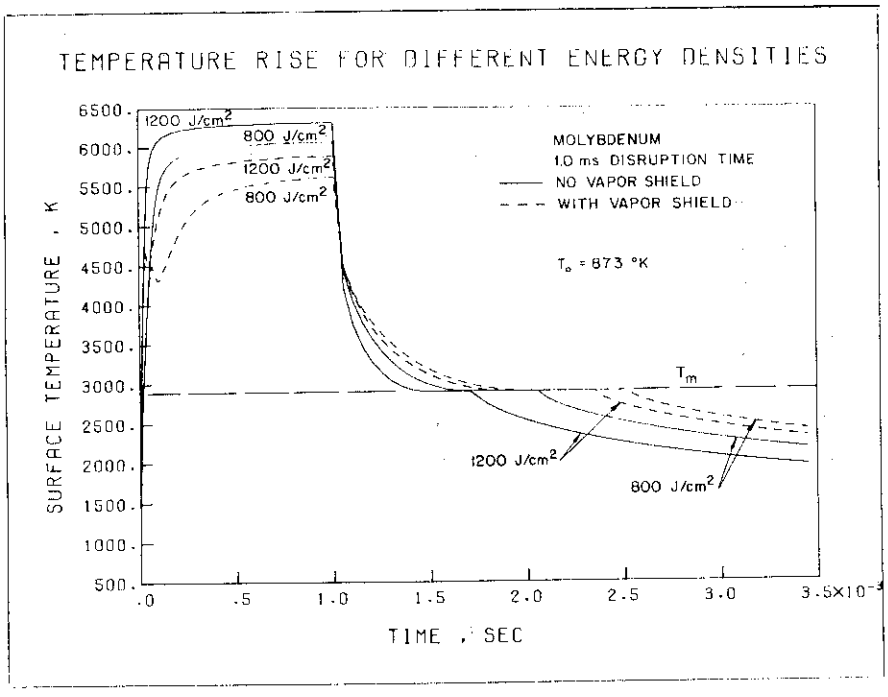

Fig. 4-23

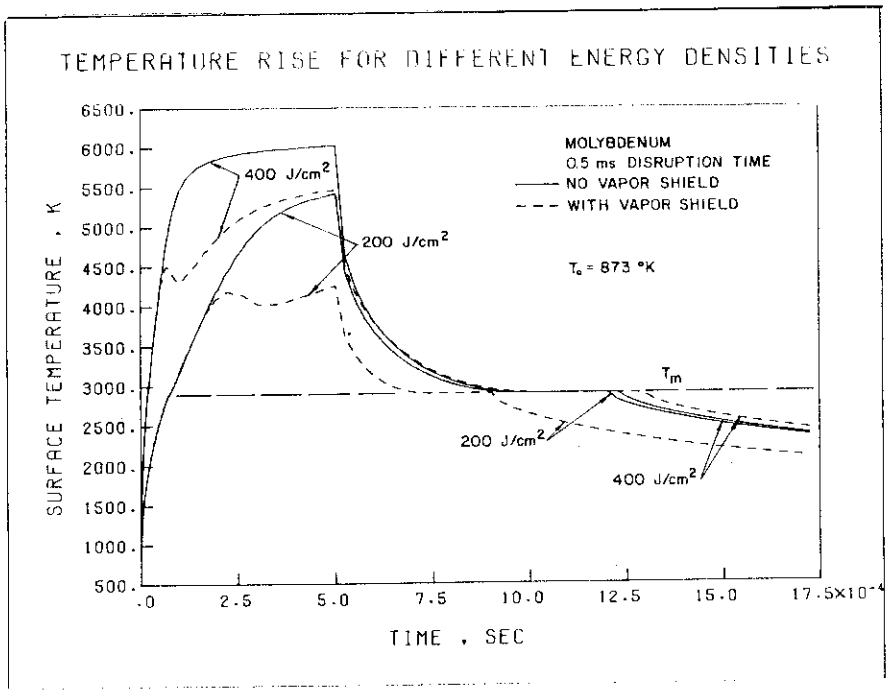

Fig. 4-24

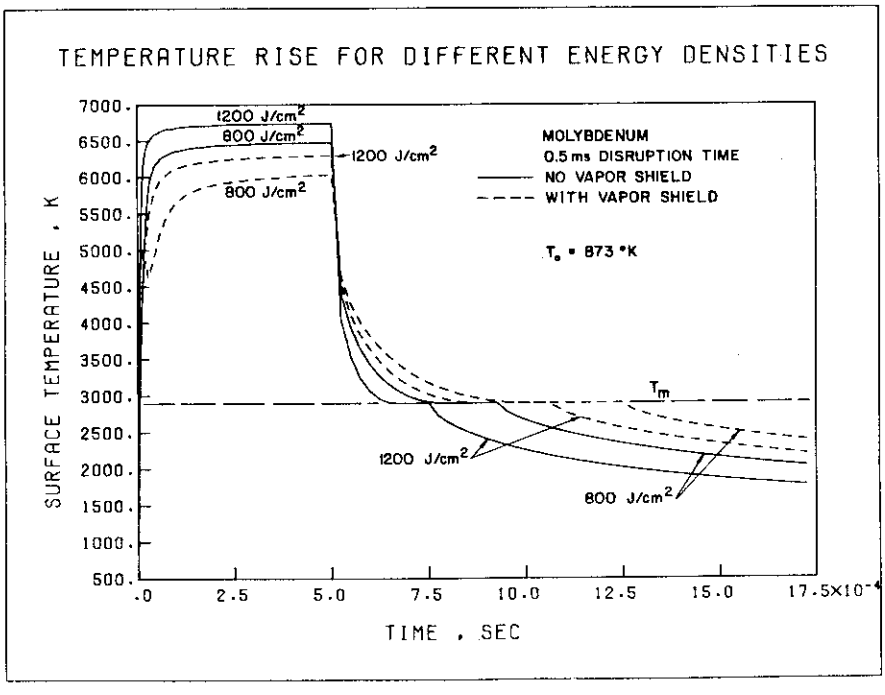

Fig. 4-25

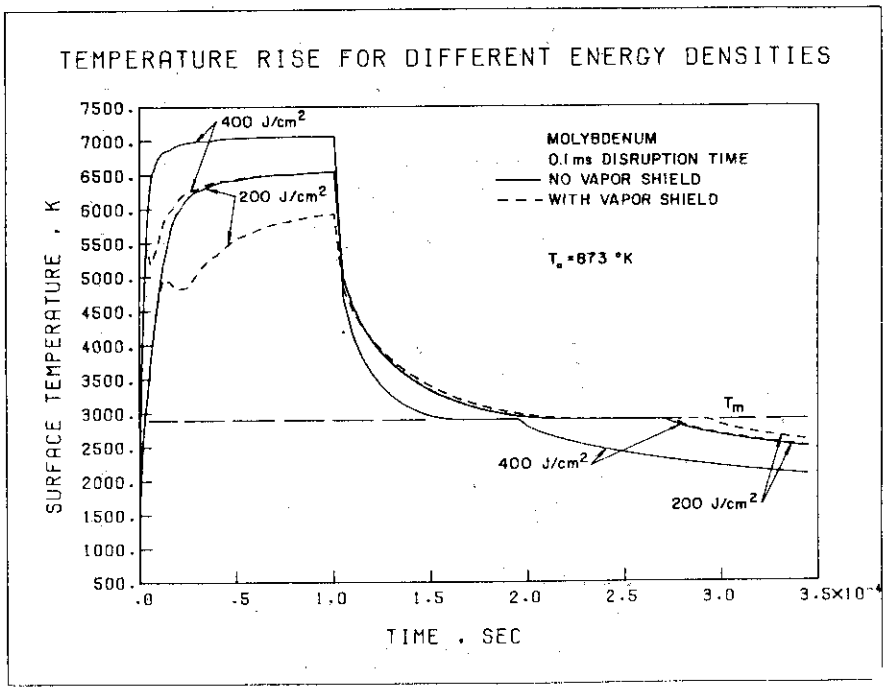

Fig. 4-26

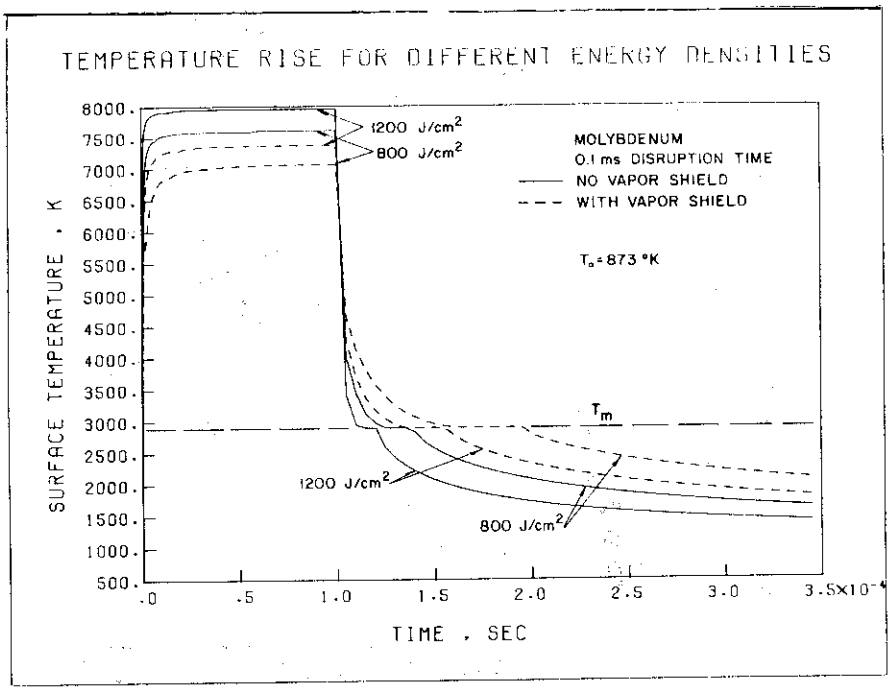

Fig. 4-27

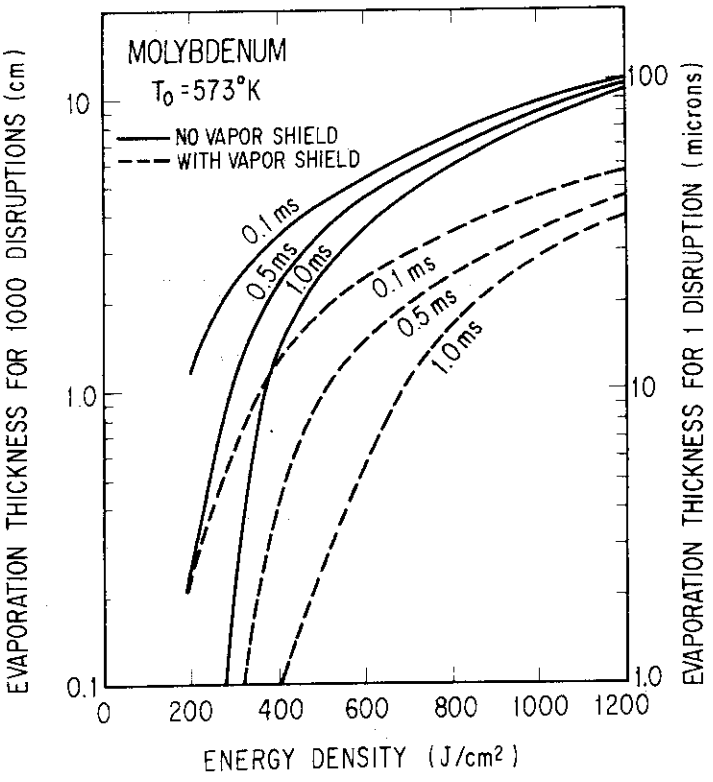

Fig. 4-28 Evaporation thickness of molybdenum for different energy deposited and disruption time (0.1, 0.5 and 1.0 msec).

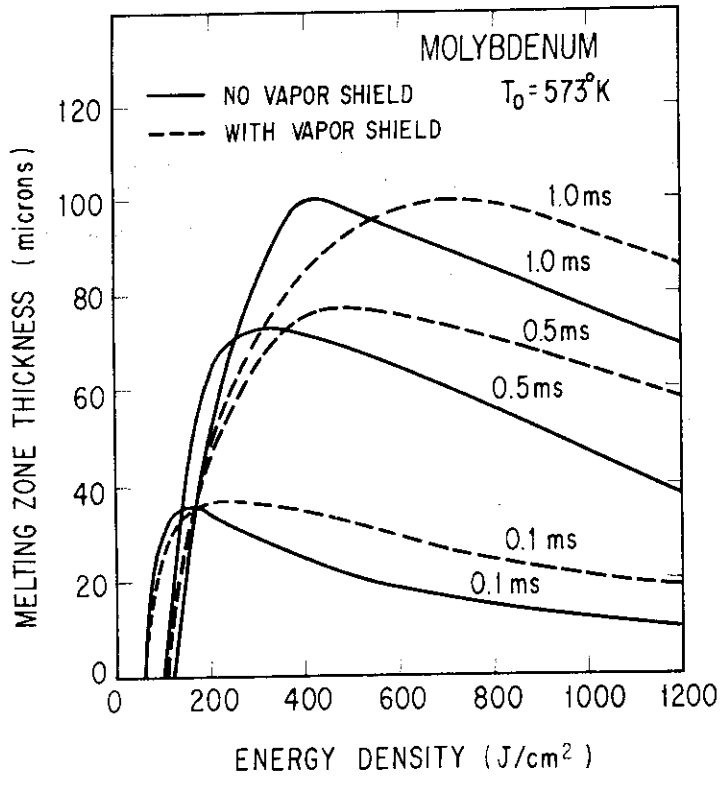

Fig. 4-29 Melt layer thickness of molybdenum for different energy deposited and disruption time (0.1, 0.5 and 1.0 msec).

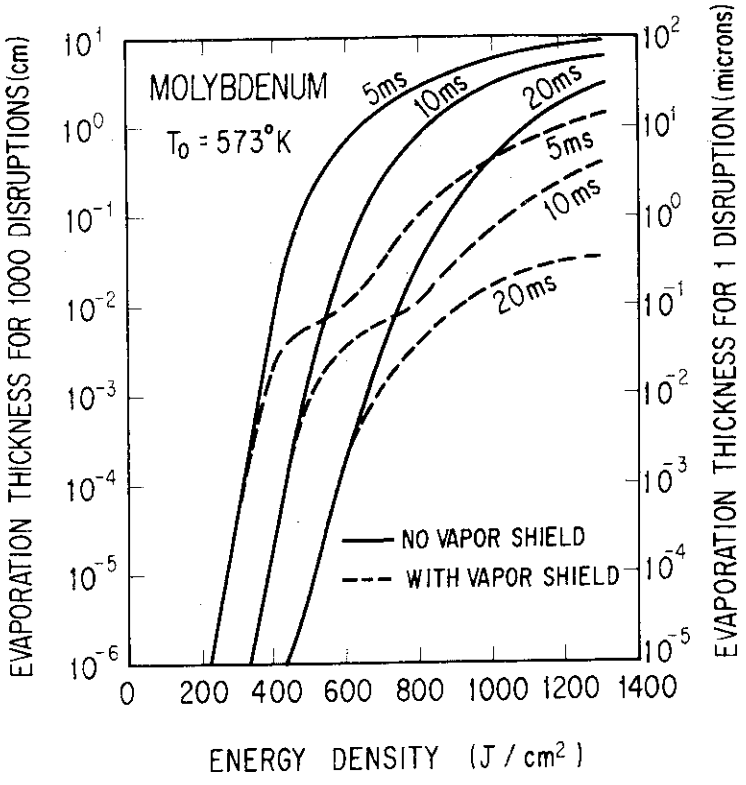

Fig. 4-30 Evaporation thickness of molybdenum for different energy deposited and disruption time (5, 10 and 20 msec).

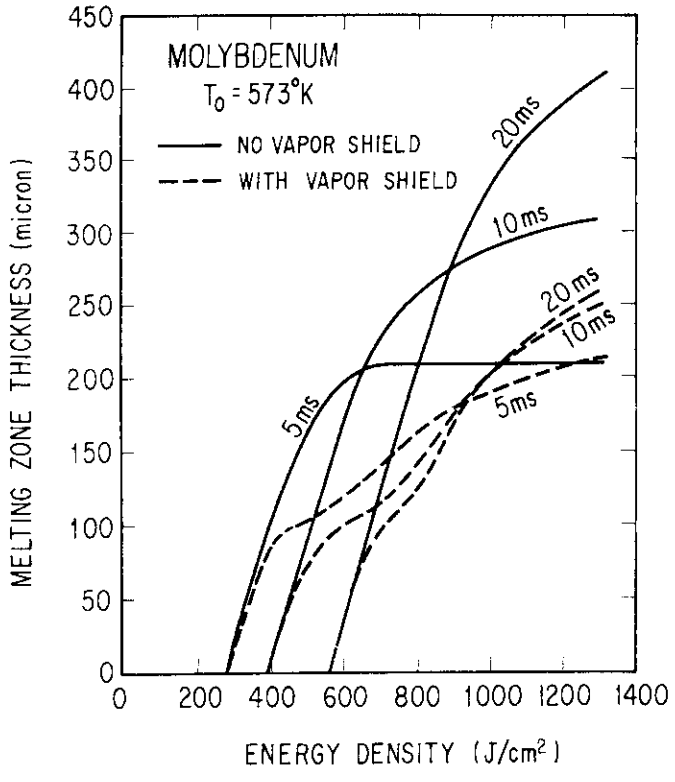

Fig. 4-31 Melt layer thickness of molybdenum for different energy deposited and disruption time (5, 10 and 20 msec).

Table 4-4 Effect of heat flux on the vaporization thickness of carbon (μm).

Carbon Evap. Thickness (μm)		0.1 msec		0.5 msec		1.0 msec	
Energy Flux (J/cm²)	Initial Temp.(°K)	Vapor Shield w/o	Vapor Shield with	Vapor Shield w/o	Vapor Shield with	Vapor Shield w/o	Vapor Shield with
200	573	6.8	3.7	7.7	2.2	5.8	0.8
400	573	11.2	7.0	18.0	8.4	18.7	6.9
800	573	17.1	11.4	32.3	18.4	38.7	19.4
1200	573	21.5	14.6	43.0	26.1	54.0	30.0

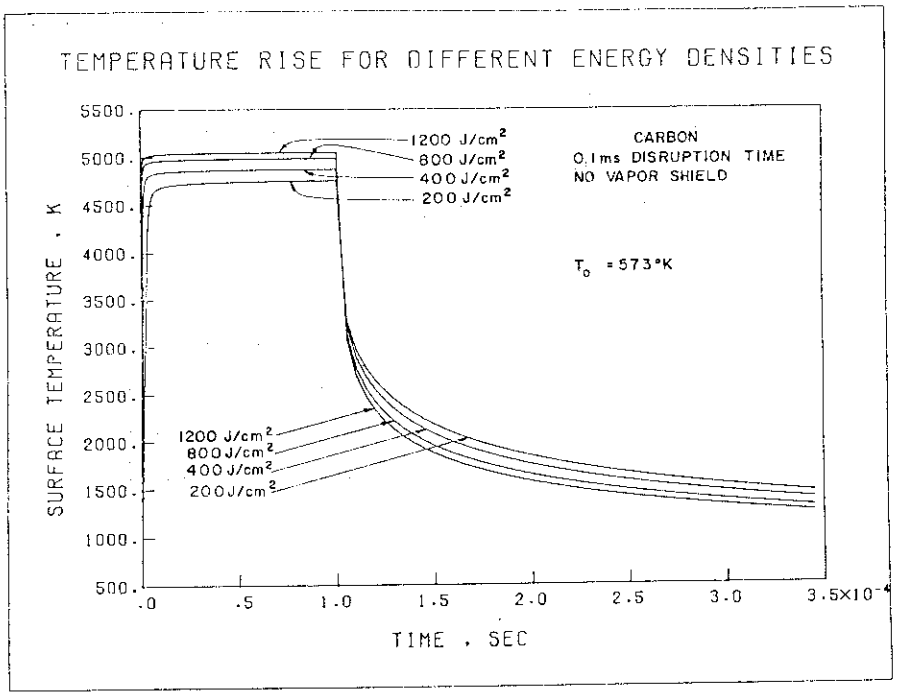

Fig. 4-32

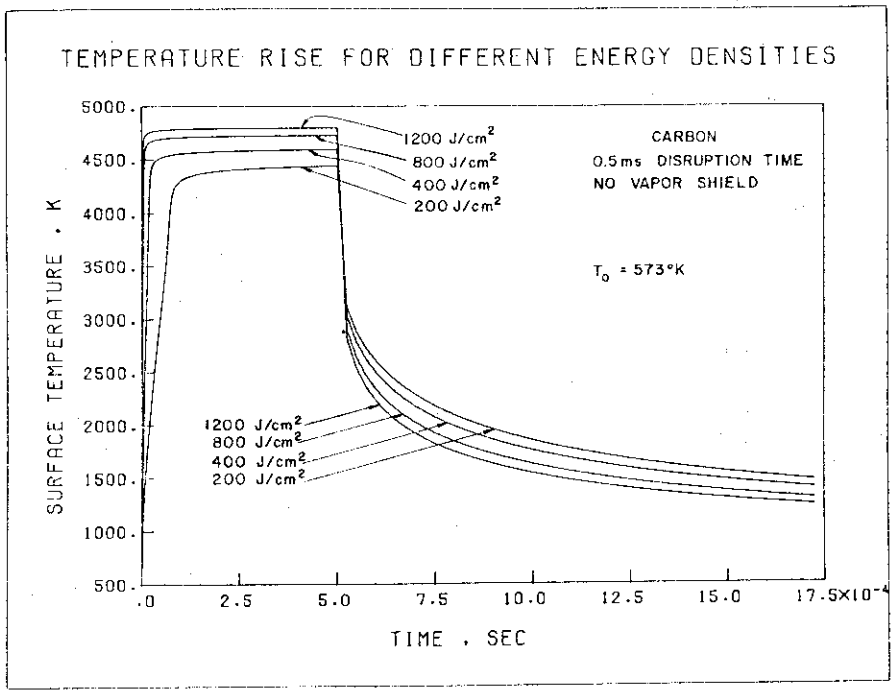

Fig. 4-33

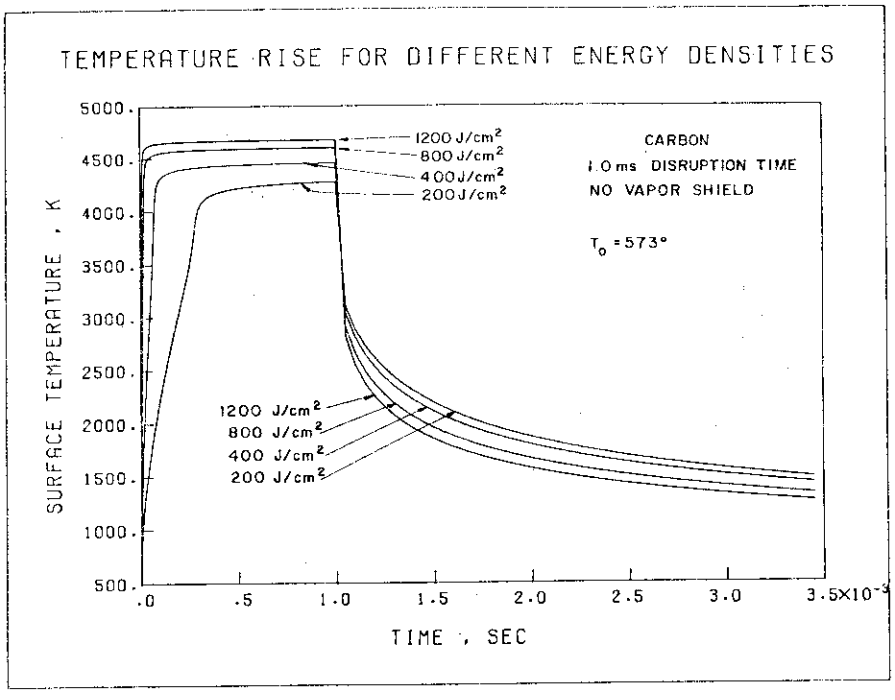

Fig. 4-34

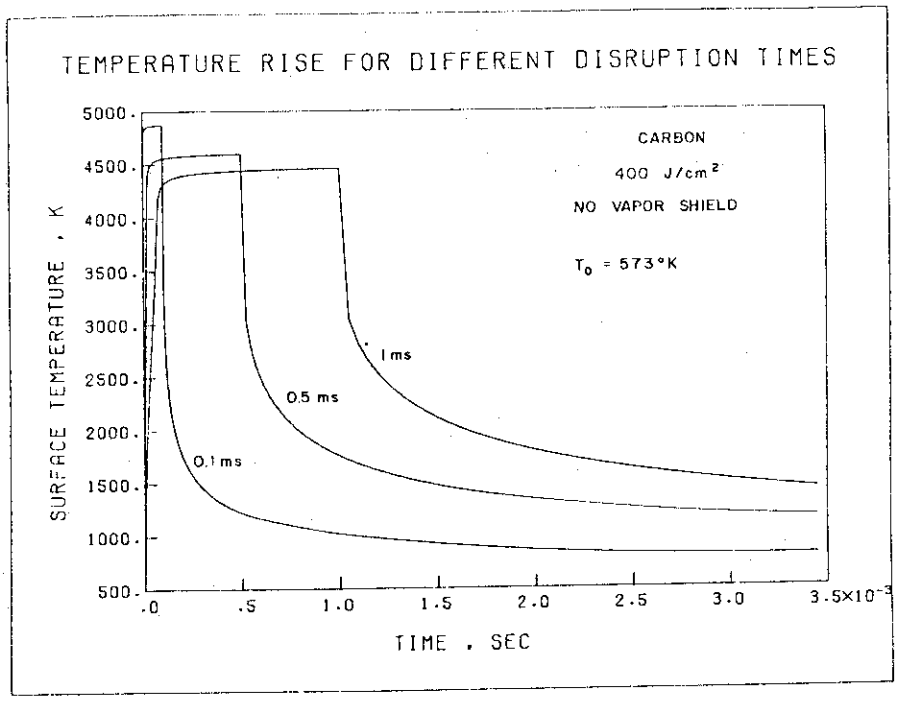

Fig. 4-35

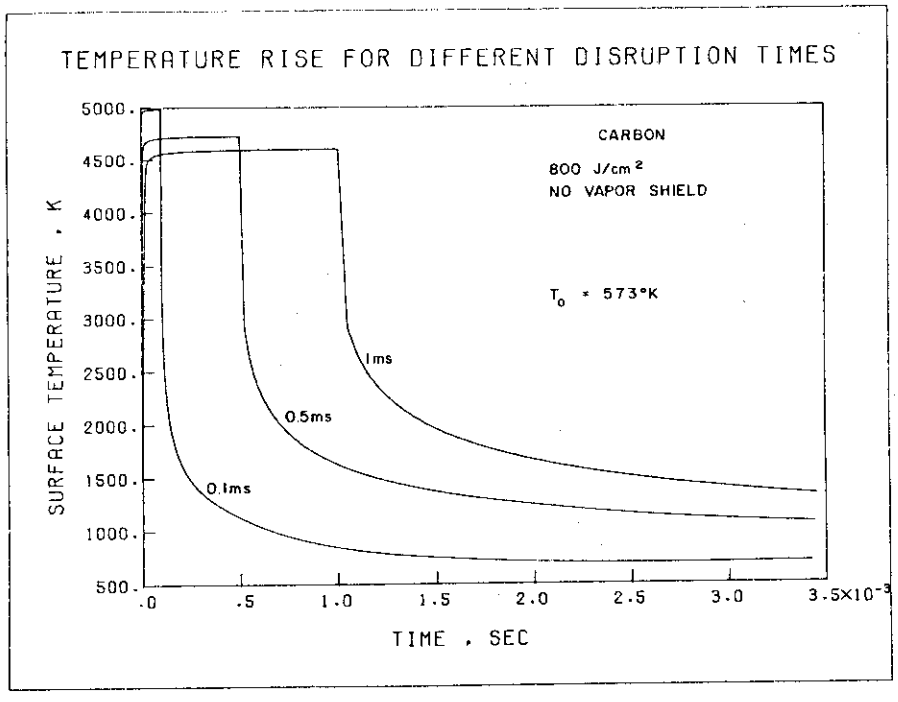

Fig. 4-36

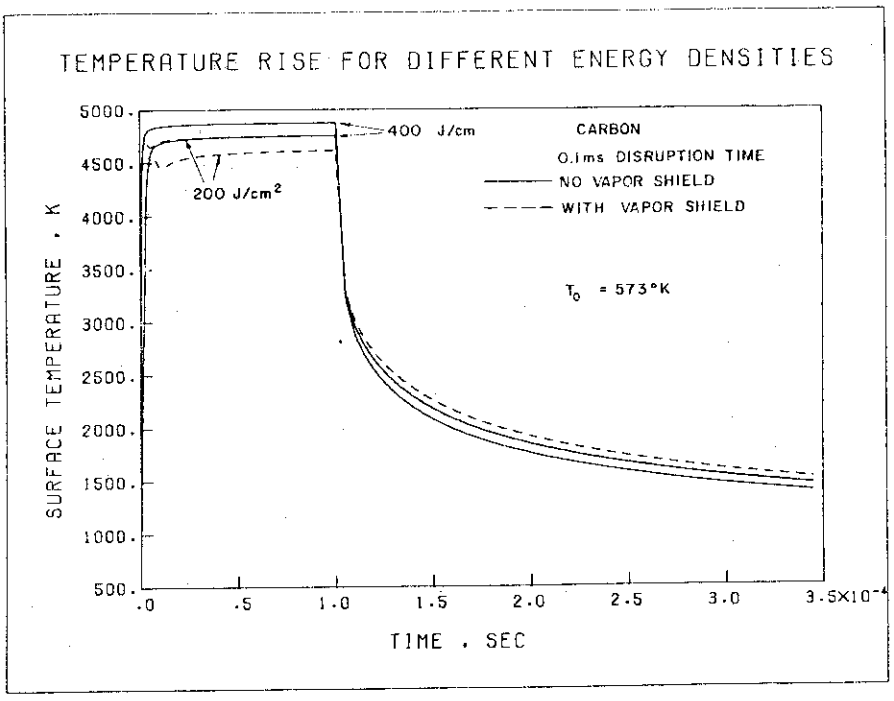

Fig. 4-37

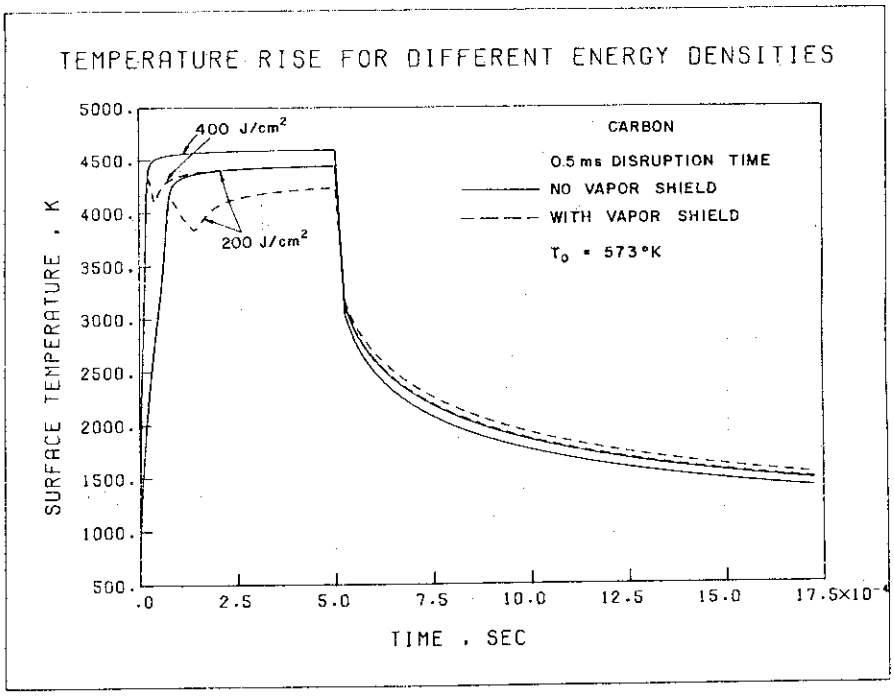

Fig. 4-38

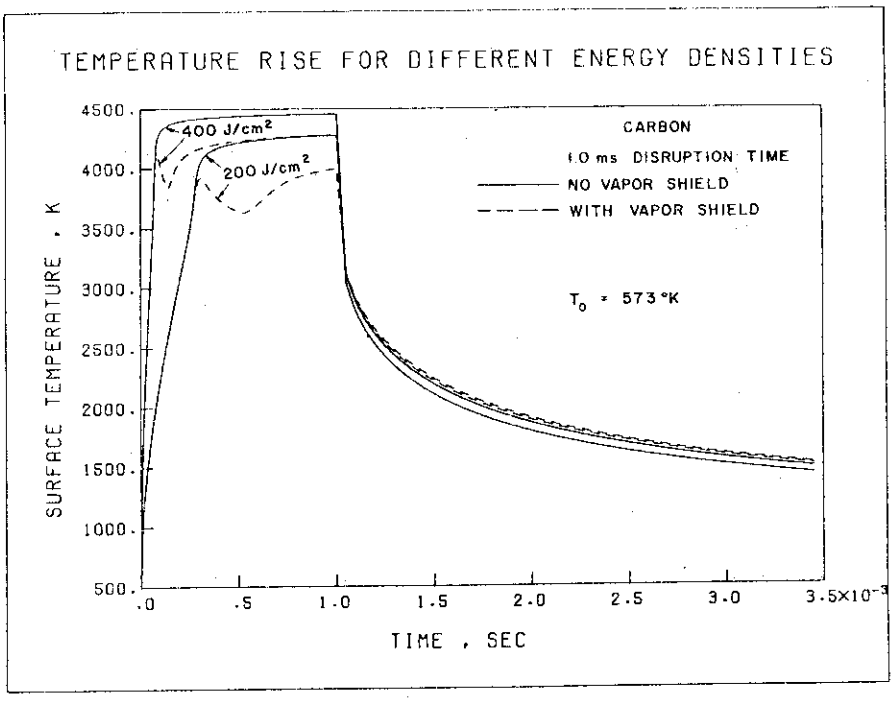

Fig. 4-39

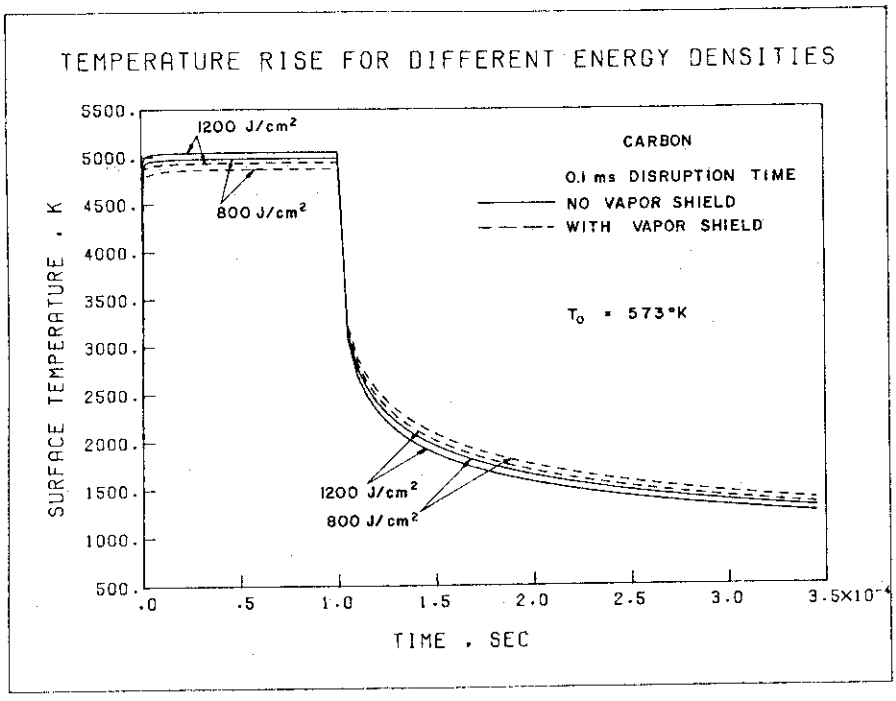

Fig. 4-40

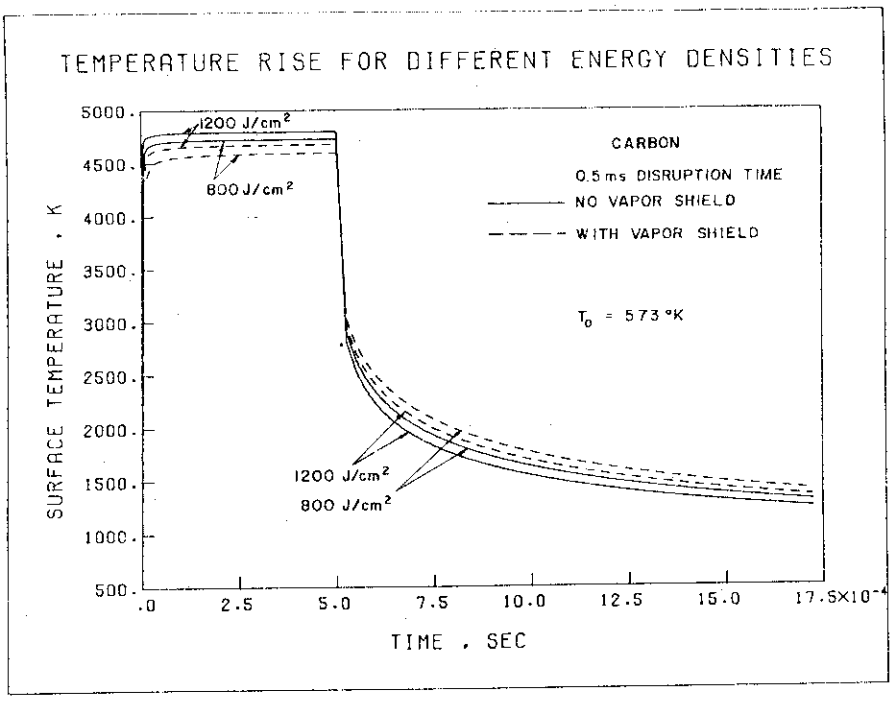

Fig. 4-41

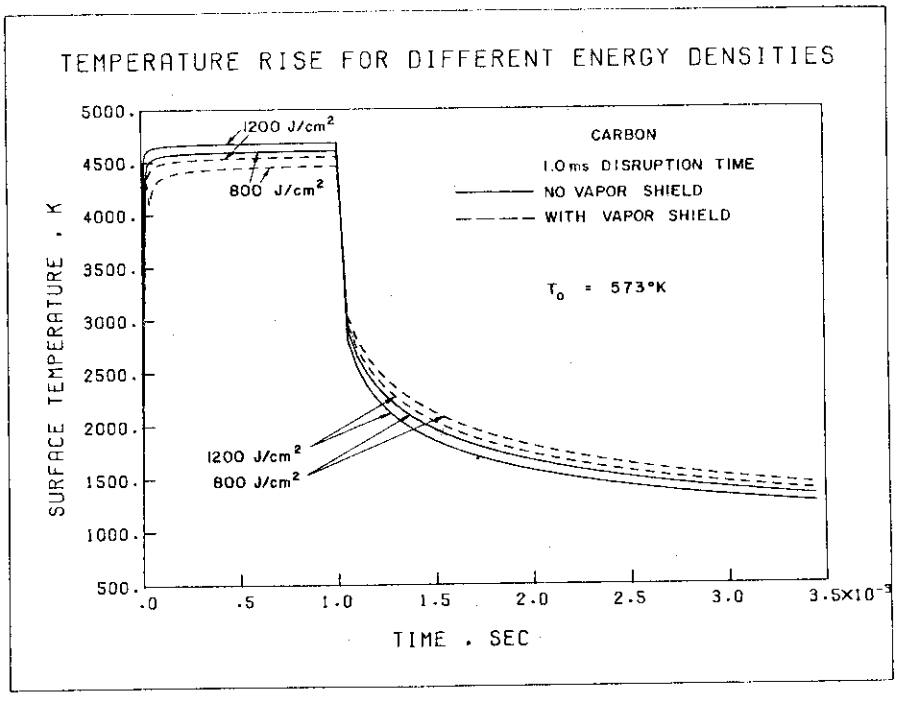

Fig. 4-42

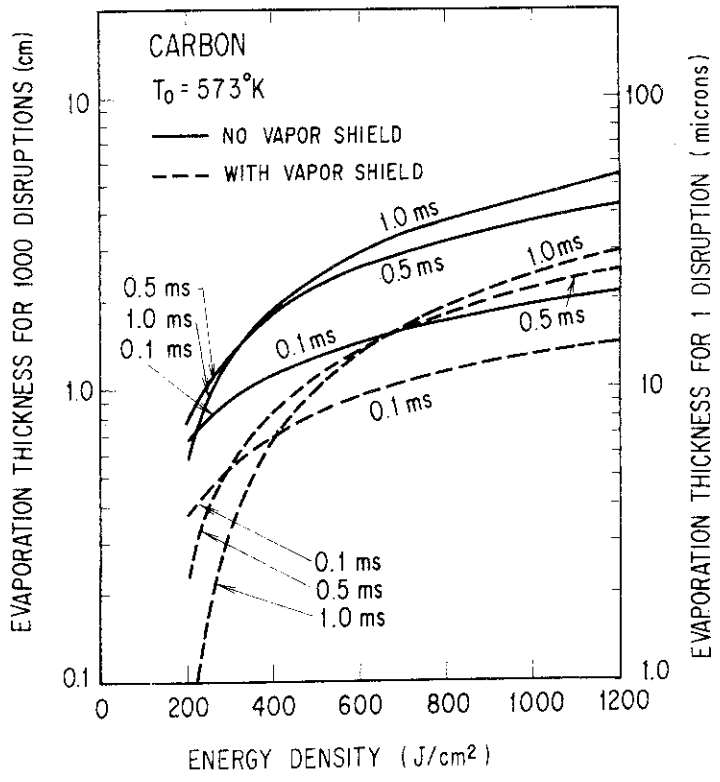

Fig. 4-43 Evaporation thickness of carbon for different energy deposited and disruption time (0.1, 0.5 and 1.0 msec).

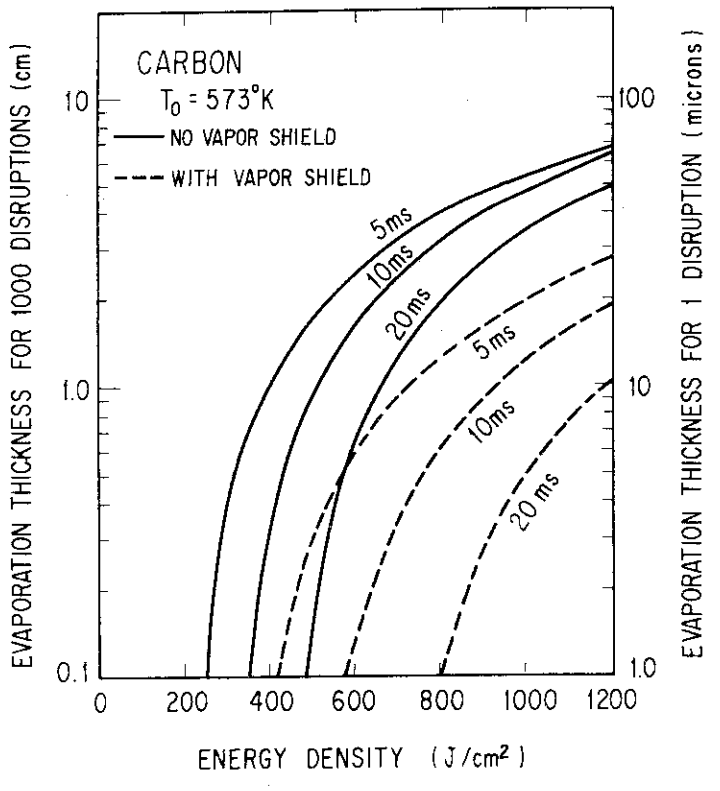

Fig. 4-44 Evaporation thickness of carbon for different energy deposited and disruption time (5, 10 and 20 msec).

Table 4-5(a) Effect of heat flux on the vaporization thickness of TiC (μm)

TiC Evap. Thickness (μm)		0.1 msec		0.5 msec		1.0 msec	
Energy Flux	Initial	Vapor Shield		Vapor Shield		Vapor Shield	
(J/cm^2)	Temp.(°K)	w/o	with	w/o	with	w/o	with
200	573	20	.6	10	0	4	0
400	573	46	20	40	12	33	7
800	573	96	47	95	41	91	35
1200	573	143	72	147	69	145	64

(a) If value is less than 1 microns per pulse, it is set equal to 0.

Table 4-5(b) Effect of heat flux on the melt layer thickness of Tic (μm).

TiC Melt Thickness (μm)		0.1 msec		0.5 msec		1.0 msec	
Energy Flux	Initial	Vapor Shield		Vapor Shield		Vapor Shield	
(J/cm^2)	Temp.(°K)	w/o	with	w/o	with	w/o	with
200	573	14	19	37	33	45	22
400	573	9	14	28	37	48	52
800	573	5	9	21	26	33	46
1200	573	4	7	12	21	23	35

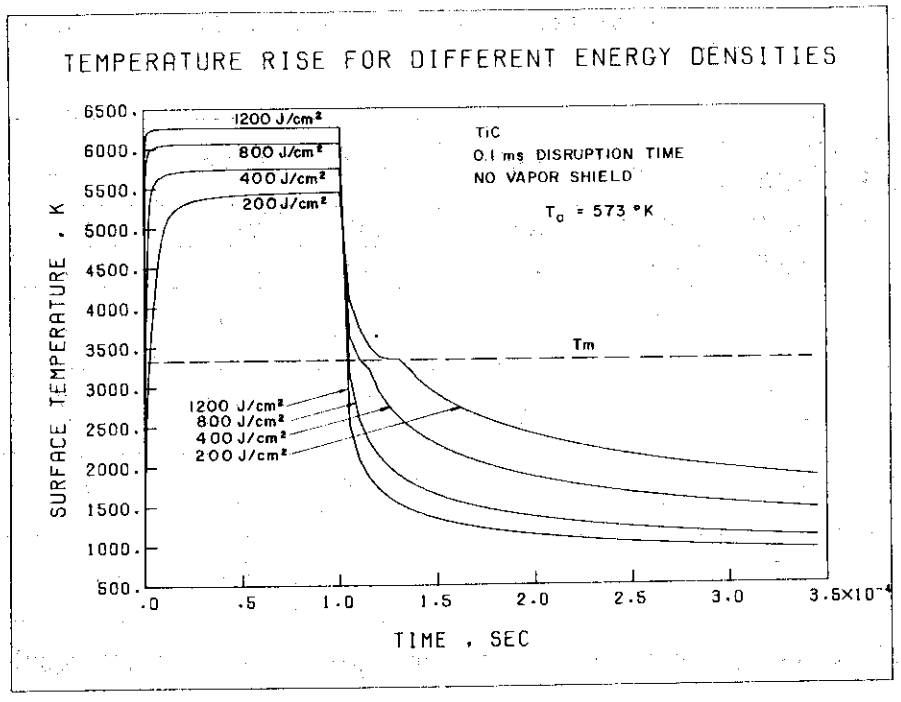

Fig. 4-45

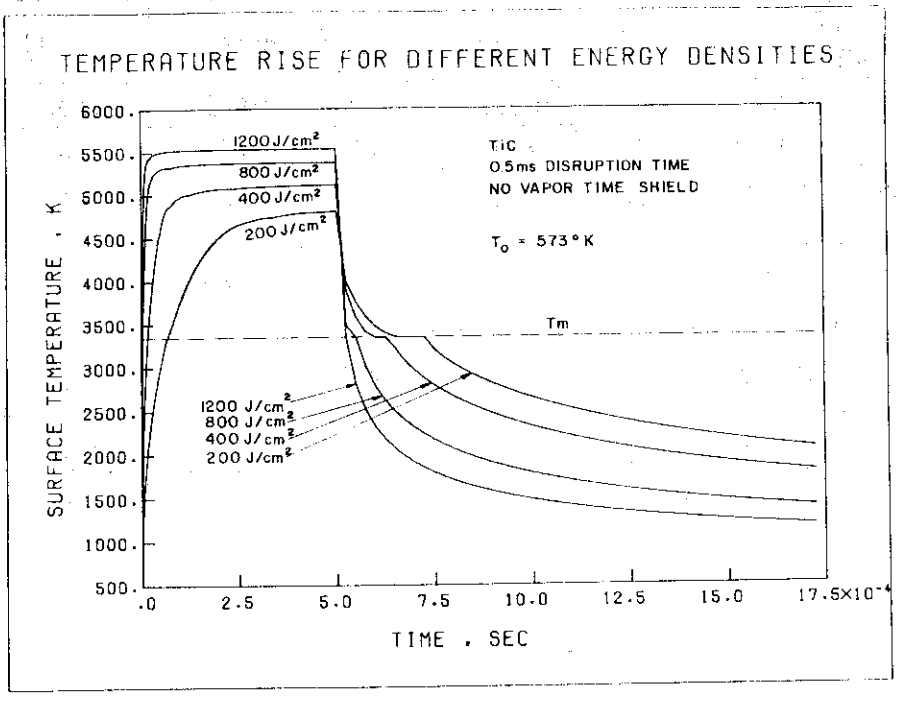

Fig. 4-46

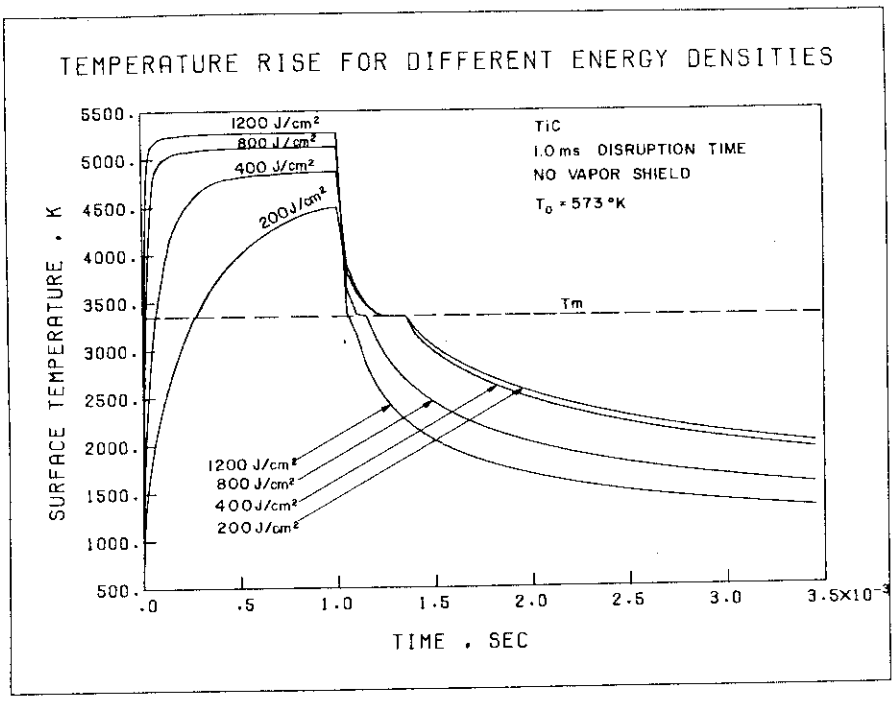

Fig. 4-47

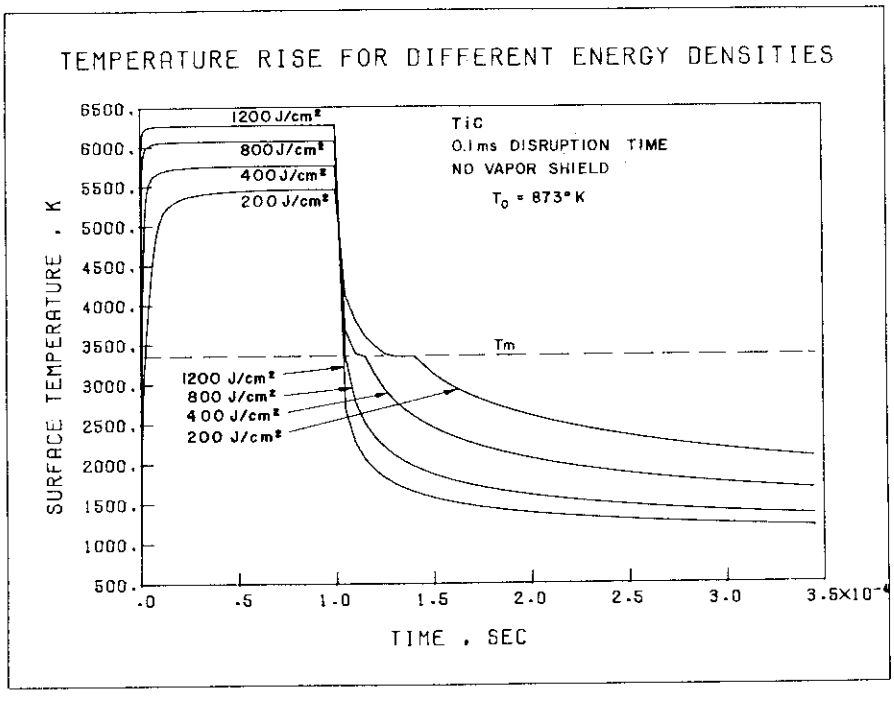

Fig. 4-48

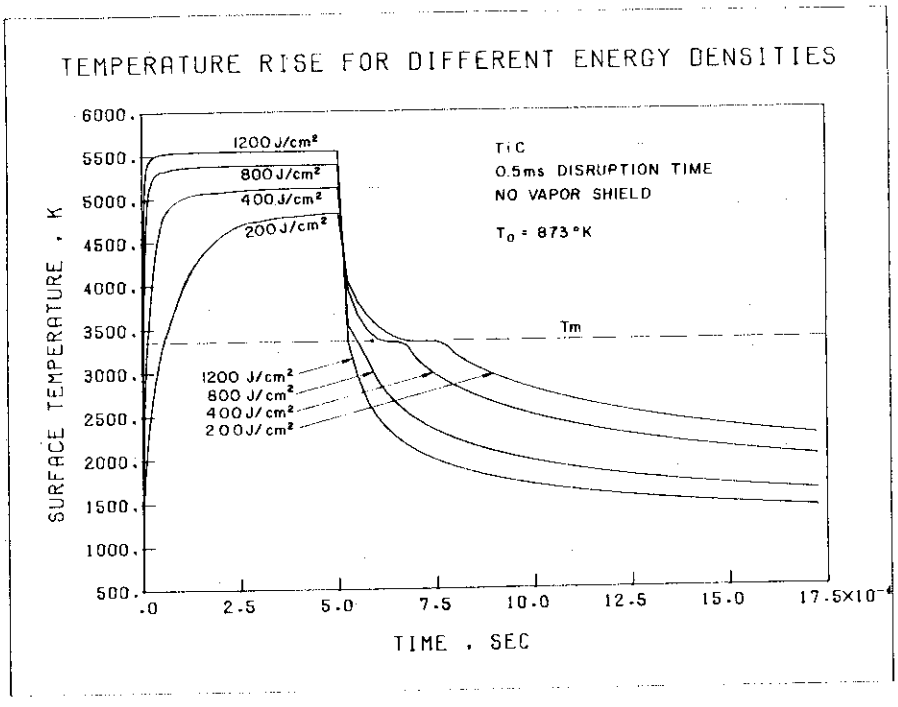

Fig. 4-49

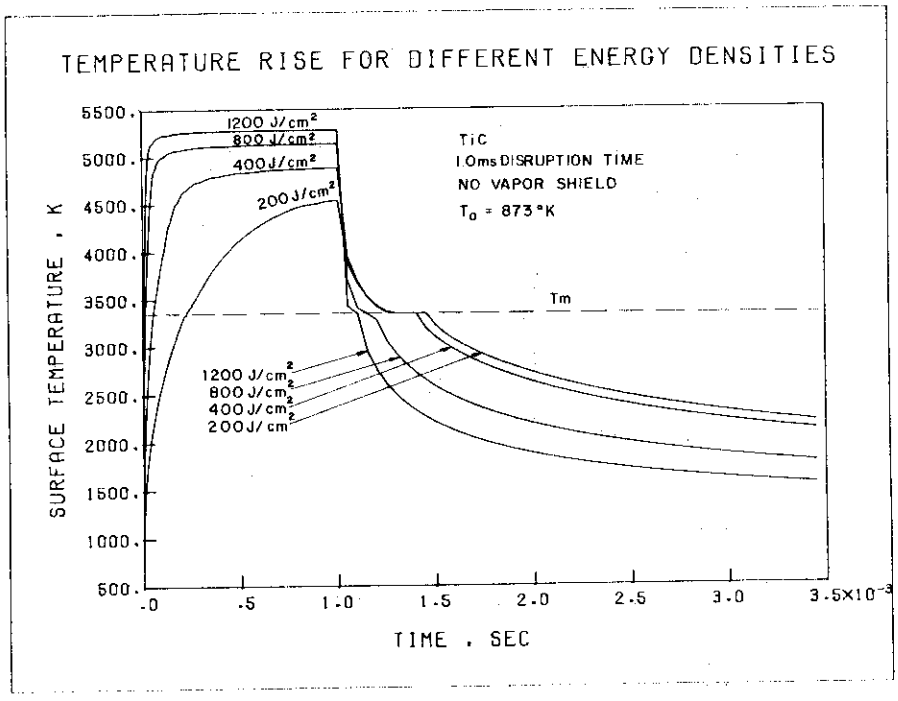

Fig. 4-50

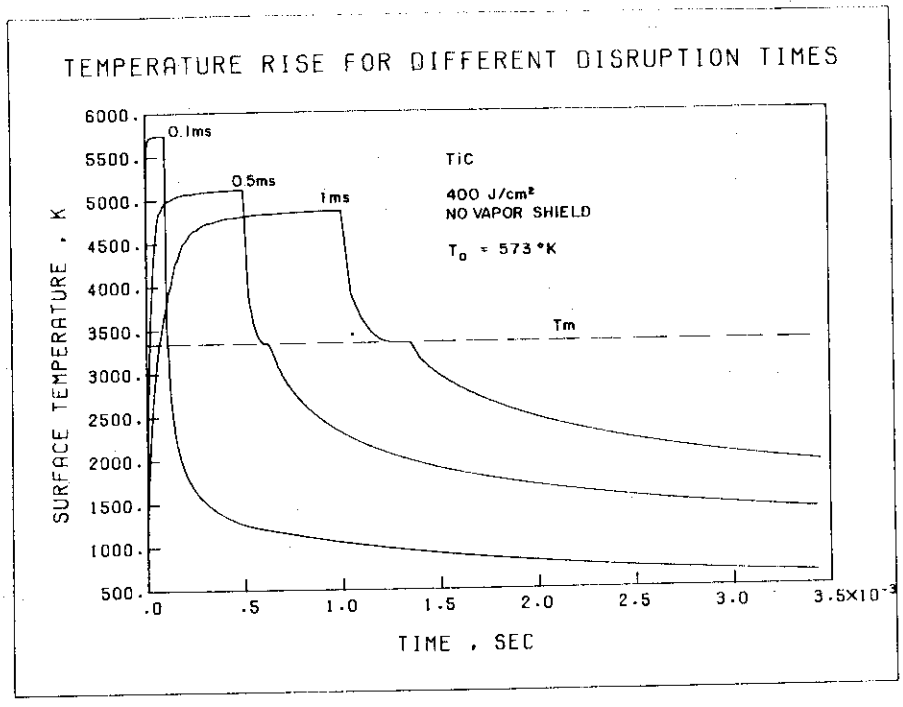

Fig. 4-51

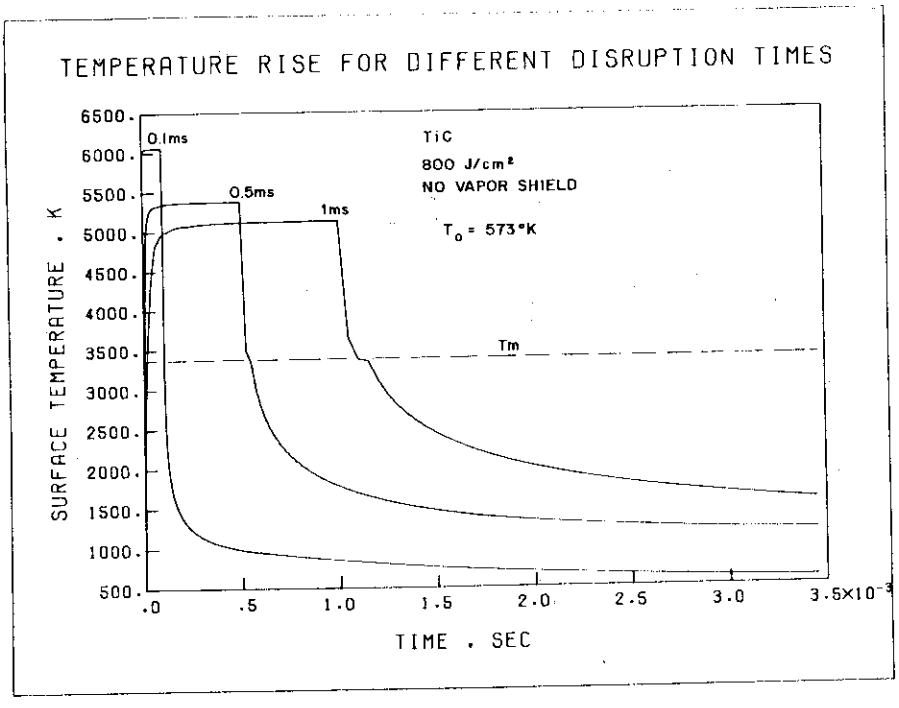

Fig. 4-52

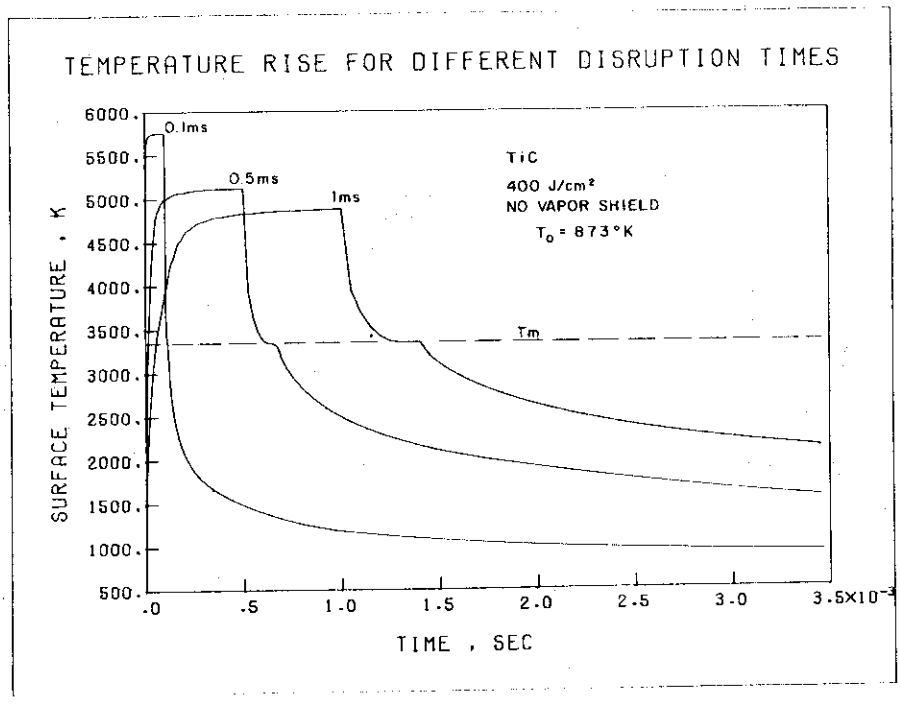

Fig. 4-53

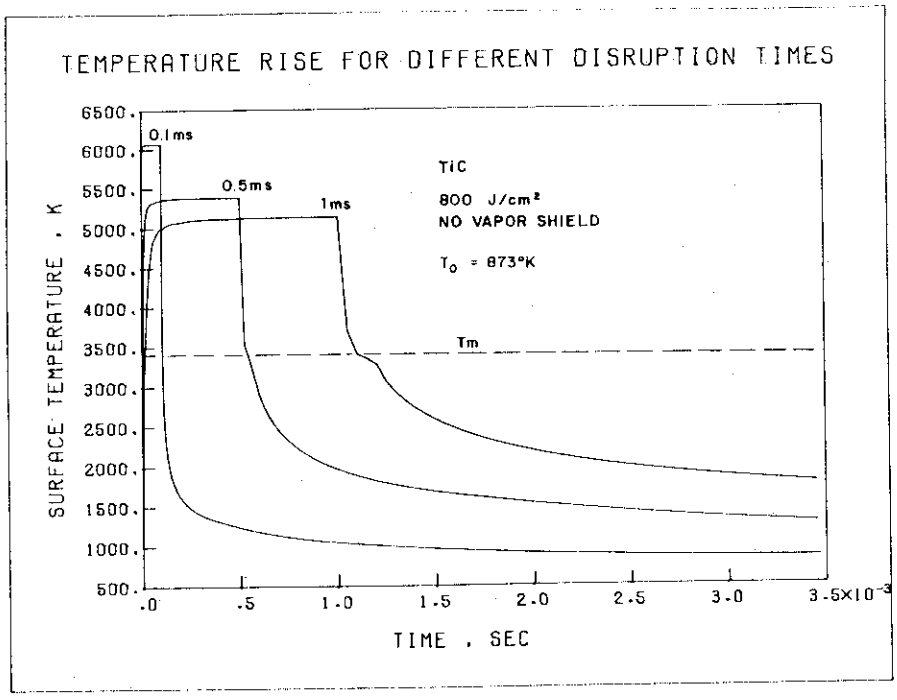

Fig. 4-54

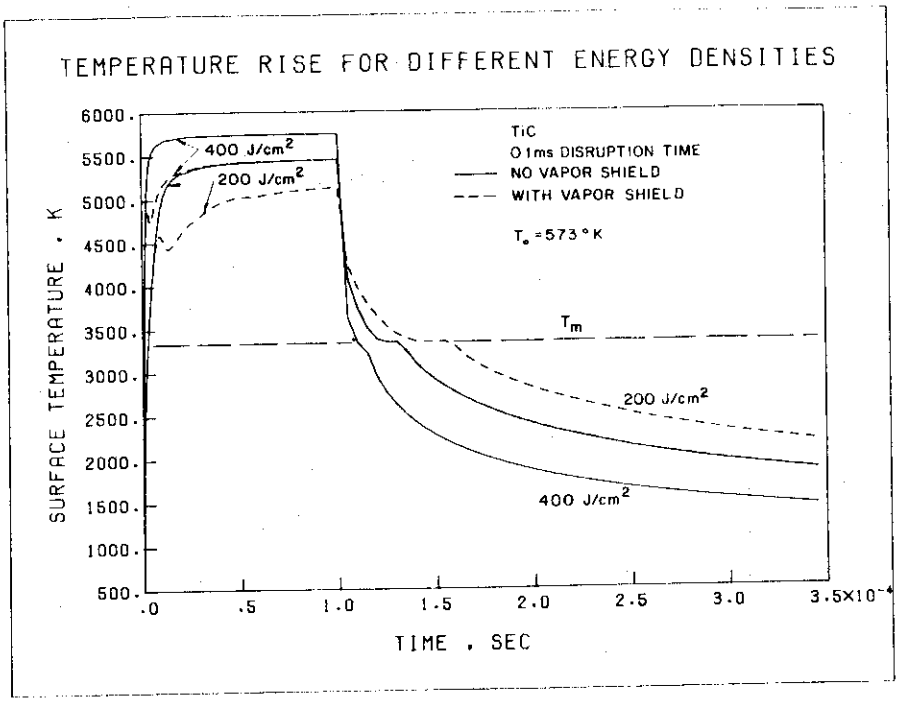

Fig. 4-55

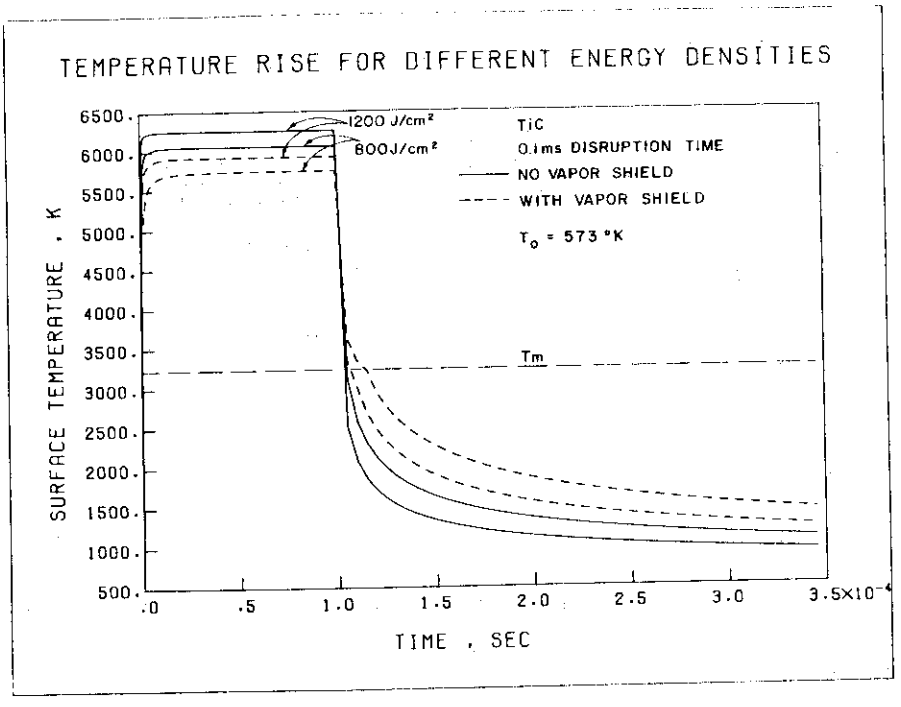

Fig. 4-56

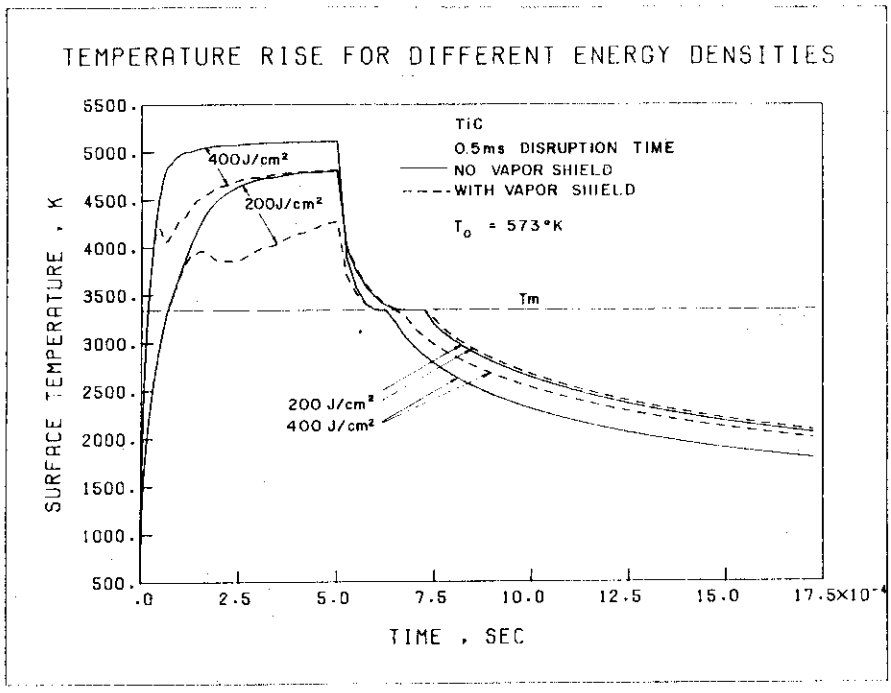

Fig. 4-57

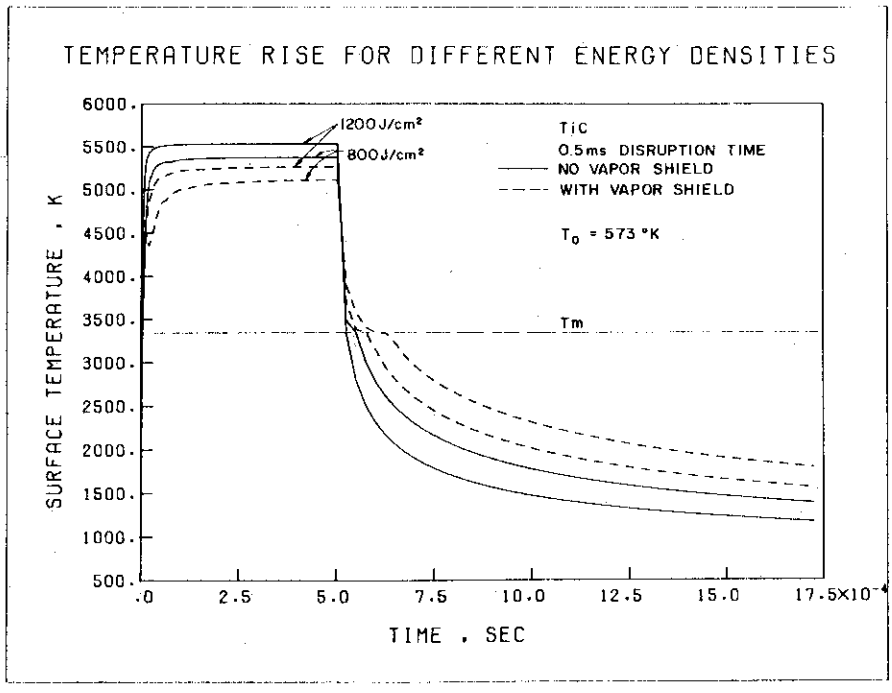

Fig. 4-58

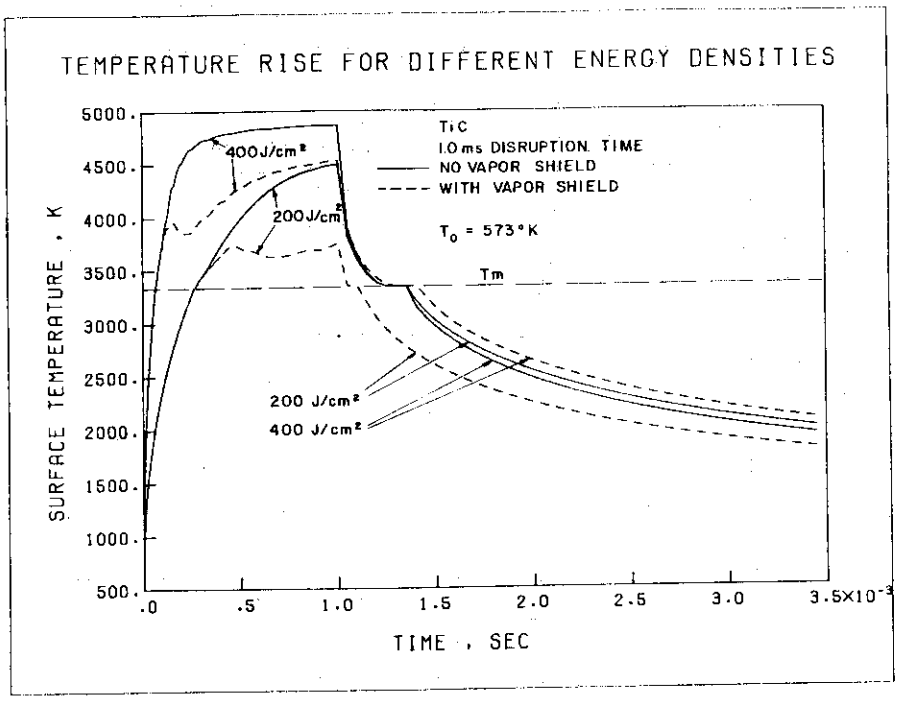

Fig. 4-59

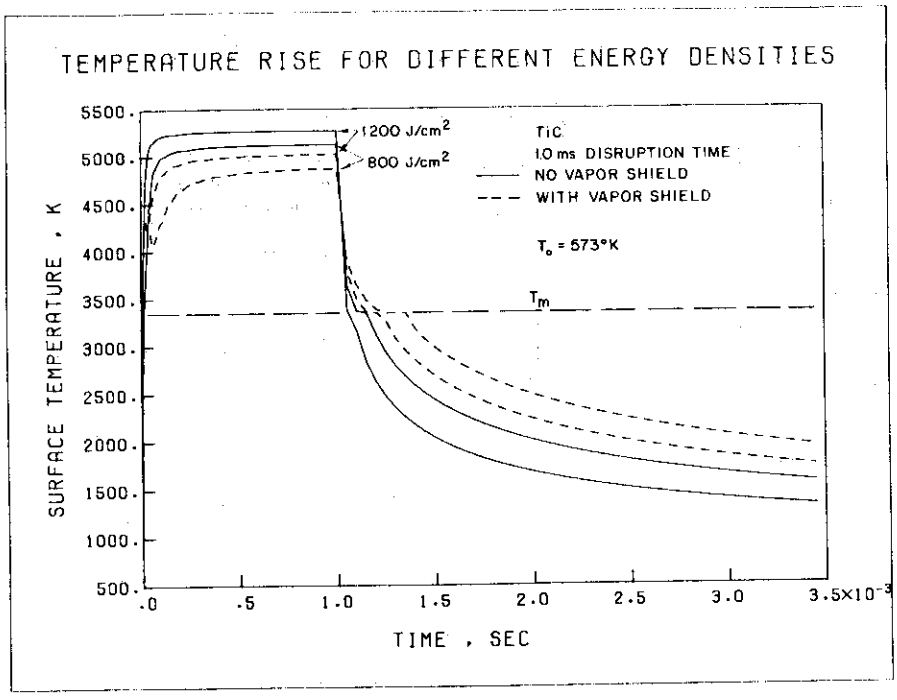

Fig. 4-60

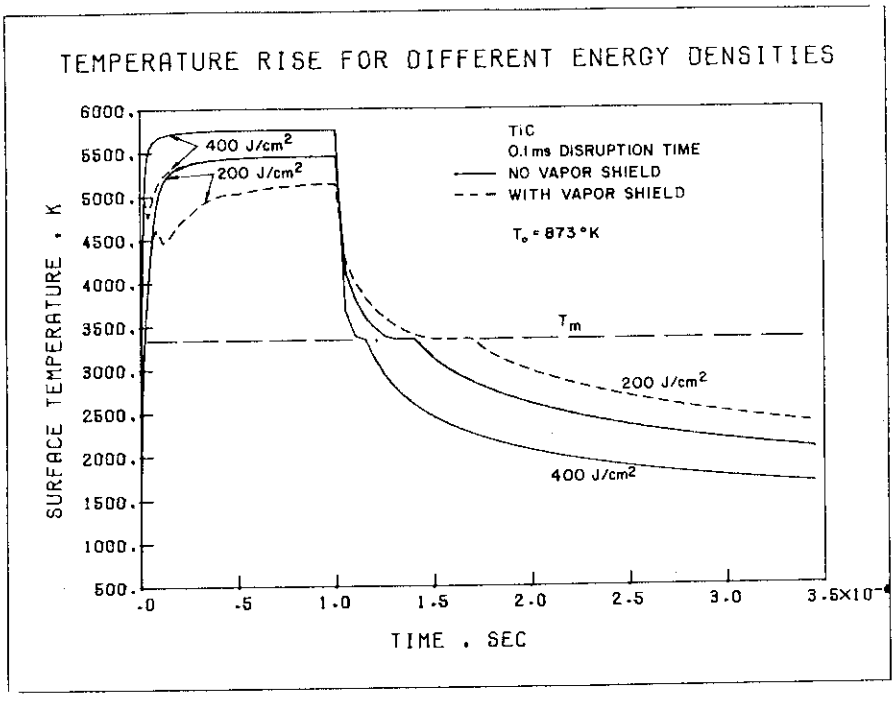

Fig. 4-61

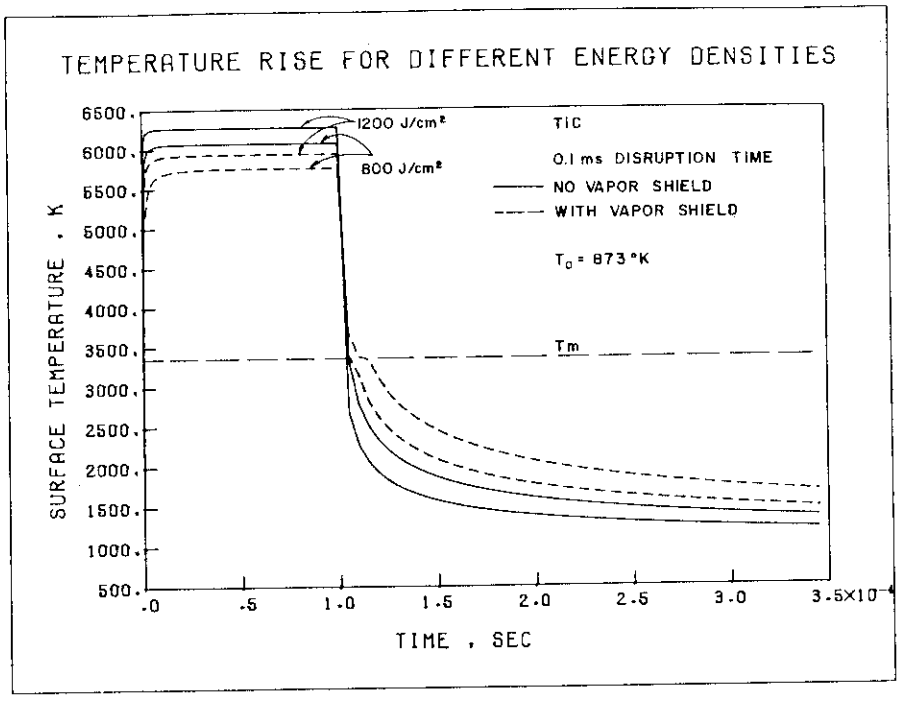

Fig. 4-62

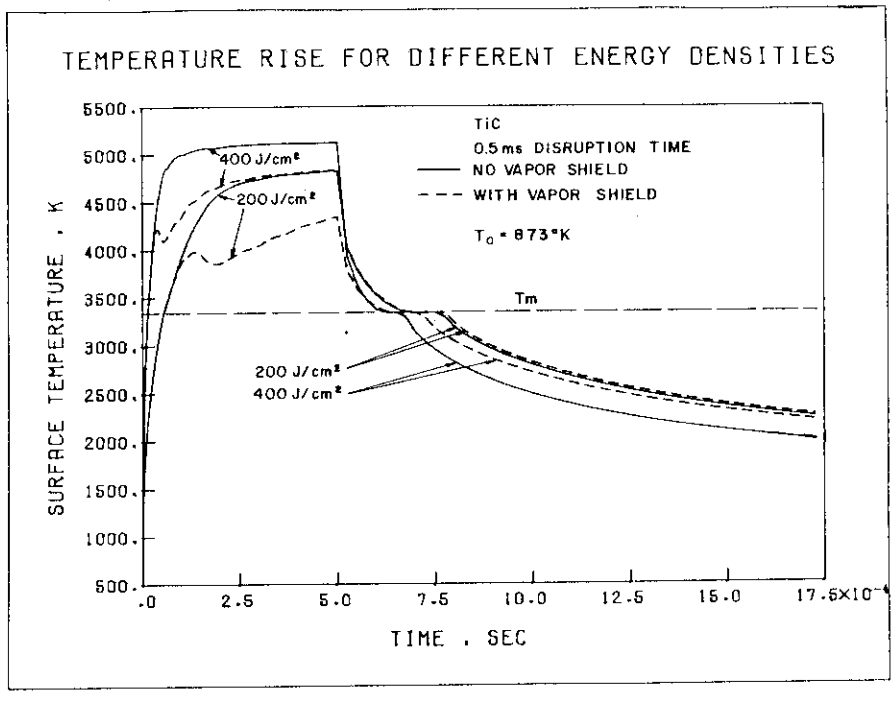

Fig. 4-63

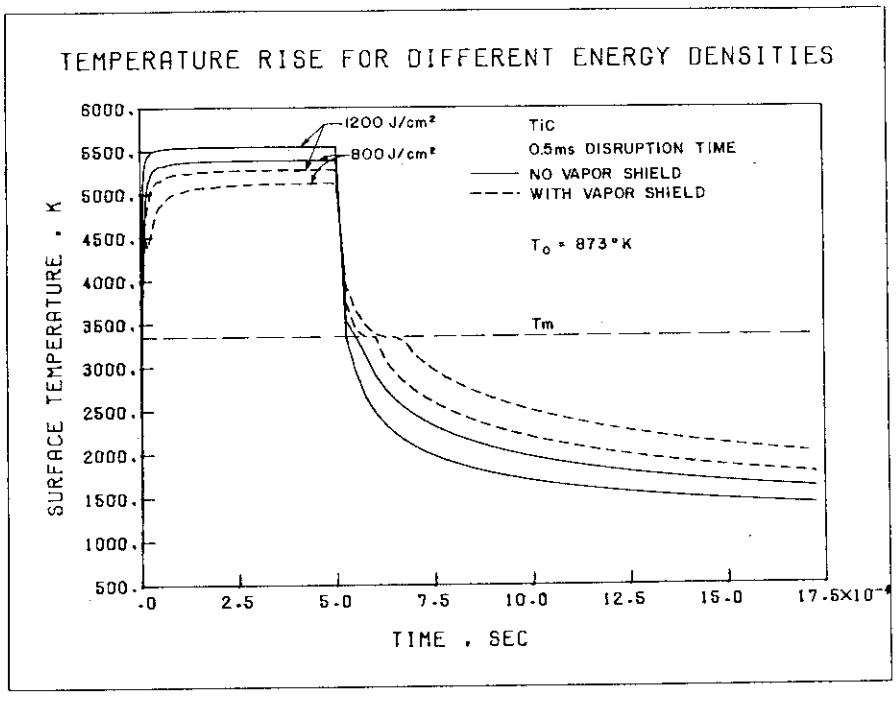

Fig. 4-64

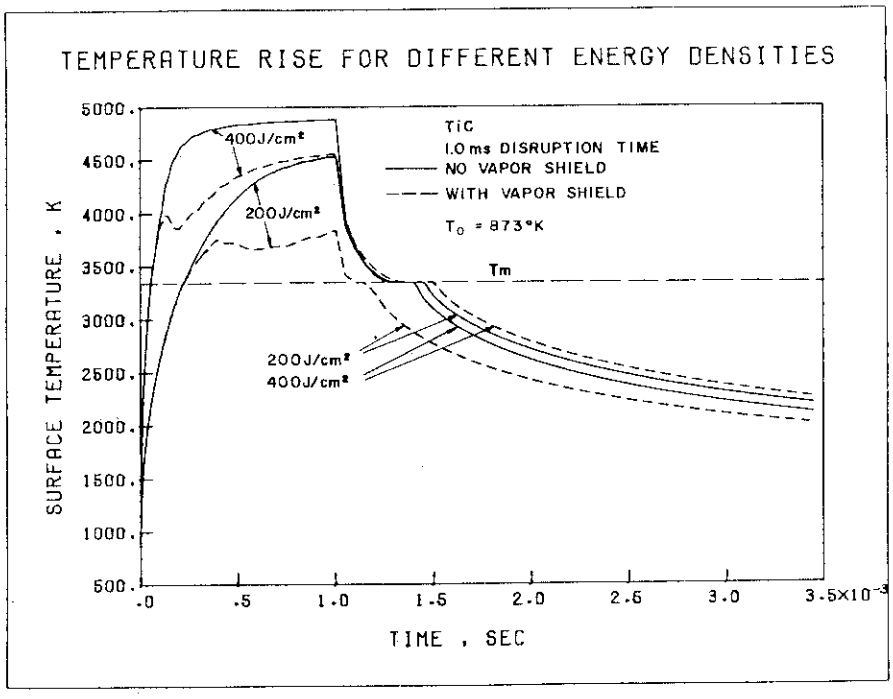

Fig. 4-65

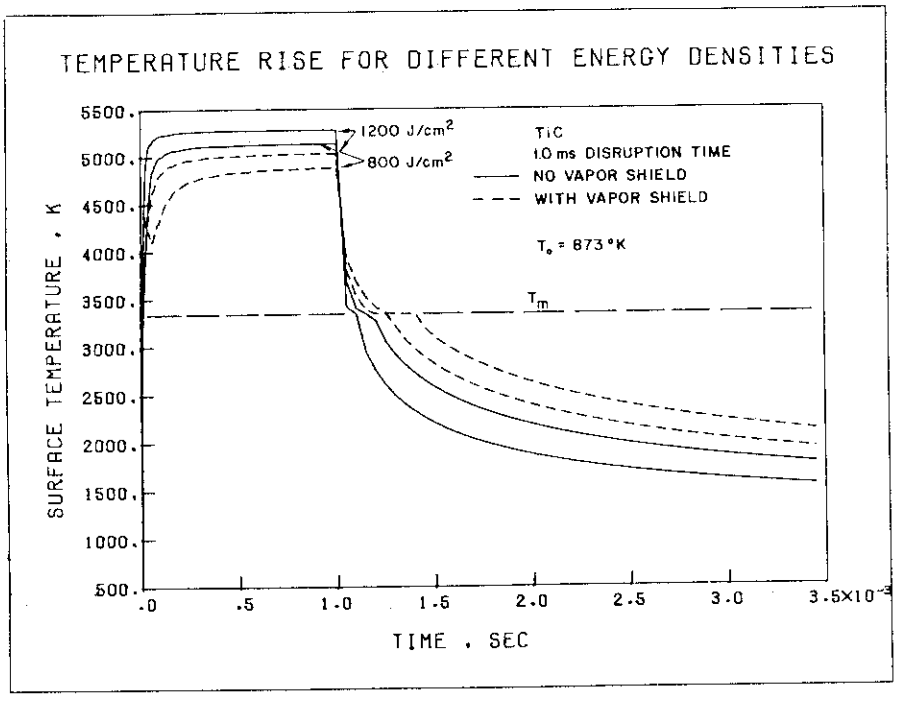

Fig. 4-66

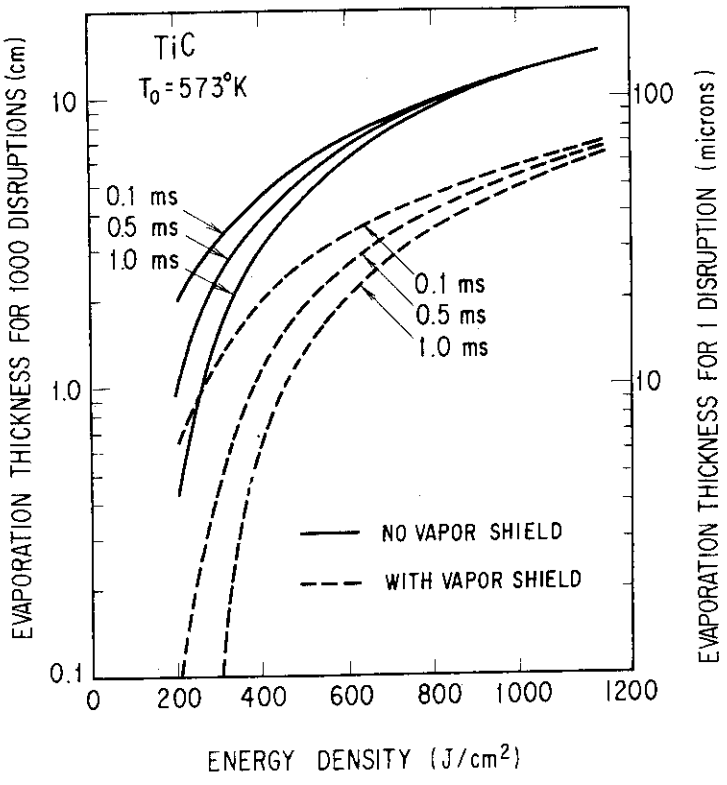

Fig. 4-67 Evaporation thickness of TiC for different energy deposited and disruption time (0.1, 0.5 and 1.0 msec).

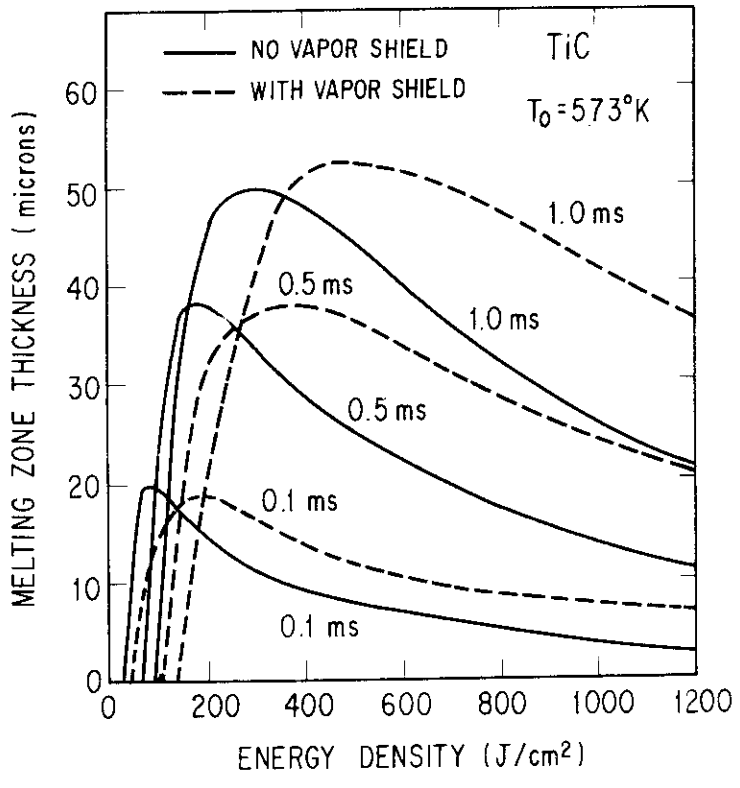

Fig. 4-68 Melt layer thickness of TiC for different energy deposited and disruption time (0.1, 0.5 and 1.0 msec).

Table 4-6(a) Effect of heat flux on the vaporization thickness of SiC (μm). (0.1, 0.5 and 1.0 msec disruption time)

SiC Evap. Thickness (μm)		0.1 msec		0.5 msec		1.0 msec	
Energy Flux	Initial	Vapor Shield		Vapor Shield		Vapor Shield	
(J/cm²)	Temp(°K)	w/o	with	w/o	with	w/o	with
200	573	14.8	4.9	7.7	1.0	3.3	0
400	573	34.9	15.5	30.5	9.5	25.3	5.5
800	573	70.9	35.4	73.1	31.8	70.6	27.3
1200	573	105	53.7	113	53.4	113	50

(a) If value is less than 1 micron per pnlse, it is set equal to 0.

Table 4-6(b) Effect of heat flux on the melt layer thickness of Sic (μm). (5, 10 and 20 msec disruption time)

SiC Evap. Thickness (μm)		5.0 msec		10.0 msec		20.0 msec	
Energy Flux	Initial	Vapor Shield		Vapor Shield		Vapor Shield	
(J/cm²)	Temp(°K)	w/o	with	w/o	with	w/o	with
200	573	0	0	0	0	0	0
400	573	5.4	0	0	0	0	0
800	573	49.9	9.2	32.6	2.5	12.8	0
1200	573	98.2	30.1	81.1	16.6	55.8	4.8

(a) If value is less than 1 micron per pulse, it is set equal to 0.

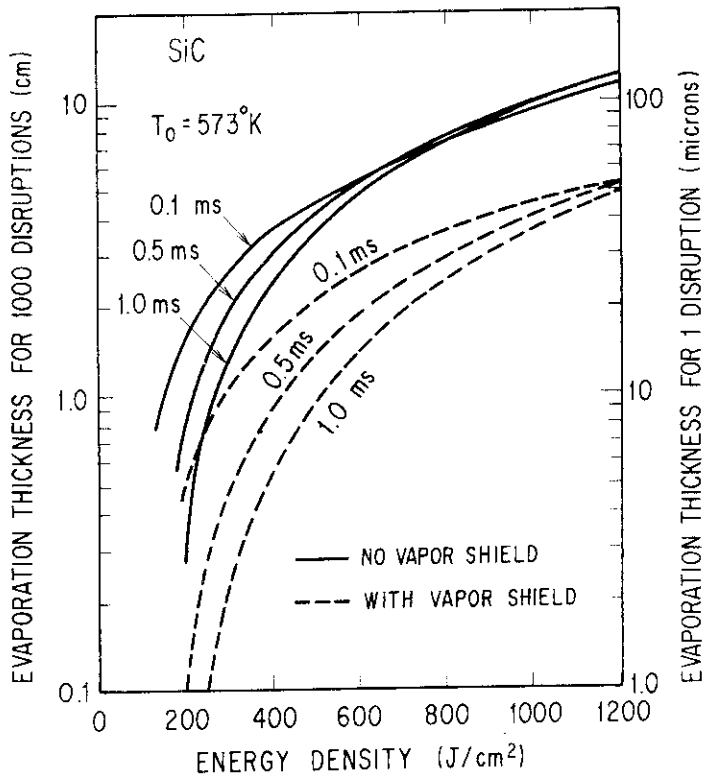

Fig. 4-69 Evaporation thickness of SiC for different energy deposited and disruption time (0.1, 0.5 and 1.0 msec)

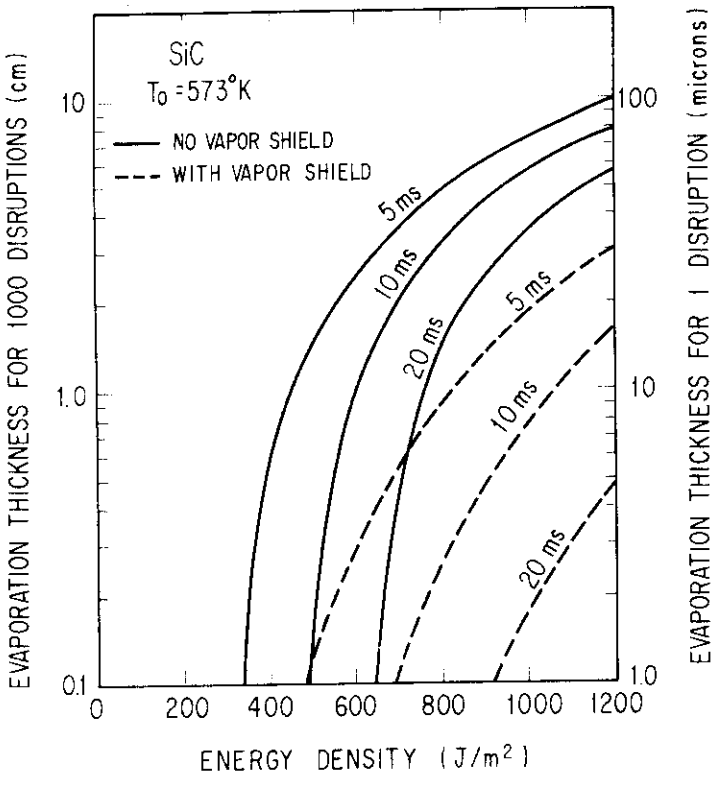

Fig. 4-70 Evaporation thickness of SiC for different energy deposited and disruption time (5, 10 and 20 msec)

Table 4-7 Evaporation, melting and total erosion thicknesses of C, SiC, TiC and Mo for 200 J/cm^2 and 0.1 ∿ 1.0 msec.

200 J/cm^2		C			SiC			TiC			Mo		
		EVAP	MELT	TOTAL	EVAP	MELT	TOTAL	EVAP	MELT	TOTAL	EVAP	MELT	TOTAL
0.1 (ms)	w/o v.s.	7	NM	7	15	NM	15	20	14	34	12	34	46
	with v.s.	4	NM	4	5	NM	5	6	19	25	2	37	39
0.5 (ms)	w/o v.s.	8	NM	8	8	NM	8	10	37	47	2	65	67
	with v.s.	2	NM	2	1	NM	1	0	33	33	0	44	44
1.0 (ms)	w/o v.s.	6	NM	6	3	NM	3	4	45	49	0	57	57
	with v.s.	1	NM	1	0	NM	0	0	22	22	0	49	49

a) If value is less than 1 micron per pulse, it is set equal to 0.
b) $T_0 = 573°K$
c) w/o v.s. means without vapor shielding.
d) NM means no melting.

Table 4-8 Evaporation, melting and total erosion thicknesses of C, SiC, TiC and Mo for 200 J/cm^2 and 5 ∿ 20 msec.

200 J/cm^2		C			SiC			316SS			Mo		
		EVAP	MELT	TOTAL	EVAP	MELT	TOTAL	EVAP	MELT	TOTAL	EVAP	MELT	TOTAL
5.0 (ms)	w/o v.s.	0	NM	0	0	NM	0	4	100	104	0	0	0
	with v.s.	0	NM	0	0	NM	0	0	80	80	0	0	0
10.0 (ms)	w/o v.s.	0	NM	0	0	NM	0	0	100	100	0	0	0
	with v.s.	0	NM	0	0	NM	0	0	75	75	0	0	0
20.0 (ms)	w/o v.s.	0	NM	0	0	NM	0	0	50	50	0	0	0
	with v.s.	0	NM	0	0	NM	0	0	45	45	0	0	0

a) If value is less than 1 micron per pulse, it is set equal to 0.
b) $T_0 = 573°K$
c) w/o v.s. means without vapor shielding.
d) NM means no melting.

Table 4-9 Evaporation, melting and total erosion thicknesses of C, SiC, 316SS and Mo for 400 J/cm^2 and 5 ∿ 20 msec.

400 J/cm^2		C			SiC			316SS			Mo		
		EVAP	MELT	TOTAL	EVAP	MELT	TOTAL	EVAP	MELT	TOTAL	EVAP	MELT	TOTAL
5 (ms)	w/o v.s.	10	NM	10	5	NM	5	30	120	150	0	95	95
	with v.s.	1	NM	1	0	NM	0	5	110	115	0	88	88
10 (ms)	w/o v.s.	3	NM	3	0	NM	0	20	160	180	0	3	3
	with v.s.	0	NM	0	0	NM	0	15	125	127	0	3	3
20 (ms)	w/o v.s.	0	NM	0	0	NM	0	9	220	229	0	0	0
	with v.s.	0	NM	0	0	NM	0	0	170	170	0	0	0

a) If value is less than 1 micron per pulse, it is set equal to 0.

b) $T_0 = 573°K$

c) w/o v.s. means without vapor shielding.

d) NM means no melting.

5. Modification of the vapor shielding model

5.1 Introduction

The development of the A*Thermal code[18] has greatly assisted our ability to analyze evaporation and melting of limiter or first wall surfaces during a plasma disruption. However, there are some assumptions in the evaporation code which need to be tested parametrically to determine the overall erosion sensitivity.

Two such assumptions are 1) the conversion of the kinetic energy of the incoming plasma ions to X-rays in the blow-off layer, and 2) the fraction of the blow-off layer which stays in front of the first wall during the disruption. The objective of this study is to show the sensitivity of the present model to the above conditions.

5.2 Background to modifications of the present vapor shielding model

It has been assumed in A*Thermal that if a vapor layer of sufficient thickness has been produced, the plasma ions will be stopped in this vapor layer rather than in the condensed material of the wall. In this model, it is also assumed that all the energy deposited by the ions in the vapor will be converted to radiation energy and isotropically reradiated back to the wall. It is furthermore assumed that all the vaporized material will stay in front of the wall and be intersected by the incoming plasma ions.

However, if all of the energy deposited by the ions in the vapor is not converted into radiation energy, then this could affect the total amount of melted and vaporized material. In this analysis, an energy conversion coefficient, α, is introduced to account for the conversion of ion energy into radiation energy. An example of a case where the kinetic energy might not be converted into radiation is when the incoming ions cause the vapor to be highly ionized and recombination occurs much later. In this case, the energy incident on the wall during the disruptive period is reduced.

Another factor to be considered is the transfer of some, or all, of the vaporized material away from the incident plasma ions during the disruption process. If all the vapor moves away from the disruption area immediately as it forms (e.g., under the action of a magnetic field), then there will be no vapor shielding to the wall.

In this analysis a vapor transfer coefficient, β, which allows for some or all the vapor to be moved away is introduced.

The new formulation of the model is presented as follows. For a vapor layer produced by the evaporation of a thickness, $\Delta x(t)$, the actual thickness, $\Delta x_a(t)$, of the layer seen by the incoming plasma ions is written as:

$$\Delta x_a(t) = (1-\beta)\Delta x(t) \tag{5-1}$$

where β = vapor transfer coefficient

and $0 \leqslant \beta \leqslant 1$.

Here

$\beta = 0$ means that there is a full vapor shield.

$\beta = 1$ means that there is no vapor shield.

This vapor layer will reduce the heat flux to the first wall to values given by the following considerations:

1. For $\Delta x_a(t) \leqslant R$ [or $\Delta x(t) \leqslant \frac{R}{(1-\beta)}$]

Let R be the range of the plasma ions into the wall material. Then,

$$F(t) = F_0 \left[1 - \frac{\Delta x_a(t)}{R}\right] + \frac{1}{2} F_0 \frac{\Delta x_a(t)}{R} (2-\alpha)$$

$$= F_0 \left[1 - \frac{\Delta x_a(t)}{R} \cdot \frac{\alpha}{2}\right] \quad . \tag{5-2}$$

In terms of the total material vaporized, $\Delta x(t)$, the surface heat flux is given by:

$$F(t) = F_0 \left[1 - \frac{(1-\beta)\alpha}{2} \cdot \frac{\Delta x(t)}{R}\right] \tag{5-3}$$

where F_0 = original heat flux to the wall

α = energy conversion coefficient

and

$1 \leqslant \alpha \leqslant 2$.

Here

$\alpha = 1$ means that all the energy of the ions is converted to radiation energy of the vapor to the wall.

$\alpha = 2$ means that none of the energy of the ions is converted to radiation energy to the wall.

2. For $\Delta x_a(t) > R$ [or $\Delta x(t) > \frac{R}{(1-\beta)}$]

For this case, the energy flux is

$$F(t) = F_0 \left(1 - \frac{\alpha}{2}\right) \quad . \tag{5-4}$$

We will demonstrate the implications of the model by considering a disruption case where 400 J/cm^2 is deposited in 0.5 msec on a Mo first wall initially at temperature $T_0 = 573°K$. Fig.5-1 shows the surface temperature of Mo as a function of time for $\beta = 0.0$ (which means that if there is any vaporized material, it will not move away from the disruption area) and for different values of α. The case for $\alpha = 1.0$ means that all the energy of the ions is converted to radiation by the vapor. For $\alpha = 1.5$ it means that 50% of the energy of the ions is converted to radiation energy while the case $\alpha = 2.0$ indicates that none of the ion energy absorbed in the blow-off layer is converted to radiation energy to the wall. As can be seen from Fig.5-1, a substantial reduction in the surface temperature occurs for values of α higher than 1.0. This greatly reduces the total amount of material vaporized from the first wall as shown in Table 5-1. A reduction of 50% in the conversion of ion energy to radiation energy, reduces the total amount of vaporized material by about 98%.

Fig.5-2 shows the Mo surface temperature for the same disruption conditions but for $\alpha = 1.0$ and for different values of β. The case for $\beta = 1.0$ means that the vaporized material will move away from the disruption area where it formed, i.e., no vapor shielding is provided. The case where $\beta = 0.0$ means that all the vaporized material will stay in front of the disruption area and will intersect the plasma ions and shield the wall. A value of $\beta = 0.5$ means that only 50% of the vaporized material will stay in front of the incoming ions and the other 50% will move away. It can be seen from Fig.5-2 and Table 5-1 that vapor removal up to 50% has little effect on the vapor shielding. For the particular case shown the evaporation increased only by 6% when half of the vapor was removed as compared to the case when none was removed ($\beta = 0$). This can be explained by the fact that for the case considered, the total amount of material evaporated exceeds the ion range by a substantial fraction. Therefore, even after removing 50% of the vapor, the remaining part is still sufficient to stop the incoming plasma ions. As a result, vapor removal is only important when the evaporated

amount is about equal or less than the ion range. This is to be expected for lower disruption energies, larger disruption times, or both.

5.3 Conclusions

We have shown that if there is a process by which the kinetic energy of the incoming plasma ions is absorbed but not reradiated by the blow-off vapor, a significant reduction in evaporation can occur. The effect on the total melt layer thickness is noticeable, but not as great.

The effect of sweeping away some of the blow-off layer during the disruption is only significant if the remaining vapor represents an amount of material less than the range of plasma ions in the vapor. Transport of vaporized material needs to be studied in more detail, especially in the high magnetic fields of fusion devices.

Table 5-1 Melted and vaporized thickness of Mo first wall during a plasma disruption of 400 J/cm² in 0.5 sec (To = 573°K)

Energy Conversion Coefficient α	Vapor Transfer Coefficient β	Evaporation Thickness ΔX_v (μm)	Melting Thickness ΔX_m (μm)
1.0	1.0	23	69
1.0	0.0	4	75
1.0	0.5	4	74
1.5	0.0	0.075	40
2.0	0.0	0.038	26

a) Energy flux 400 J/cm², Disruption time 0.5 msec

b) Initial temperature To = 573°K.

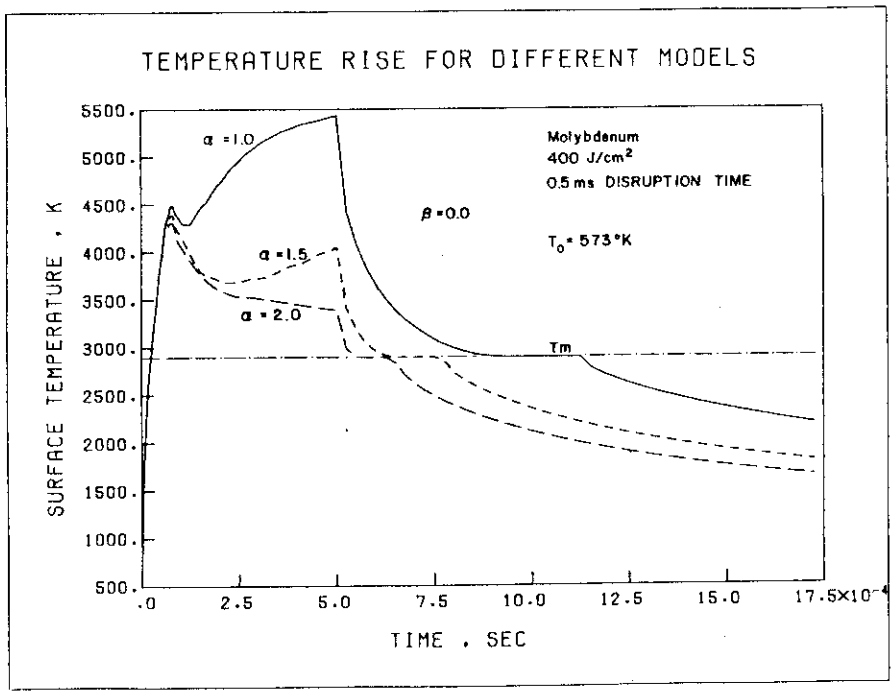

Fig. 5-1 Temperature rise for different models.
(Energy conversion coefficient α = 1.0, 1.5, 2.0
Vapor transfer coefficient β = 0.0)

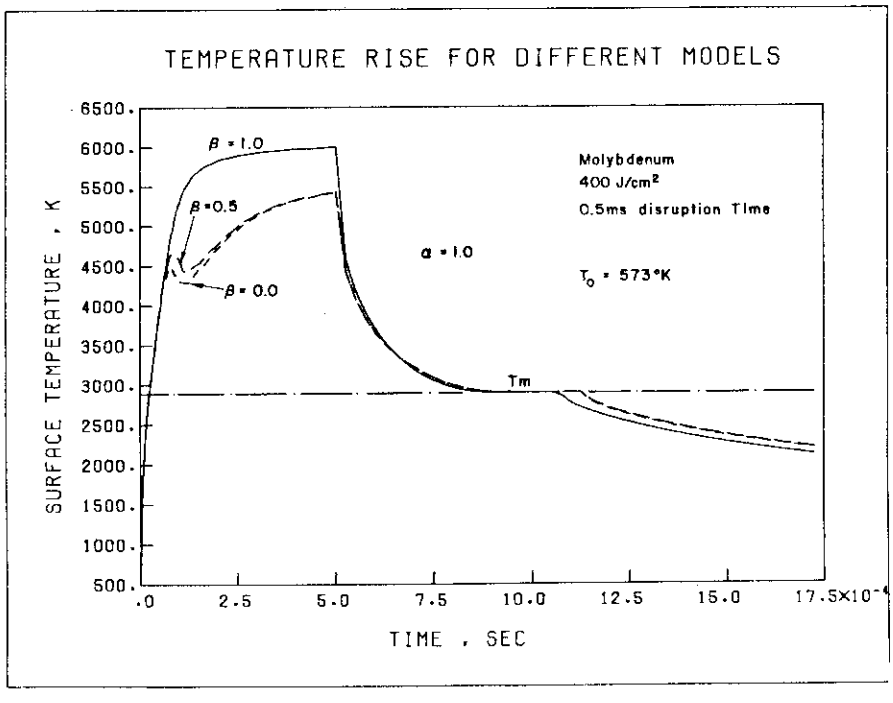

Fig. 5-2 Temperature rise for different models.
(Energy conversion coefficient α = 1.0
Vapor transfer coefficient β = 0.0, 0.5, 1.0)

6. Conclusions

The conclusions drawn from this study are as follows:

1. The effect of vapor shielding on melting and evaporated material depend on the energy density. At the lower energy densities, near melting threshold, vapor shielding is effective for reducing both melting and evaporated material. At higher energy densities, the evaporation thickness decreases and, of the same time, the melting thickness increases.
2. The total erosion thickness depends on the melt layer stability. If the melt layer is stable, the erosion thickness of Mo is less than that of C, SiC, TiC and 316SS. 316SS exhibits the largest erosion. On the other hand, if the melt layer is unstable, the erosion thicknesses of 316SS, TiC and Mo are larger than that of C and SiC.
3. During a plasma disruption, the surface temperature easily reaches values of 3000 ~ 6000°K. Therefore, chemical reactions should be considered in the calculational model.
4. The vapor transport analysis shows that, after removing 50% of the vapor, the remaining part is still sufficient to stop the incoming plasma ions.
5. A reduction of 50% in the conversion of ion energy to radiation energy, reduces the total amount of vaporized material by about 98%.

Since the erosion by evaporation and melting during a plasma disruption influences the life time of first wall, the following items are recommended for further research:

- Vapor shield models which include atomic processes.
- Chemical reactions between first wall material and plasma.
- Melt layer stability.

Moreover, tokamak experiments must establish a better data base for deposition energy densities, deposition times, and first wall damage.

Acknowledgements

The authors would like to thank Dr. S. Mori for his kind suggestions of initiating the present collaboration study. They also acknowledge Drs. Y. Iso, K. Tomabechi, M. Yoshikawa, T. Iijima and M. Ohta for their continued encouragement.

References

[1] Proc. IAEA Symp. on Current Disruption in Toroidal Devices (1979), IPP III/51.

[2] R. Behrisch, Nucl. Fusion 12 (1972) 695.

[3] R. Behrisch, J. Nucl. Mater. 85 & 86 (1979) 1047.

[4] L.L. Loebel, W.G. Wolfer, University of Wisconsin Report UWFDM-370 (1980).

[5] A.M. Hassanein, G.L. Kulcinski, and W.G. Wolfer, J. Nucl. Mater. 111 & 112 (1982) 554 and UWFDM-494 (1982).

[6] A.M. Hassanein, Thesis, University of Wisconsin Report UWFDM-465 (1982).

[7] M. Maeno, S. Sengoku, H. Nakamura, S. Yamamoto, M. Seki and H. Kawamura, Japan J. Appl. Phys. 21 (1982) L773.

[8] J.D. Callen, private communication.

[9] INTOR, Phase one, Intern. Atomic Energy Agency, Vienna (1981).

[10] T.S. Taylor, GA-A 16698 (1981) and GA-A16816 (1981).

[11] Ya.B. Zel´dovich, Yu.P. Raizer, Physics of Shock Waves and High Temperature Hydrodynamic Phenomena, Vol.1, Academic Press, New York (1966).

[12] R.W. Schrage, A. theoretical study of interphase mass transfer, Columbia Univ. Press. New York (1953).

[13] S.I. Anisimov, A.Kh. Rakhmatulina, Sov. Phys. JETP 37 (1973) 441.

[14] D.T. Vier, Los Alamos Laboratory report LA-5937-MS (April, 1975).

[15] A.M. Mullendore, private communication.

[16] W.G. Wolfer, A.M. Hassanein, J. Nucl. Mater. 111 & 112 (1982) 560.

[17] S.K. Erents, C.M. Braganza and G.M. McCracken, ibid, 63 (1976).

[18] C.M. Braganza, S.K. Erents and G.M. McCracken, ibid, 75 (1978).

[19] R. Yamada, K. Nakamura, K. Sone and G.M. McCracken, ibid, 95 (1980) 278.

[20] J. Bohdansky, H.L. Bay and W. Ottenberger, ibid, 76 & 77 (1978) 163.

[21] M. Mohri, K. Watanabe, T. Yamashina, H. Doi and K. Hayakawa, ibid, 85 & 86 (1979) 1185.

[22] K. Sone, M. Saidoh, K. Nakamura, R. Yamada, Y. Murakami, T. Shikama, M. Fukutomi, M. Kitajima and M. Okada, ibid, 98 (1981) 270.

[23] R. Yamada, K. Nakamura, K. Sone and M. Saidoh, ibid, 111 & 112 (1982).

[24] J. Roth, J. Bohdansky, K.L. Wilson, ibid, 111 & 112 (1982) 775.

[25] V. Philipps, K. Flaskamp, E. Vietzke, ibid, 111 & 112 (1982) 781.

[26] S. Fukuda, S. Kato, M. Mohri, T. Yamashina, ibid, 111 & 112 (1982) 839.

Appendix A Computer Code to Calculate First Wall Response to a Plasma Disruption "A*DISRUP"

I. Intrduction

The A*DISRP computer code is designed to calculate the response of first wall to a plasma disruption. It is a part of the general code A*THERMAL which designed to calculate the deposition and response of first wall due to any kind of radiation, i.e., light and heavy ions, X-rays, laser, and heat flux. A*THERMAL also calculates the sputtering and the displacement damage of the wall. The A*DISRUP is a finite difference code, whereas A*THERMAL solves the problem in both finite difference and the Green's function methods.

A*DISRUP is written in FORTRAN V for the UNIVAC-1110 at the University of Wisconsin-Madison and converted for FACOM M-200 in JAERI. All routines should be readily adaptable to any computer system with the exception of plotting and file handling, which need some modifications.

II. Preliminary information required for A*DISRUP

The fundamental data required for a calculation with A*DISRUP is listed below.

(1) Material thermal properties as a function of temperature, i.e., density, specific heat and thermal diffusivity as a polonomial function of the temperatures; for example

$$f(T) = a_1 + a_2T + a_3T^2 + a_4T^3$$

where f = density or specific heat or thermal diffusivity, and
T = temperature.

These property variations are required for both solid and liquid state. Other functions for the thermal properties of the material could easily be adopted by the code.

(2) The melting point and the atomic weight of the material and both latent heat fusion and heat of vaporization.

(3) The variation of the vapor pressure of the material with temperature.

Expressions for vapor pressure as a function of temperature were fit with the genral form

$$\log p = d + \frac{f}{T}$$

where p is the saturated vapor pressure in atom at temperature T, and d and f are constants. Up to two separate expressions can be used to obtain sufficient accuracy over the temperature range.

III. Descriptions of calculation procedure

Commands:

Card #1

1.	STARF	One of the subroutines to generate the space mesh array

Followed by:

Card #2

A	NSX	Max # of space point minus two (usually 48)
B	NST	Max # of time points (usually 250)
C	DELTX	First zone increment (usually 1.E-4 cm)

Command:

Card #3

2.	FHTFLX	Calculate the temperature as a function of time and space and calculate the amount of material melted and vaporized for input heat flux

Followed by:

Card #4

A	RANGE	Average range of plasma ions mainly D&T into first wall material (cm)
B	TP	Preheat time (can be set to 0.0)
C	TAU	Collision time (can be set to 0.0) will be calculated automatically
D	ALPHA	Vapor energy conversion coefficient
E	BETA	Vapor transfer coefficient

F	ISPUT	If equal 1 means do chemical sputtering If equal 0 means no chemical sputtering calculation

Card #5

A	IFLUX	If equal 1 → (means heat flux calculation without vapor shield) If equal 2 → (means vapor shielding included)
B	ITYPE	If equal 0 (means square pulse) If equal -1 (means triangular pulse)
C	IVAP	If equal 1 (means evaporation and moving boundary calculated)
D	NPTS	# of time points during the deposition time

Card #6

A	NT	Total # of time points (maximum 250)
B	NE	Equal 2 for heat flux calculations
C	IFIL	Incremental step between each time step, for good accuracy this # equal about 20 or 30 for heat flux as high as 600 J/cm^2 or higher fore higher heat fluxes or very small disruption times

Card #7

A	TAMB	Ambient 1st wall temp. (°K)
B	TMELT	Melting point of 1st wall material (°K)
C	HL	Heat of fusion of 1st wall material
D	AM	Atomic weight of 1st wall material

Card #8

A	STIPR	Sticking probability for atoms leaving 1st wall during evaporation (usually 1.0)
B	PZERO	Coefficient of vapor pressure
C	HSUB	Exponential coefficient of vapor pressure
D	HVAP	Heat of vaporization of 1st wall material

Card #9

A	PZI	Coefficient of vapor pressure at another range of temperature (TCHG)
B	HSI	Exponential coefficient
C	TCHG	Temperature at which there is a new value of vapor pressure fitting with temp.

Card #10

A	IXS	Starting space mesh point to print temperature usually in finite difference equal 2
B	IXF	Final space point to print temperature
C	IXD	Increment of space mesh, to print the result
D	IXC	Increment of time mesh after energy deposition

ex. $\rho = DS1 + DS2 \cdot T + DS3 \cdot T^2 + DS4 \cdot T^3$

Card #11

A	DS1	1st coefficient of the solid density as a function of temperature (gm/cm^2)
B	DS2	2nd coefficient of the solid density as a function of temperature
C	DS3	3rd coefficient of the solid density as a function of temperature
D	DS4	4th coefficient of the solid density as a function of temperature

Card #12

A	DL1	1st coefficient of the liquid density as a function of temperature (gm/cm^2)
B	DL2	2nd coefficient of the liquid density as a function of temperature
C	DL3	3rd coefficient of the liquid density as a function of temperature
D	DL4	4th coefficient of the liquid density as a function of temperature

Card #13, 14, 15, 16

Repeat last two sets for specific heat and also for thermal diffusivity both for solid and liquid states

Card #17

A	T(1)	Starting time of the problem (0.0) for heat flux
B	T(1)	Final time of the pulse (i.e., pulse duration) in sec

Card #18

A	Y(1)	Heat flux, i.e., (J/cm^2)
B	Y(2)	Same as Y(1)